Universitá del Salento

Dipartimento di Matematica e Fisica

UNIVERSITÀ DEL SALENTO

A high resolution tracker for MEG II Experiment

PhD Student:

Aurora Pepino

Tutors:

Dott. F. Grancagnolo
Prof. M. Panareo

Dottorato di ricerca in Fisica XXVIII ciclo

Ottobre 2016

Contents

List of Figures

List of Tables

Introduction

The $\mu \longrightarrow e\gamma$ decay is forbidden in the framework of the Standard Model although flavour mixing has been observed in neutrinos, which are also categorized as leptons. In this perspective, there is a possibility that the decay occurs; however the expected probability in the Standard Model is much smaller than the limit achievable by current available technology. If the super-symmetry exists, on the other hand, the probability can be enhanced.

The MEG experiment at PSI measures the $\mu^+ \longrightarrow e^+\gamma$ decay with a sensitivity on the Branching Ratio of 10^{-13}, taking a probe on the existence of the theories beyond the Standard Model. In the last data analysis (2016) the upper limit on the $\mu^+ \longrightarrow e^+\gamma$ branching ratio of 4.2×10^{-13} at the 90% CL was set, it is the leading upper limit on the branching ratio of this decay.

In 2013 the experiment planned an upgrade with the aim to improve the sensitivity of one order of magnitude. The key features of the MEG upgrade are an increased rate capability of all detectors to enable running at the intensity frontier and an improved energy, angular and timing resolutions, for both the positron and photon arms of the detector.

A new positron tracker consisting in a high transparency, single volume, high granularity multi wire Drift Chamber is actually under construction at the sections of Lecce and Pisa. Thanks to the innovative semi automatic system, able to manage and produce multi wire frame layers, the wiring procedure is faster and better supervised.

This thesis describes the MEG II tracker focusing the attention on the design of the new Front End Board that performs a first acquisition of the signal coming out from the Drift Camber. The main features of the FE and its design in relation to the applicability of Cluster Timing techniques are discussed. Moreover, the main strategies of the Cluster Counting/Timing in order to improve the detector performance are showed. This work is structured in five chapters.

The first chapter illustrates the interest and the physics motivation in the lepton flavour violation and explains the $\mu^+ \longrightarrow e^+\gamma$ decay .

In the second chapter the detector and its upgrade are presented, pointing out the expected performances.

In chapter 3 we describe the MEG II tracker construction, paying attention to the wiring system designed and built at the INFN Lecce and University of Salento laboratories.

The chapter 4 is dedicated to introduce the basic operation of Drift Chamber, discussing the mechanisms of the signal formation. The DC signal characteristics set the specifications for the design of the Front End board that provides a first amplification of the signal. We show the design of the FE board and the measurements on the last prototypes.

In chapter 5 the momentum and spatial resolution are presented with the possibility to improve them applying the Cluster Counting/Timing techniques. Two different algorithms based on different approaches are implemented and tested on Monte Carlo data simulations in order to get a comparison with the traditional method of obtaining the Distance of Closest Approach from the first cluster. The method of waveforms generation based on electric simulation is described in order to apply the techniques on the simulated waveforms processed by the electronics.

1

LEPTON FLAVOUR VIOLATION

This chapter is an introduction to the physic motivation of the MEG experiment. It focuses on Charge Lepton Flavour Violation (CLFV) processes and explains why they are powerful probes of physics beyond the Standard Model. The $\mu \longrightarrow e\gamma$ decay, forbidden in the Standard Model (SM), will be illustrated reporting the kinematic of the decay, the background processes and the MEG I experiment results.

1.1 Lepton Flavour violation and physic motivation

Particle physics phenomena are extremely well described within the SM of elementary particles and their fundamental interactions. The SM provides a very elegant theoretical framework (1), (2), (3), (4) and it has successfully passed very precise experimental tests in the past decades. The SM is a theory based on the gauge symmetry group $SU(3)_C \times SU(2)_L \times U(1)_Y$, where $SU(3)_C$ (colour symmetry) gives as gauge fields the mediators of strong interactions, $SU(2)_L$ (weak isospin symmetry) and $U(1)_Y$ (weak hypercharge symmetry) are related to the electroweak interactions (5), (6). Therefore Standard Model encloses itself two different theories:

- the **Quantum Cromo-Dynamics (QCD)**, describing the strong interactions between quarks and gluons;

- the **Glashow-Salam-Weinberg** theory for the electroweak interactions.

Gravity is not included in this model because it is negligibly small compared to the other forces. The Standard Model counts six flavours of quarks and six flavours of leptons. They are conventionally parametrized with flavour quantum numbers that are assigned to all subatomic particles, including composite ones. For hadrons, these quantum numbers depend on the numbers of constituent quarks of each particular flavour. Although the Standard Model predictions have been widely verified by experimental, there are still many unanswered questions and unnaturalness, such as dark matter and the hierarchy problem. Today the SM is considered to be a low energy approximation of a more complete and general theory. In this situation, new theories which replace the Standard Model at high energy scales have been proposed. Among those, supersymmetric (SUSY) (7) models and Grand Unified Theories (GUT) are the favourite candidates for physics Beyond the Standard Model. In particular:

- **SUSY** postulates that each gauge boson has, as a super symmetric partner, a fermion gaugino (photino, zino...), each fermion has a boson partner (smuon, sneutrino, squark...). It allows lepton-slepton transitions, therefore any mixing among the sleptons can provide CLFV;

- **GUT** provide an elegant unification of the strong and electroweak forces in a larger gauge group at some high energy scale. The novel particles predicted by GUT models are expected to have masses around the GUT scale just a few orders of magnitude below the Plank scale and so will be well beyond the reach of any foreseen particle collider experiments. Therefore, the particles predicted by GUT models will not be observed directly while the effects of grand unification might be detected through indirect observations.

These physics models predict experimentally accessible branching ratios for the $\mu \longrightarrow e\gamma$, the $\mu \longrightarrow eee$ decay, and the $\mu \longrightarrow e$ conversion while these processes are almost forbidden in the Standard Model because of the lepton flavour violation (LFV); thus, CLFV is a good probe to test new physics (8), (7), (9). Experiments looking for these CLFV processes are complementary in testing theories beyond the Standard Model and if these processes, forbidden in the SM, exist, their independent measurements can provide a discrimination among the proposed extensions. Glashow has recently written (10):
"Because their standard model branching ratios are far too tiny for possible detection,

observation of any mode would be certain evidence of new physics. That's what makes such sensitive searches potentially transformative".

1.2 Muon decay

In the SM, muons $\mu^{\pm}$ are particles whose mass and lifetime are extremely well known and measured (11):

$$m_{\mu} = 105.6583715 \pm 0.0000035 MeV$$

$$\tau_{\mu} = (2.1969811 \pm 0.0000022) \times 10^{-6} s$$

They decay in one preferential way:

$$\mu^{-} \longrightarrow e^{-}\bar{\nu_e}\nu_{\mu}$$

$$\mu^{+} \longrightarrow e^{+}\nu_e\bar{\nu_{\mu}}$$

These are typical three-body decays, called Michel decays, whose decay width, neglecting radiative corrections, is:

$$\Gamma_{\mu} = \frac{G_F^2 m_{\mu}^5}{192\pi^3} \simeq (2.2\mu s)^{-1} \quad (1.1)$$

where $G_F = (1.166 \cdot 10^{-5})GeV^{-2}$ is the Fermi coupling constant.

Figures 1.1(a) and 1.1(b) show the Feynman diagram of the SM muons decay at tree level and the resulting electron energy spectrum, without radiative corrections. The discovery of neutrino oscillation added new processes that contribute to muon decays. The Lagrangian of the Standard Model, including neutrino mass term, leads to new Feynman diagrams as shown in figure 1.2, and opens to the possibility for the existence of the $\mu \longrightarrow e\gamma$ decay. Including neutrino oscillations in the Minimal Standard Model Lagrangian density, the $BR_{\mu \to e\gamma}$ can be computed as:

$$BR_{\mu \to e\gamma} = \frac{\Gamma_{\mu \to e\gamma}}{\Gamma_{\mu \to everithing}} = \frac{3\alpha}{32\pi} \left| \sum_{i=2,3} U_{\mu i}^{*} U_{ei} \frac{\Delta m_{i1}^2}{M_W^2} \right|^2 \quad (1.2)$$

where:

- $U_{\alpha i}$ are elements of the neutrino mixing matrix;

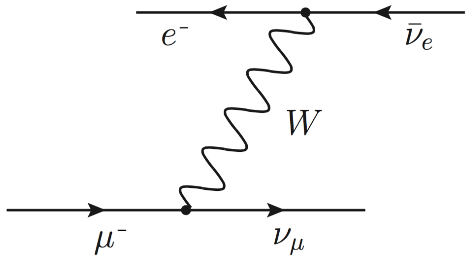

(a)

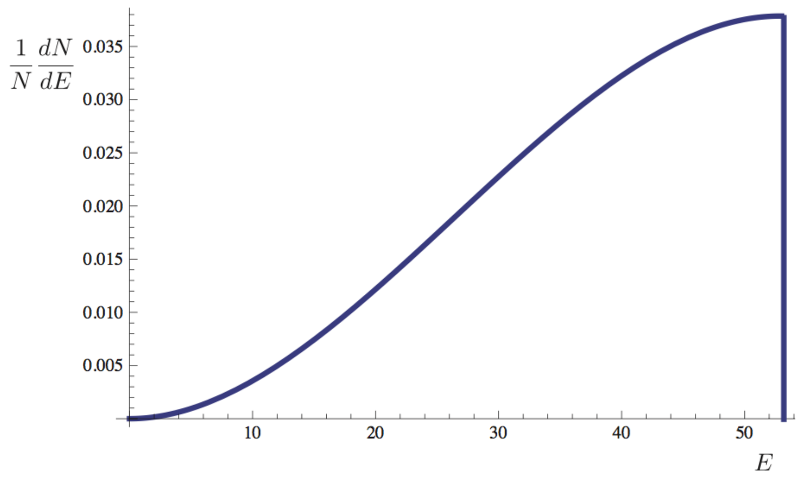

(b)

Figure 1.1: a) $\mu^- \longrightarrow e^-\bar{\nu}_e\nu_\mu$ Feynman diagram in SM; b) energy spectrum of the $e^\pm$ without radiative correction

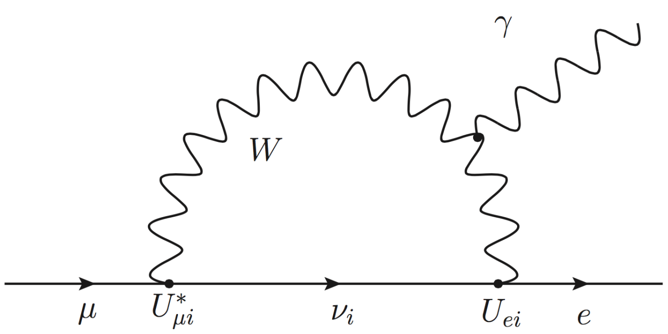

Figure 1.2: $\mu \longrightarrow e\gamma$ diagram induced by neutrino oscillations.

Table 1.1: Muon decays and their Branching Ratios

Mode	Branching Ratio	Confidence Level
$\mu^- \to e^- \bar{\nu}_e \nu_\mu$	$\simeq 100\%$	
$\mu^- \to e^- \bar{\nu}_e \nu_\mu \gamma$	$(1.4 \pm 0.4) \times 10^{-5}$	
$\mu^- \to e^- \bar{\nu}_e \nu_\mu e^+ e^-$	$(3.4 \pm 0.4) \times 10^{-5}$	
$\mu^- \to e^- \nu_e \bar{\nu_\mu}$	$< 1.2\%$	90%
$\mu^- \to e^- \gamma$	$< 4.2 \times 10^{-13}$	90%
$\mu^- \to e^- e^+ e^-$	$< 1.0 \times 10^{-12}$	90%
$\mu^- \to e^- 2\gamma$	$< 7.2 \times 10^{-11}$	90%

- Δm_{ij} are the neutrino mass-squared differences;
- α is the fine-structure constant;
- M_W is the W-boson mass.

The resulting branching ratio is:

$$BR_{\mu \to e\gamma} = O(10^{-54})$$

which is far too small to be detected by any possible experiment. Therefore, any detection of CLFV is a proof of physics beyond the SM.

Table 1.1 summarizes the muon decay modes and their branching ratios with the respective confidence level.

1.3 Experimental searches for CLFV

This section focuses on the history and prospects for Charged Lepton Flavour Violation experiments (12) (13).
The MEG experiment at PSI is leading in this field and it is expected to provide fruitful result soon. Detector upgrade (14) plan is considered to further improve the physics sensitivity of the experiment. The first search for the process $\mu \longrightarrow e\gamma$ was performed by Hincks and Pontecorvo in 1948 at Chalk River (11). The search was motivated by the results from an experiment of Conversi et al. in 1947 (15). The theoretical situation was described by Fermi et al. (16) and the interest was intense.

Table 1.2: History of $\mu \longrightarrow e\gamma$

Year	90% CL on B($\mu \longrightarrow e\gamma$)	Collaboration/Lab	Reference
1947	1.0×10^{-1}	Chalk River	Hincks and Pontecorvo (1948)
1948	.04	Washington University	Sard and Althaus (1948)
1955	2.0×10^{-5}	Nevis	Steinberger and Lokanathan (1955)
1959	7.5×10^{-6}	Liverpool	O'Keefe et al. (1959)
1959	2.0×10^{-6}	Nevis	Berley et al. (1959)
1959	1.0×10^{-5}	Rochester	Devis et al. (1959)
1959	1.2×10^{-6}	CERN	Ashkin et al. (1959)
1960	1.2×10^{-6}	LBL	Frankel et al. (1960)
1961	2.5×10^{-5}	Carnegie	Crittenden et al. (1961)
1962	1.9×10^{-7}	LBL	Frankel et al. (1962)
1962	6.0×10^{-8}	Nevis	Bartlett et al. (1962)
1963	4.3×10^{-8}	LBL	Frankel et al. (1962)
1964	2.2×10^{-8}	Chicago	Parker et al. (1964)
1971	2.9×10^{-8}	Dubna	Korenchenko et al. (1961)
1977	3.6×10^{-9}	TRIUMF	Depommier et al. (1977)
1977	1.1×10^{-9}	SIN	Povel et al. (1977)
1979	1.9×10^{-10}	LAMPF	Bowman et al. (1979)
1982	1.7×10^{-10}	LAMPF	Kinnison et al. (1982)
1986	4.9×10^{-11}	LAMPF/Crystal Box	Bolton et al. (1986, 1988)
1999	1.2×10^{-11}	LAMPF/MEGA	Brooks et al. (1999)
2010	2.8×10^{-11}	PSI/MEG	Adam et al. (2010)
2011	2.4×10^{-12}	PSI/MEG	Adam et al. (2011)
2013	5.7×10^{-13}	PSI/MEG	Adam et al. (2013)
2016	4.2×10^{-13}	PSI/MEG	Baldini et al. (2016)

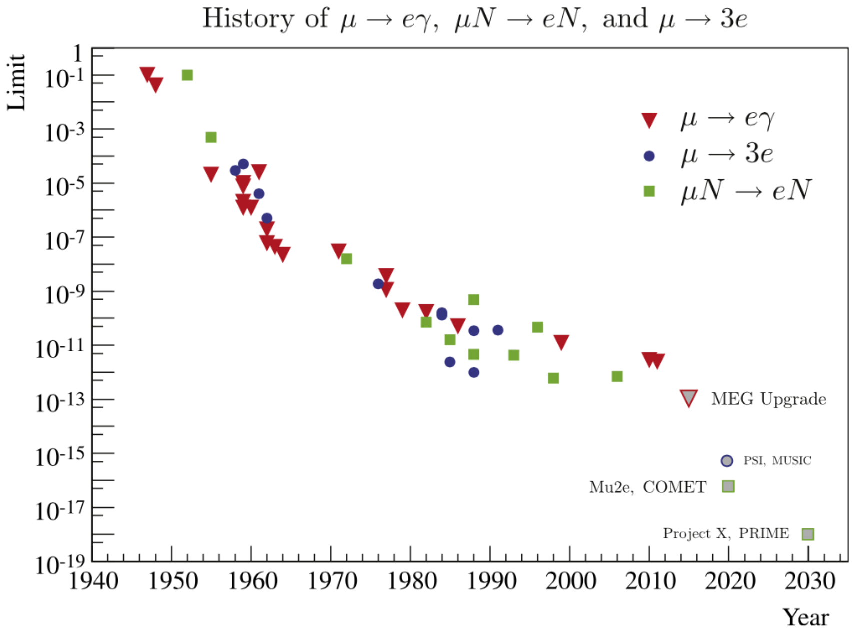

Figure 1.3: The history of CLFV searches in muons

There are a number of activities trying to search for CLFV which are illustrated in the figure 1.3. After pioneering measurements using muons from cosmic rays carried out by Pontecorvo et al. in the late 1940s (11), the experimental sensitivity for CLFV has increased by many orders of magnitude over time as reported in table 1.2 which summarizes the upper limit in lepton flavour violation in the course of time still in improvement.

CLFV channels, complementary to $\mu \longrightarrow e\gamma$ are: $\mu \longrightarrow eee$ and $\mu - e$ conversion. Currently, the most stringent limits come for $\mu \longrightarrow e\gamma$ from the MEG experiment ($BR(\mu \longrightarrow e\gamma) < 4.2 \times 10^{-13}$) (17) and for $\mu \longrightarrow e$ conversions from the SINDRUM II experiment ($R_{\mu e}(\mu N \longrightarrow eN$ on Au$) < 6 \times 10^{-13}$) (18), (19). Confirming the presence of these processes implies the obvious existence of new physics and that is why they are called "*golden channels*".

Two major experiments are in the planning phase to improve the physics sensitivity by more than an order of magnitude compared to the MEG experiment. They use the $\mu - e$ conversion process for this purpose. One is the Mu2e experiment at FNAL in the U.S. and the other is the COMET experiment at J-PARC in Japan. Both experiments set their goal of the branching ratio sensitivity at 10^{-16}, starting physics data acquisition around 2018. Another effort in search of CLFV is being considered at PSI using a different decay mode of muons. The experiment intends to search for the decay $\mu^+ \longrightarrow e^+e^-e^+$ using the surface muon beam provided at PSI and a new detector (20) in order to improve the sensitivity on the branching ratio beyond the current best limit of 1.0×10^{-12} obtained by the SINDRUM experiment (21).

The comparison between $\mu \longrightarrow e\gamma$ versus $\mu \longrightarrow e$ conversion and $\mu \longrightarrow 3e$ is usually done in a model independent way by using the effective Lagrangian (12):

$$L_{CLFV} = \frac{m_\mu}{(k+1)\Lambda^2}\bar{\mu_R}\sigma_{\mu\nu}e_L F^{\mu\nu} + \frac{k}{(k+1)\Lambda^2}\bar{\mu_R}\gamma_\mu e_L \bar{f}\gamma^\mu f \tag{1.3}$$

which contains two possible terms contributing to CLFV. While $\mu \longrightarrow e\gamma$ proceeds only via the first term, corresponding to $k = 0$, the $\mu \longrightarrow e$ conversion process and the $\mu \longrightarrow 3e$ decay may proceed also through the other one (large k values). Figure 1.4 shows the range of parameters in the (k, Λ) plane which can be explored for the sensitivities that can be reached by $\mu \longrightarrow e$ conversion, $\mu \longrightarrow 3e$ or $\mu \longrightarrow e\gamma$ experiments. While the sensitivity for $\mu \longrightarrow e\gamma$ is restricted to small values of k, the $\mu \longrightarrow e$ conversion can probe for new physics effects for a large range of the parameter space of k with best sensitivities for large k. Therefore the $\mu \longrightarrow e\gamma$ and $\mu \longrightarrow e$ processes have complementary sensitivity to new physics effects, and it is important to search for CLFV using both processes. All the relevant SUSY-GUT models privilege the $k = 0$ term for which one can see from the figure 1.4 that MEG is not only competitive with the second phase of the $\mu \longrightarrow 3e$ experiment but also, with a much shorter time-scale and a far lower budget, with the first phase of the Mu2e project. We finally care to note that the upgraded MEG will represent the best effort to address the search of the $\mu \longrightarrow e\gamma$ rare decay with the available detector technology coupled with the most intense continuous muon beam in the world.

1.4 Mu e gamma decay: the kinematics of the event

In this section the relativistic kinematic is described in order to find the value of energy, momentum and time in which the particles are produced by the decay. The $\mu \longrightarrow e\gamma$ decay has a two body final state. Positive muons are stopped in a thin target to observe their decay at rest. The thin target minimizes multiple scattering effects that could spoil the measurements of the daughter positron kinematic variables. The experiment

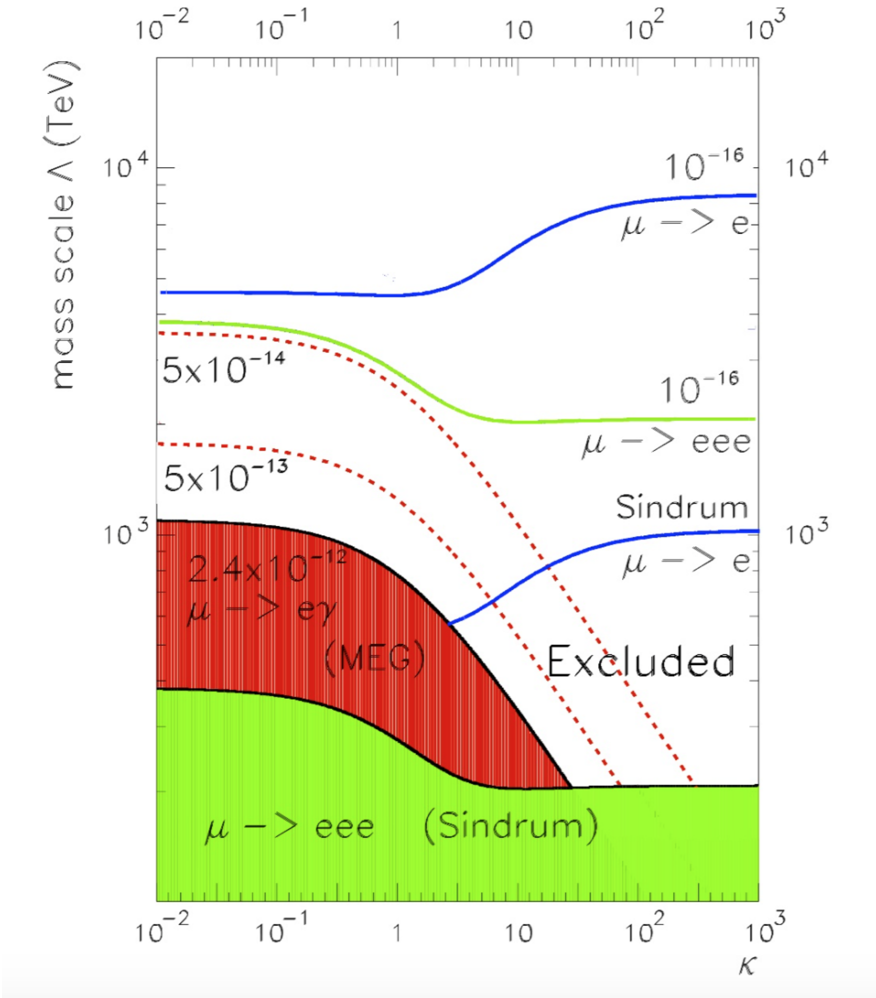

Figure 1.4: the range of parameters in the (Λ, k) plane that are explored by $\mu \longrightarrow e\gamma$, $\mu \longrightarrow 3e$, $\mu \longrightarrow e$ econversion experiments

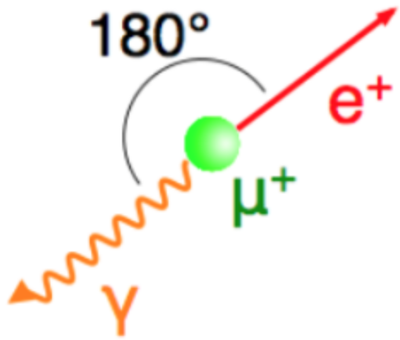

Figure 1.5: $\mu \longrightarrow e\gamma$ event signature

uses stopped μ^+ rather than μ^- and bring the muons to rest in a thin target. The reasons are that one gets more π^+ than π^- from the proton collision and so the final data sample is larger; moreover muons captured on the nucleus typically cause the nucleus to eject protons, neutrons, and photons, which produce accidental rates in the detector. Further, if one uses a surface beam of π^- to make the muons, one has to deal with all the π^- capture products as well.
The energy conservation and the quadri-momentum conservation in the center of mass system are:

$$\left\{ \begin{array}{ccc} E_\mu & = & E_\gamma + E_e \\ 0 & = & \overrightarrow{p_e} + \overrightarrow{p_\gamma} \end{array} \right. \tag{1.4}$$

The relativistic relation between energy mass and momentum in natural units (c=1) for the particles is:

$$E_\mu^2 = m_\mu^2 + |\overrightarrow{p_\mu}|^2$$

$$E_e^2 = m_e^2 + |\overrightarrow{p_e}|^2$$

$$E_\gamma^2 = m_\gamma^2 + |\overrightarrow{p_\gamma}|^2$$

The muon is stopped in the target so its momentum is null and its energy correspond to its mass, while the photon has mass equal to zero. So the positron and the photon have the following energy:

$$E_e = \sqrt{m_e^2 + |\overrightarrow{p_e}|^2}$$

$$E_\gamma = |\overrightarrow{p_\gamma}|$$

Putting these expressions in the system 1.4 and solving it we can find the energy of both particles:

$$E_e = \sqrt{(\frac{m_\mu^2 - m_e^2}{2m_\mu})^2 + m_e^2}$$

$$E_\gamma = \frac{m_\mu - m_e}{2m_\mu}$$

Considering the mass of electron that is negligible with respect to the mass of the muon, finally we obtain the expression of energy and momentum of both the particles:

$$E_e = \sqrt{\frac{m_\mu^2}{4} + m_e^2} \simeq \frac{m_\mu}{2} = 52.8MeV$$

$$E_\gamma = \frac{m_\mu^2 - m_e^2}{2m_\mu} \simeq \frac{m_\mu}{2} = 52.8MeV$$

1.5 Signal and background

As described in the previous section, the $\mu^+ \longrightarrow e^+\gamma$ event signature is given by the simultaneous and collinear back to back emission of photon and positron, with the same energy equal to half the muon mass, so the event signature of the decay must satisfy the following requirements:

- one γ with $E = 52.8\ MeV$ and one e^+ with $E = 52.8\ MeV$;
- direction of the momentum of the e^+ and γ extrapolated to the same point in the target;
- angle between the direction of the momenta at the decay vertex $\theta_{e\gamma} = 180°$
- moving back to back and forming a relative angle $\theta_{e\gamma} = 180°$;
- produced simultaneously and detected in coincidence $\Delta t_{e\gamma} = 0$;

In order to identify the event with high efficiency and to reject the background, high resolution measurements and efficient algorithm for signal/background discrimination are required. There are two important backgrounds:

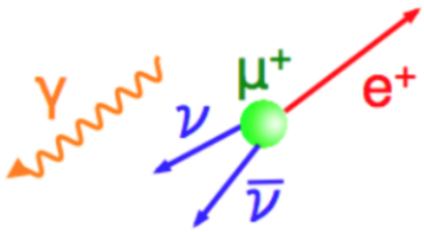

(a)

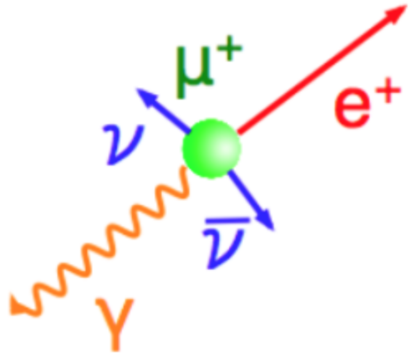

(b)

Figure 1.6: a) $\mu^+ \longrightarrow e^+\gamma$ accidental background; b) $\mu^+ \longrightarrow e^+\gamma$ radiative background

1. **In time physics background** due to the Radiative Muon Decay (RMD) $\mu^+ \longrightarrow e^+\nu_e\bar{\nu_\mu}\gamma$, where the positron and gamma ray are emitted back-to-back and two neutrinos carry off small momentum

2. **Accidental background**, which arises when an energetic positron coming from a normal Michel decay $\mu^+ \longrightarrow e^+\nu_e\bar{\nu_\mu}$ that overlaps, within the timing resolution, with a photon coming from:

   (a) Radiative muon decay $\mu^+ \longrightarrow e^+\nu_e\bar{\nu_\mu}\gamma$ where the neutrino momenta are small

   (b) Annihilation in flight of positrons (for example, from another muon decay): $e^+e^- \longrightarrow \gamma$, with a photon of appropriate momentum and direction to combine with a regular Michel decay

   (c) $e^+N \longrightarrow e^+N\gamma$ from scattering off a nucleus (Bremsstrahlung photons).

The accidental background is dominant and it is determined by the detector resolutions of the MEG experiment. The expected number of accidental background events (N_{acc}) depends on the uncertainty affecting the measurements of the four relevant quantities (E_γ, P_e, $\theta_{e\gamma}$, $t_{e\gamma}$). It can be expressed as:

$$N_{acc} \propto R_\mu^2 \times \Delta E_\gamma^2 \times \Delta P_e \times \Delta\theta_{e\gamma}^2 \times T \times \Delta t_{e\gamma} \tag{1.5}$$

where:

- R_μ is the muon stopping rate

- T is the measurement time

- ΔE, ΔP_e, $\Delta\theta$, $\Delta t_{e\gamma}$ are the experimental resolutions for the photon energy, the muon momentum, the opening angle, and the relative timing.

The number of expected signal events N_{sig} depends on the solid angle Ω subtended by the detectors (the acceptance of the apparatus), on the efficiencies of the detectors (ϵ_γ, ϵ_e) and of the selection criteria (ϵ_s). In a measurement time T, for a given branching ratio BR it yields:

$$N_{sig} = R_\mu \times T \times BR \times \Omega \times \epsilon_\gamma \times \epsilon_e \times \epsilon_s \tag{1.6}$$

In those experiments in which the expected decay is not observed it is possible to define the Single Event Sensitivity (SES) and set an upper limit on BR with a certain confidence level (usually 90%). The SES is defined as the BR which corresponds the record of one event in the experiment (in absence of background):

$$SES = BR(\mu \longrightarrow e\gamma) = \frac{1}{R_\mu T \frac{\Omega}{4\pi}} \frac{1}{\varepsilon_e \varepsilon_\gamma \varepsilon_s} \tag{1.7}$$

Assuming a muon stopping rate of 3×10^7 μ/s, a running time of 4×10^7 s, an acceptance of 9%, $\varepsilon_s = 0.7$, $\varepsilon_\gamma = 0.4$, $\varepsilon_e = 0.65$ the correspondent SES is 5×10^{-14}.

A high SES implies acceptance and efficiencies should be maximized. In addition background rejection (see equation 1.5) requires good resolutions on the kinematic parameters are required, with special attention on photon energy and emission angle, whose contribution is squared.

Therefore if high rates are needed from a statistical point of view, on the other hand with too high rates the background becomes intolerable, for fixed experimental resolutions, so the muon stop rate cannot be increased too much but it must be accurately chosen in order to keep a reasonable signal over background ratio. In summary, we need:

- a high intensity continuous muon beam

- a positron spectrometer which can measure high-rate positrons precisely

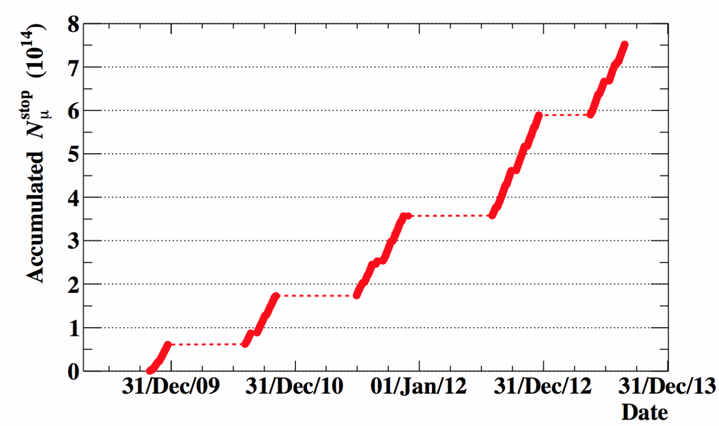

Figure 1.7: Accumulated stopped muon in the course of the years

- a gamma-ray detector which has a high energy resolution
- a timing counter with a good time resolution

Based on this concept, the MEG experiment has planned an upgrade that involve all the detectors.

1.6 MEG I last physics results

The MEG experiment sets the most stringent constrain on CLFV, establishing the upper limit on the $\mu^+ \longrightarrow e^+\gamma$ branching ratio: $BR = 4.2 \times 10^{-13}$ at the 90% CL confidence level (17).

Data were accumulated intermittently in the years 2008-2013 (see figure 1.7). The data accumulated in 2008 were presented in (22), but the quality of those data was degraded and therefore they are not considered in the last full dataset analysis (17). In total, 7.5×10^{14} muons were stopped on target in 2009-2013. The analysis based on the 3.6×10^{14} muons stopped on target in 2009-2011 has published in (23). The data from the remaining 2.3×10^{14} muons stopped on target in 2012, and from 1.6×10^{14} muons stopped on target in 2013 are included in last analysis (17) completing the full dataset. The upper limits of the BR measurement on the decay, over the last six years are reported in (22), (24), (23), (17).

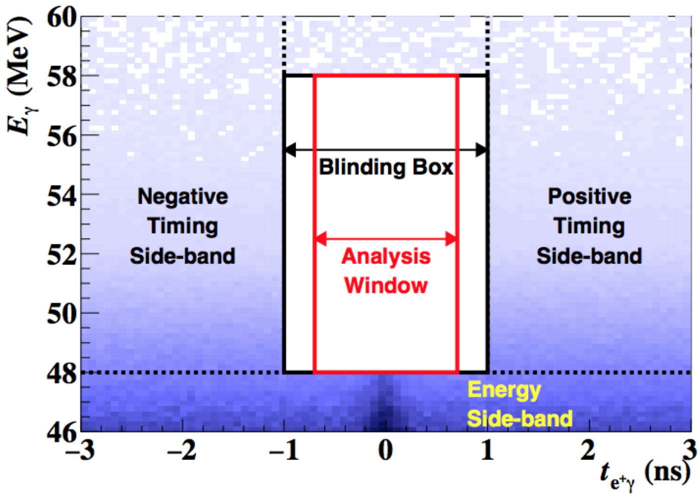

Figure 1.8: The MEG blinding box that defines the events to be processed

Positron and photon energies E_{e^+} and E_γ, e^+ γ relative time $t_{e^+\gamma}$ and relative azimuthal and polar angles ($\theta_{e^+\gamma}$ and $\phi_{e^+\gamma}$) are the observables available to distinguish possible $\mu^+ \longrightarrow e^+\gamma$ candidates from background.

The MEG analysis strategy is a combination of blind and maximum likelihood analysis. The blind analysis is chosen to prevent any bias in the evaluation of the expected background in the analysis region and the maximum likelihood analysis is preferred to the simpler box analysis in order to avoid boundary effects at the borders of the analysis region and to improve the sensitivity by correctly taking into account the probabilities of events being due to signal, RMD or accidental background.

In the first stage of the MEG analysis, events are preselected depending on the presence of, at least, one positron track candidate and a time match given by $-6.9 < t_{LXe-TC} < 4.4\ ns$, where t_{LXe-TC} is the relative difference between the LXe time and the TC time associated with the positron candidate. The pre-selected events, that are those events falling in the window of the plane defined by $\mid t_{e^+\gamma} \mid < 1\ ns$ and $48.0 < E_\gamma < 58.0\ MeV$ called "Blinding Box" and represented in figure 1.8, are hidden and written in a separate data stream. Events with $\mid t_{e^+\gamma} \mid < 1\ ns$ fall in the "timing side bands", while events with a relative timing and with $E_\gamma < 48.0\ MeV$ fall into the "energy side-band". Events falling in the side-bands, that are very likely to be accidental events, are used for optimizing the analysis parameters and for studying the background.

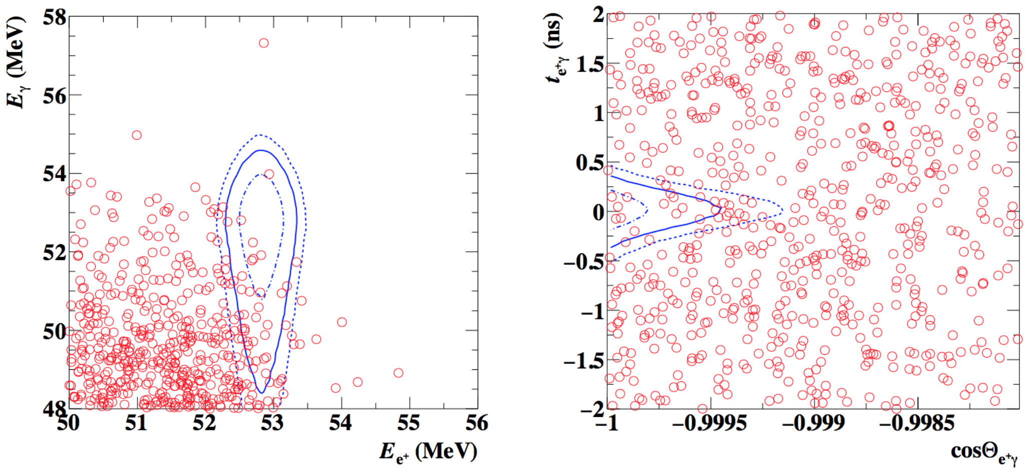

(a) (b)

Figure 1.9: a) Event distribution in the kinematic variables planes: E_e vs E_γ; b) Event distribution in the kinematic variables planes: $t_{e\gamma}$ vs $\cos\theta_{e\gamma}$

At the end of the optimisation procedure, the events in the blinding box are analysed and a maximum likelihood fit is performed to extract the number of signal (N_{sig}), RMD (N_{RMD}) and accidental background (N_{ACC}) events. The likelihood fit is performed on events falling in the "Analysis Window" defined by $48.0 < E_\gamma < 58.0\ MeV$, $50.0 < E_{e^+} < 56.0\ MeV$, $\mid t_{e^+\gamma} \mid < 0.7\ ns$, $\mid \theta_{e^+\gamma} \mid < 50\ mrad$ and $\mid \phi_{e^+\gamma} \mid < 75\ mrad$. The size of the analysis window is chosen to be between five and twenty times the experimental resolutions of all observables in order to prevent any risk of losing good events and to restrict the number of events to be fitted at a reasonable level.

Figures 1.9(a) and 1.9(b) shows the event distributions for the 2009-2013 full dataset on the (E_{e^+}, E_γ) and ($cos\vartheta_{e^+\gamma}$, $t_{e^+\gamma}$) planes with the signal PDF contours (1σ, 1.64σ, 2σ). No significant correlated excess is observed within the signal contours, thus no signal event is observed.

An effort to upgrade the existing MEG detector is currently underway with the goal of achieving an additional improvement in the sensitivity of close to an order of magnitude (14). The modifications are designed to increase acceptance, enable a higher muon stopping rate, and improve limiting detector resolutions. Tracking and timing detectors for measuring the positrons have been completely re-designed and other parts of the detector have been refurbished. The problems with the tracker system degraded significantly the data taken (22) contributing to have a worse estimate of the BR upper limit and in general in the event detection. For this purpose a new low mass and high transparent tracker (25), in order to detect positron trajectory is currently under development and construction at INFN of Lecce (26) and Pisa. The efficiency of the positron reconstruction will be highly improved with respect to the current one, thanks to the high efficiency tracking system combined to the optimized relative position of the tracker and the timing counter. The tracker, that will be described in details in the next chapters, is expected to have a single hit resolution in the transverse plane of 110 μm that could be further improved implementing alternative track reconstruction based on Cluster Timing techniques (27), (28), (29), (30). The improved detector is expected to improve the branching ratio sensitivity to 5×10^{-14} with three years of data taking planned for the coming years.

2

THE MEG EXPERIMENT UPGRADE

This chapter is an overview of the MEG experiment detector, it intends to illustrate the main parts of the detector, their upgrade and the resolution which are planned to reach. The status of the MEG upgrade is described with a particular focus on the Lecce group activities.

2.1 MEG and the upgrade to MEG II

The MEG collaboration consists of about sixty physicists from Japan, Switzerland, Italy, Russia and the USA. A proposal (14) was submitted to the PSI committee and was approved in 2013, which aims at a sensitivity enhancement of one order of magnitude compared with the current MEG experiment.

As explained in previous chapter, equation 1.6 implies that, in ideal conditions, the best single event sensitivity and the largest intensity muon beam is recommended in order to increase statistics and achieve the lowest possible BR. At the same time, the experimental resolutions must be good enough to suppress the accidental background rate that increases as R_μ^2 (see equation 1.5). In order to balance those conflicting requirements, the experiment should satisfy the following requisites:

- a **high intensity muon beam** of $10^7 \div 10^8 \mu/s$, that is currently only available at the Paul Scherrer Institut (PSI) in Villigen (CH);

- a **photon detector with high energy resolution** to reject background positrons from RMD and annihilation of photons in material;

- a **precision spectrometer** that can manage high positron rates and that should provide high position resolution;

- **good position and timing resolutions** are also required to minimize accidental background events.

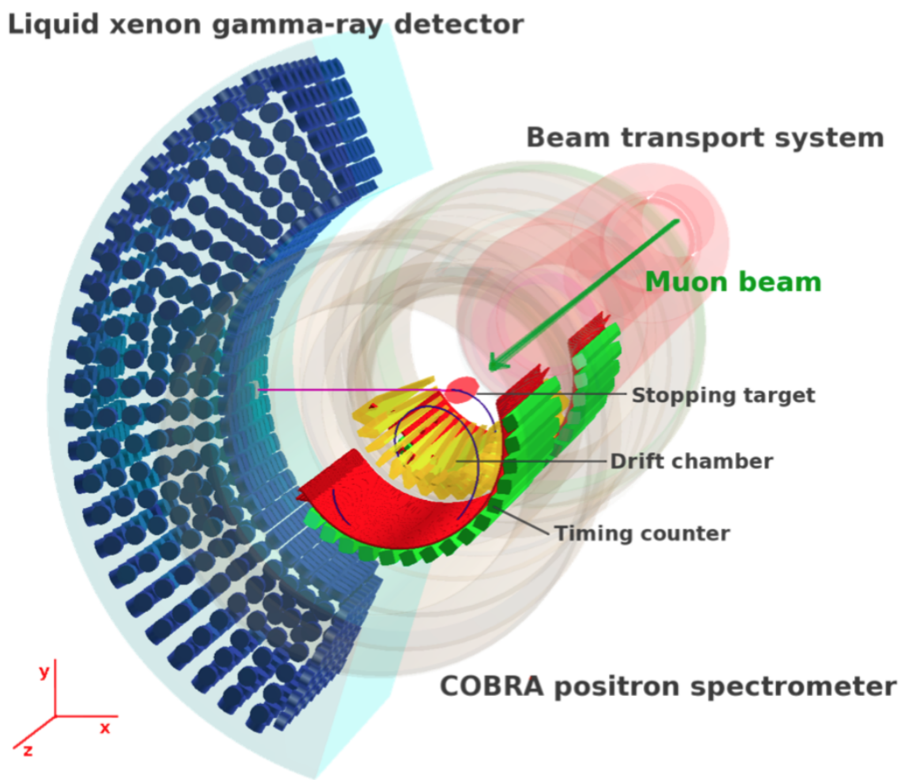

Figure 2.1: MEG I detector overview

The MEG experiment at PSI satisfies most of these requirements. Figure 2.1 shows a sketch of the MEG I experiment: a monochromatic muon beam is stopped in a thin target, μ^+ decay at rest and the expected positrons and γ rays characteristics are measured by a drift chamber coupled to a timing counter and a liquid xenon calorimeter respectively. The coordinate system (x, y, z) is defined as follows: the origin is the center of the spectrometer magnet where the stopping target is located. The z-axis is the direction along the μ^+ beam axis and the y-axis points vertically upward. The region with $z > 0$ is referred to as upstream, while with $z < 0$ as downstream. The experiment improvements have been proposed (14) and approved for the MEG II experiment to achieve the highest possible sensitivity and fully exploit the muon beam intensity. The main features of the MEG experiment upgrade are following reported:

1. increasing the muon beam rate from 3×10^7 to 7×10^7 μ/s which is the current maximum rate available at PSI;
2. a thinner stopping target ($140\mu m$ at $15°$ to the beam);
3. a new lower mass drift chamber with a reduced radiation length, improved granularity and resolution
4. a better coupling between positron tracker and timing counter;
5. a new pixelated timing counter system with a better timing resolution for positrons;
6. extended calorimeter detector acceptance to achieve a better photon resolution: better energy, position and timing resolutions;
7. enhancement in photon efficiency with less material at the photon entrance face of the calorimeter and a new layout of the PMTs at the lateral faces of the calorimeter.

Figure 2.2 schematically shows the main improvements in the MEG II experiment with respect to the MEG experiment, while figure 2.3 shows the design of the MEG II detector apparatus. Since all the detectors are planned to improve their performances, also an improved trigger and DAQ are required, while maintaining a high bandwidth (further details will be given in the next chapters). Measured and expected resolutions (14) and detection efficiencies for MEG I and MEG II detector are shown in table 2.1

2.2 PSI Facility

In the PSI User Laboratory, the world's most intense DC muon beam is available, thus it runs several particle accelerators offering access to its facilities: the Swiss Light Source, SLS, the Swiss spallation neutron source, SINQ, and the Swiss Muon Source, SμS, cyclotron.

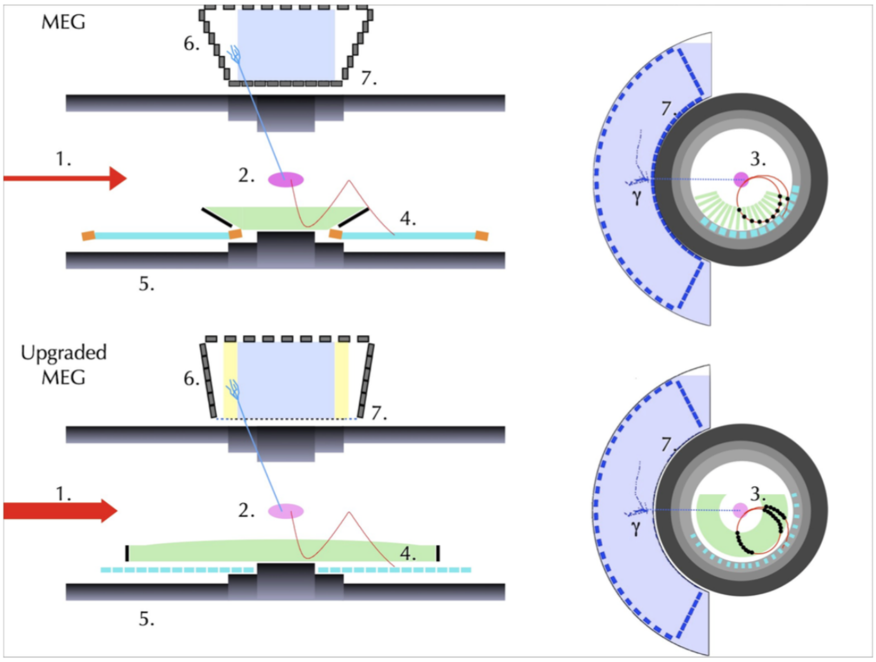

Figure 2.2: MEG detector upgrade

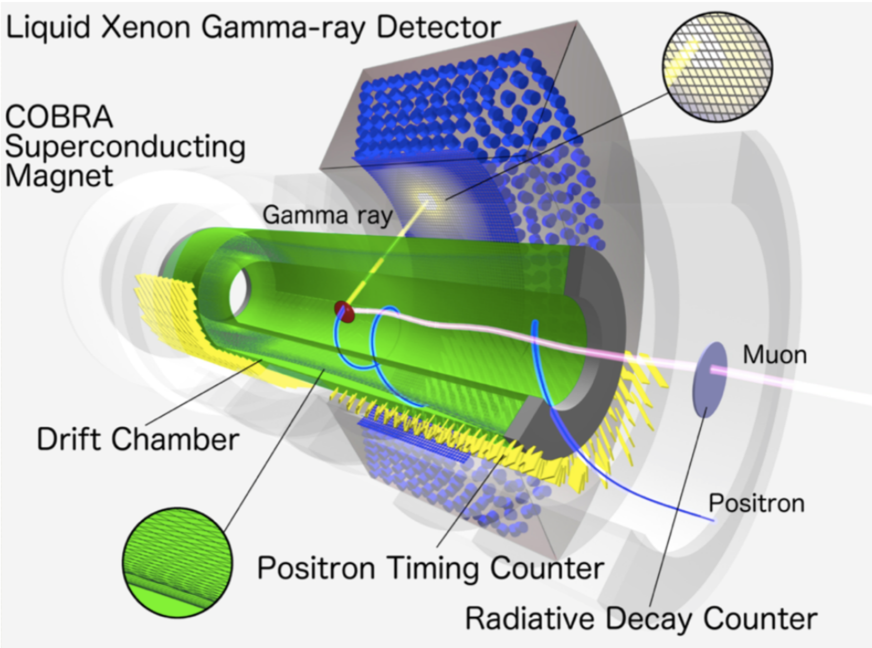

Figure 2.3: MEG II experimental apparatus

Table 2.1: MEG I vs MEG II expected resolutions (Gaussian σ) and detector efficiencies

PDF Parameters	Present MEG	Upgrade Scenario
$\sigma_{E_{e^+}}$ (keV)	306 (core)	130
$e^+\sigma_\vartheta$ (mrad)	9.4	5.3
$e^+\sigma_\phi$ (mrad)	8.7	3.7
$e^+\sigma_Z/\sigma_Y$ (core) (mm)	2.4 / 1.2	1.6 / 0.7
γ energy (%) $(w < 2cm)/(w > 2cm)$	2.4/1.7	1.1/1.0
γ position in (mm) $u/v/w$	5/5/6	2.6/2.2/5
$\gamma - e^+$ timing (ps)	122	84
Efficiency (%)		
trigger	$\simeq 99$	$\simeq 99$
γ	63	69
e^+ reconstruction	40	88

2.2.1 The Beam

The MEG experiment uses a secondary beam produced by the cyclotron depicted in figure 2.4. The cyclotron contains a cascade of three accelerators that delivers a proton beam of 590 MeV energy at a current up to 2.3 mA (1.36 MW). The proton beam is pre-accelerated in a Cockcroft-Walton electrostatic column to an energy of 870 keV and this is increased to 72 MeV in the 4-sector injector cyclotron. Final acceleration of the main beam to 590 MeV occurs in the large 8-sector Ring Cyclotron, from which the beam is transported to the experimental hall. The layout of cyclotron facility is reported in the figure 2.5, while the main characteristics of cyclotron accelerator are summarized in table 2.2. Secondary beams of pions are generated at 2 different target stations, that are distinguished by their respective thicknesses: 7 mm for the M target and 40 $\div$ 60 mm for the E target. The two targets feed seven different pion and muon beam lines.

The channel used by the MEG experiment, namely the $\pi E5$ channel, selects low energy muons product in the E target, with an angle of about 175° respect to the primary beam direction. The main characteristics of the $\pi E5$ channel are summarized in tab 2.3.

Pions decay at rest in the target, the resulting surface muons (those muons which

Figure 2.4: Paul Scherrer Institute 590 MeV proton cyclotron

Table 2.2: Main characteristics of PSI cyclotron proton beam

Injection energy	72 MeV
Extraction energy	590 MeV
Extraction momentum	1.3 GeV/c
Relative energy spread (FWHM)	1.2%
Beam emittance	$2mm \times \pi mrad$
Beam current	$> 1.8mA$DC
Accelerator frequency	50.63 MHz
Time between pulses	19.75 ns
Bunch width	0.3 ns

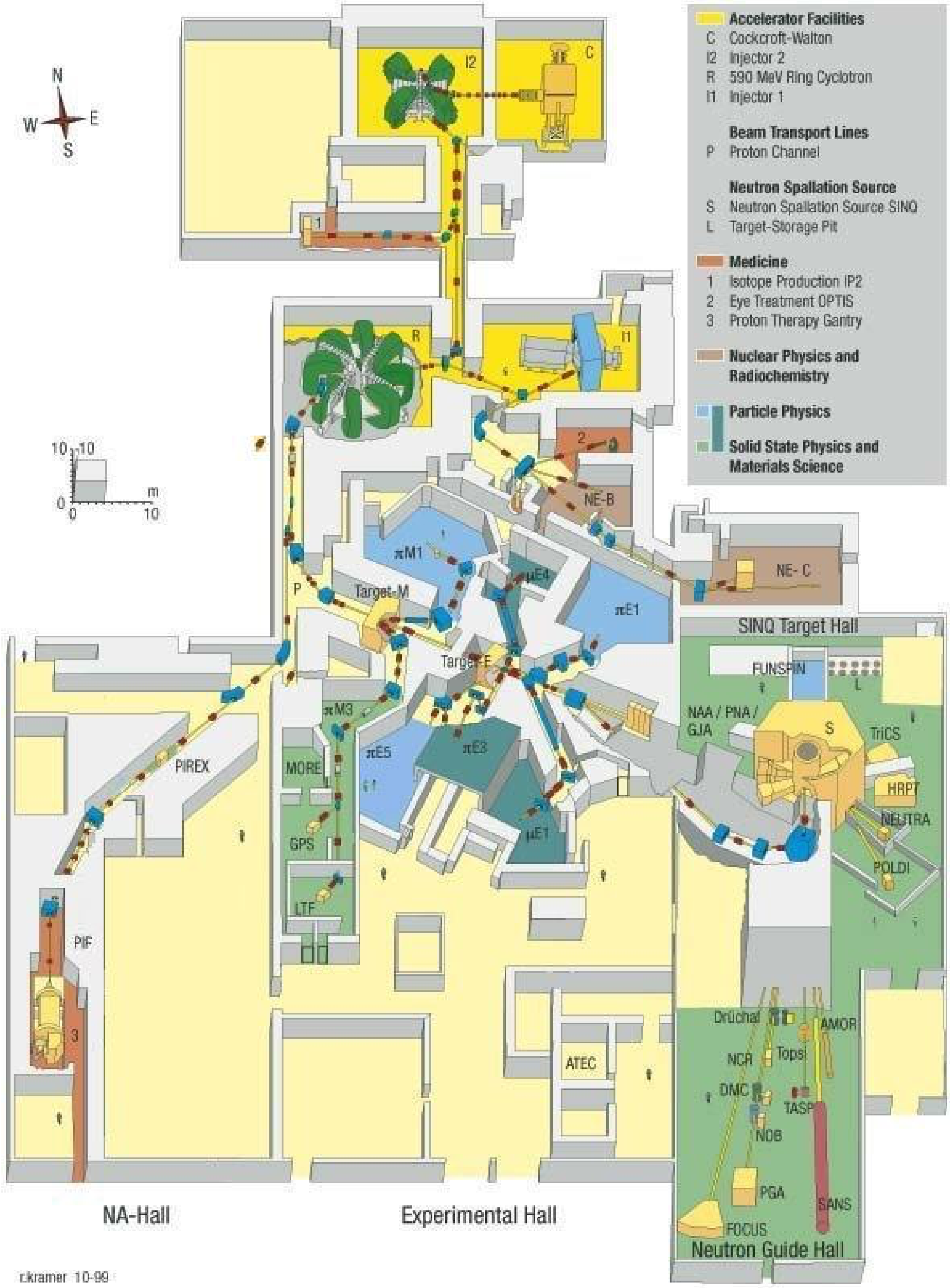

Figure 2.5: The cyclotron facility and the beam lines at the PSI. The MEG experiment is carried out in $\pi E5$ which is located at the center.

Table 2.3: Main characteristics of $\pi E5$ beam line

Solid angle acceptance	150 msr
Momentum range	$20 \div 120$ MeV/c
Length	10.4 m
Relative momentum band (FWHM)	10%
Relative momentum resolution (FWHM)	2%
Horizontal emittance	$> 15.3 cm \cdot rad$
Vertical emittance	$3.6 cm \cdot rad$

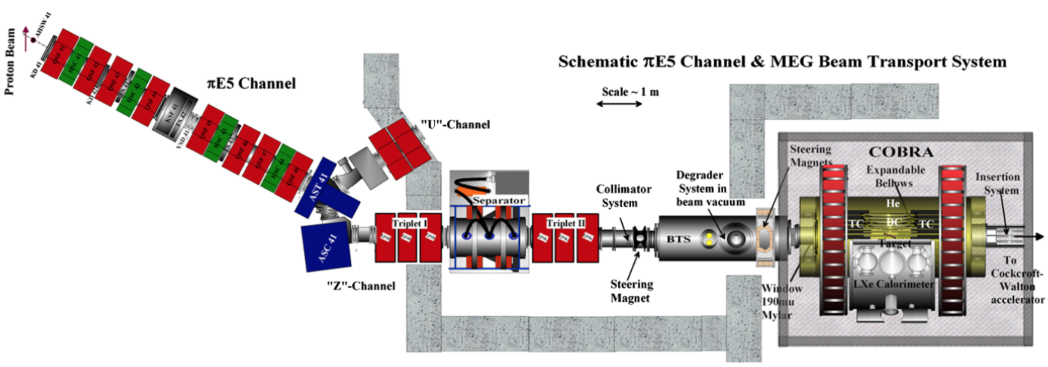

Figure 2.6: Schematic view of the MEG beam line configuration

are produced close to the target surface), have 28 MeV/c momentum and can be easily stopped in a thin target (like the MEG one), in such a way to reduce the multiple scattering phenomena that could affect particles coming from thick target. The final configuration, according to the figure 2.6, is mainly made by the following elements

1. a quadrupoles triplet, that preliminary focuses the beam coming from the primary beam line;

2. an electrostatic separator (Wien filter), that cuts down the positron content of the muon beam. After passing through the separator, the positron contamination in the beam is less than 1%;

3. a second quadrupoles triplet that re-focuses the beam after the separator stage;

4. a beam transport solenoid (BTS) that carries the μ beam in the COBRA volume.

Inside the transport solenoid a μ momentum degrader (Mylar sheet of 300 μm thickness) is placed. The degrader further reduces the muon momentum, thus optimizing the fraction of muons stopped in the thin target.

2.2.2 The target

Positive muons are stopped in a thin target at the centre of the spectrometer, where they decay at rest. The target requirement is to have a stopping efficiency higher than 80%, while multiple scattering, bremsstrahlung and annihilation in flight of positrons from muon decays inside the target should be minimised. These opposing requirements are satisfied by using a 205 μm thick layer of polyethylene and polyester (density 0.895 g/cm^3) with an elliptical shape with semi-major and semi-minor axes of 10 cm and 4 cm, respectively. The target foil is equipped with seven cross marks and eight holes of radius 0.5 cm to allow for both optical survey and software alignment purposes. The foil is mounted in a Rohacell frame, which is attached to the tracking system support frame and placed at an angle of 20.5° to the beam axis. A picture of the target before installation in the detector is shown in Fig 2.7.

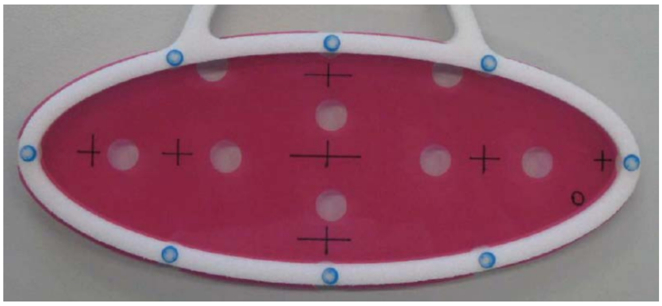

Figure 2.7: The muon stopping target

2.3 MEG and MEG II Apparatus overview

In this section a brief MEG apparatus overview and its upgrade will be presented in order to focalize the main aspects of the detector.

There are three important components for the MEG experiment: the world most intense DC muon beam produced by the 1.3 MW high intensity proton accelerator in the Paul Scherrer Institute, a positron spectrometer (a superconducting magnet, a drift chamber and a timing counter), and a liquid Xenon calorimeter for γ mesurements (31).

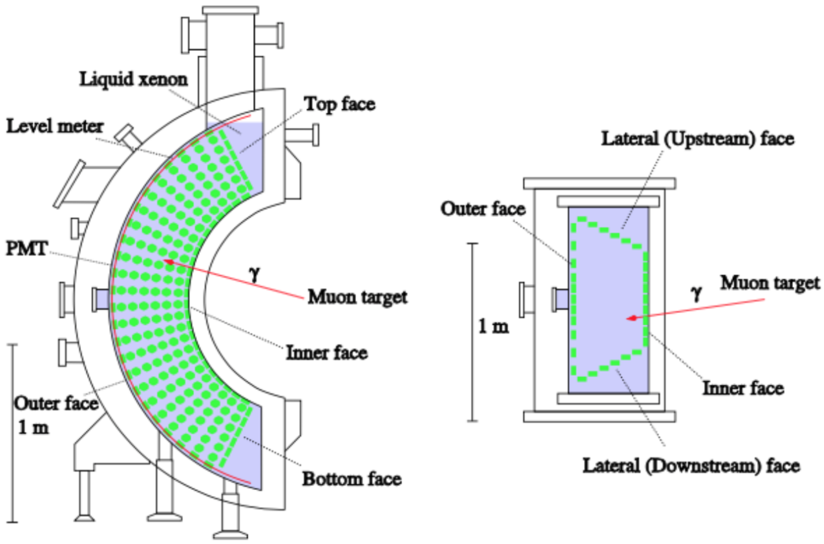

Figure 2.8: Schematic view of the liquid xenon detector: from the side (left) and from the top (right)

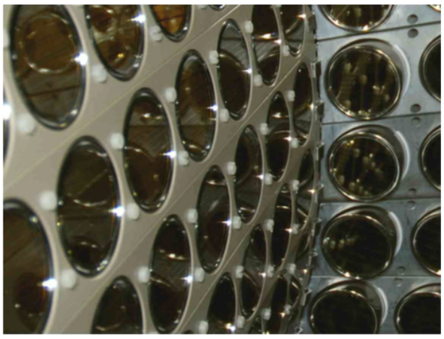

(a)

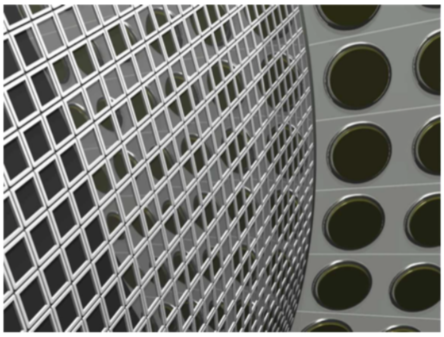

(b)

Figure 2.9: a) MEG LXe detector; b)upgraded LXe detector

2.3.1 Gamma Ray Detector

A γ-ray detector (32), (33) plays an important role for $\mu^+ \longrightarrow e^+\gamma$ detection. It requires excellent position, time and energy resolutions to minimise the number of accidental coincidences between background γ rays and positrons, which are the dominant background process. It is a homogeneous calorimeter able to contain fully the shower induced by a 52.83 MeV photon and measure the photon interaction vertex, interaction time and energy with high efficiency. The photon direction is not directly measured in the LXe detector, rather it is inferred by the direction of a line between the photon interaction vertex in the LXe detector and the intercept of the positron trajectory at the stopping target. A schematic view of the LXe detector, with its C-shape structure fitting the outer radius of COBRA, is shown in figure 2.8. The current gamma ray detector is the world's largest Liquid Xenon (LXe) detector with a 900 l volume surrounded by 846 PhotoMultiplier Tubes (PMT) submerged in the liquid to detect scintillation light in the UV range ($\lambda = 175 \pm 5nm$). Liquid Xenon, with its high density and short radiation length, is an efficient detection medium for photon detection thanks to the fast time constant response to incident radiation. The performance of the detector are 3.3%-2.1% in energy resolution, $\sim 5\ mm$ in position resolution and 67 ps in timing resolution for a 55 MeV gamma-ray.

The current limitation of the LXe detector is mainly related to non uniform light collection in the MEG calorimeter due to non-uniform PMT coverage. The non uniform response is partly corrected in the offline analysis, but it still deteriorates the energy

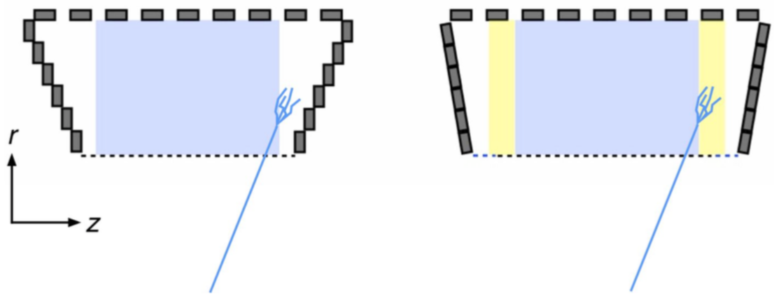

Figure 2.10: MEG (left) and MEG II (right) overview of the PMTs on a given r-z plane

and position resolutions especially for the shallow events. The main concept of the upgrade (14) (34) is to replace the 216 PMTs with about 4000 smaller photo sensors called Multi-Pixel Photon Counter (MPPCs) $12 \times 12\ mm^2$ on the γ-ray incident face (figure 2.9(a) 2.9(b)) together with the reconfiguration of the PMTs at the lateral faces in order to achieve a larger acceptance region (see figures 2.10). The expected energy resolution values for a 52.8 MeV gamma-ray are 1.1% for shallow events and 1.0% for deeper events, while timing resolution is expected to be $\sim 50\ ps$. An improved resulting imaging power is expected in order to have a more efficient rejection of background photons and a reduced photon pile-up.

2.3.2 Positron Spectrometer

Event signature imposes to measure a positron momentum of $\sim 52MeV$; in order to suppress multiple Coulomb scattering of positron, which is relevant for low momentum measurement, we require a **low mass tracker**. In particular, to fulfil the requirement of the MEG experiment, the positron spectrometer must satisfy these conditions:

- stable operation under high positron hit rate

- good resolution of positron momentum, direction and timing

The spectrometer consists of three parts:

1. a superconducting solenoidal magnet,

2. drift chamber

3. timing counter

2.3.2.1 COnstant Bending RAdius (COBRA) magnet

The magnet consists of five coils with different radii to realize gradient magnetic field. Two compensation coils suppress the residual field around the liquid xenon calorimeter, a picture of the magnet is shown in figure 2.11.

Figure 2.11: The COBRA magnet

COBRA is specifically designed to provide a gradient field stronger at the center (z=0) ~ 1.27 T, slowly decreasing as $\mid z \mid$ increases to get a ~ 0.49 T field at both ends as depicted in figure 2.12 where the magnetic field profile along z axis is shown.

Magnetic solenoidal spectrometer of this kind have the advantage of radial energy selection, therefore it is possible to set a detection energy threshold for the tracking detector (Drift Chambers) simply placing them at opportunely chosen radii: this lets to cut out the low energy part of the positron from Michel decay mode $\mu^+ \longrightarrow e^+ \nu_e \bar{\nu_\mu}$.

Pure solenoidal field doesn't match the MEG requirements in terms of tracking efficiency and momentum reconstruction, because:

- positrons emitted with an angle of about 90° respect to beam axis presents a very small pitch of the helical trajectory; jamming the detector with multiple turns with a consequent loss of efficiency (figure 2.13(a));

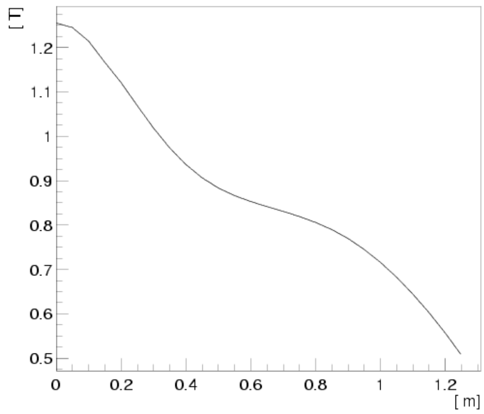

Figure 2.12: Magnetcic field profile along the magnet axis

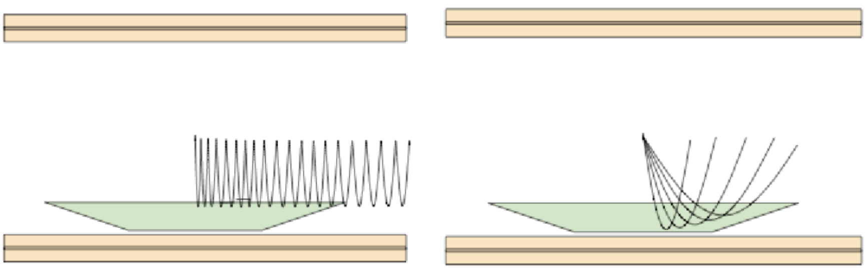

(a) (b)

Figure 2.13: Behavior of particle in an uniform solenoidal magnetic field: a) trajectory made by a positron emitted at 88° respect to the beam axis; b) trajectories of monochromatic positrons emitted at different angles.

- for a fixed value of out coming momentum, the bending radius of the curved trajectory depends on the emission angle, resulting in a complication in track selection and momentum measurement (figure 2.13(b)).

Such complications can be avoided using a quasi-solenoidal field, with a proper gradient; in the case of the COBRA magnet, the gradient is in the direction of the beam axis and also in the radial direction. This particular field map allows positrons emitted with angle near to 90° to make only 1-2 turns inside the chambers, in this way the positrons can be swept out more quickly from the sensitive detector volume,

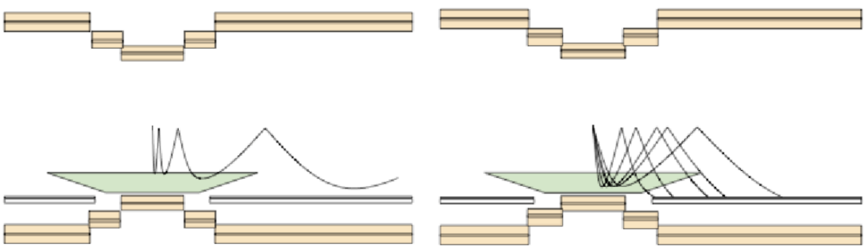

(a) (b)

Figure 2.14: a) Advantages for a quasi-solenoidal magnetic field with gradient along beam axis direction: trajectory made by a positron emitted at 88° with respect to the beam axis, the positron is faster extracted from the DC region; b) trajectories of monochromatic positrons emitted at different angles. The bending radius results to be independent from emission angles

as can be seen in fig 2.14(a), in addition the gradient field make the bending radius independent from emission angles for a given value of the $\vec{p}$ (see fig 2.14(b)).

2.3.2.2 Timing Counters

The Timing Counter of the MEG experiment (35) is designed to deliver trigger information and to accurately measure the timing of the e^+. The main requirements of the TC are:

- fast response used in the on line trigger algorithms and to avoid rate effects;
- fast and approximate ($\sim 5\ cm$) positron impact point;
- excellent ($\sim 50\ ps$) positron impact point time resolution;
- good ($\sim 1\ cm$) positron impact point position resolution in the off line event analysis;
- reliable operation in a harsh environment: high and non uniform magnetic field, possibility of ageing effects, high rate;
- cover the full acceptance region for signal events while matching the tight mechanical constraints dictated by the Drift CHamber (DCH) system and COBRA.

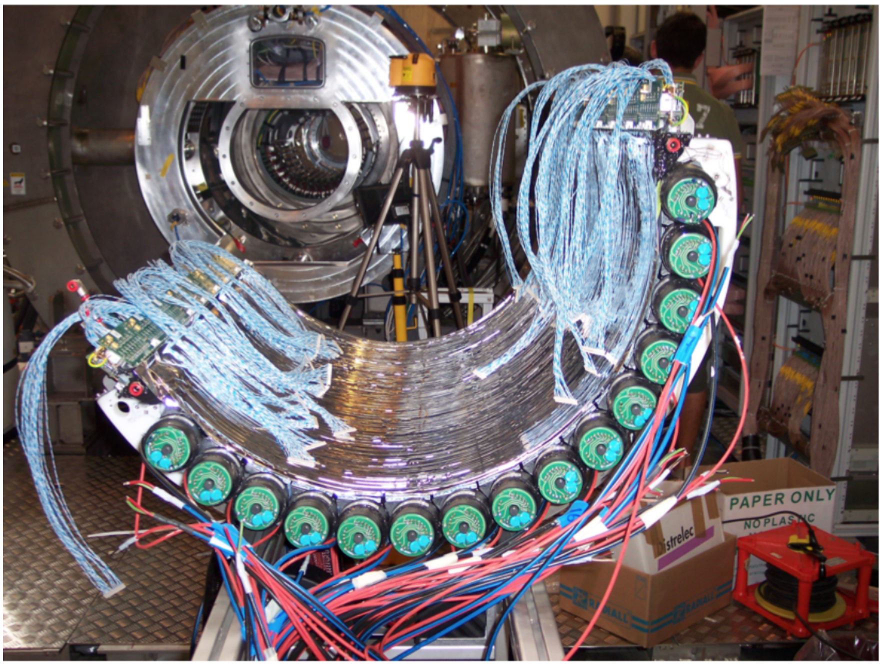

Figure 2.15: A picture of timing counter in front of the COBRA magnet

The MEG I timing counter consisted of 15 plastic scintillation bars (40 $\times$ 40 $\times$ 800 mm^3) and 128 $\times$ 2 plastic scintillation fibres as shown in figure 2.15. The scintillating bars, at the outer radius are read out at each end by PMTs; they are dedicated mainly to the precise time measurements ($\sim$ 50 psec) and, thanks to the segmentation along ϕ, also provides a measurement of the positron impact ϕ coordinate. They also provides a measurement of the positron impact z coordinate by exploiting the separate time measurements of both PMTs. At the inner radius, the transverse detector, consisting of scintillating fibres, is devoted to determining with high precision the impact z coordinate to improve the matching between the DCH track and TC point.

In the MEG II, the new pixelated timing counter is composed of two sets of semi-cylindrical scintillation detectors similarly to the MEG I timing counter, but each detector is segmented as shown in figure 2.16. The higher granularity is obtained by 300 small ultra-fast scintillator plates (90 $\times$ 40 $\times$ 4 mm^3) with silicon photomultiplier (SiPM) readout (34) (14). The advantages in this detector concept over the current timing counter are:

- The single plate can easily have a good timing resolution since ambiguity in the positron path length inside the plate and also in the scintillation light propagation time to the photo-sensor is small.

- Most of the signal positrons passes through more than one pixel. Proper averaging of the times measured at the hit pixels gives more precise information of the positron impact time.

- The hit rate at each segment pixel is lower than 1 kHz even at a high beam rate of 10^8 μ/s. The pileup probability is quite low.

- The multiple pixel hits can provide additional track information.

- For the MEG I timing counter, a positron sometimes leaves double hits in a single timing counter bar which produces a tail component in the timing response function. This problem will not happen in the pixelated timing counter.

- The proposed photo-sensor (SiPM) is insensitive to magnetic field. Note that the detector is placed in the bore of the spectrometer magnet COBRA.

- The detector is operational in the COBRA bore filled with helium gas in contrast to the MEG I detector with PMTs which was housed in a helium-tight plastic bag constantly flushed with nitrogen.

- Flexible detector layout is possible since the position and angle of each pixel module can be individually adjusted.

The timing precision can be improved up to ~ 30 ps with an appropriate counter arrangement where a positron hits several scintillator plates, enabling several timing measurements. SiPMs do not degrade in the helium environment and should not suffer for radiation damage.

2.3.2.3 Drift Chambers

The Drift Chamber (36) of the MEG experiment measures the trajectory and momentum of positrons from $\mu^+ \longrightarrow e^+\gamma$ decays. It is designed to satisfy several requirements:

- operate at high rates, primarily from positrons from μ^+ decays in the target;

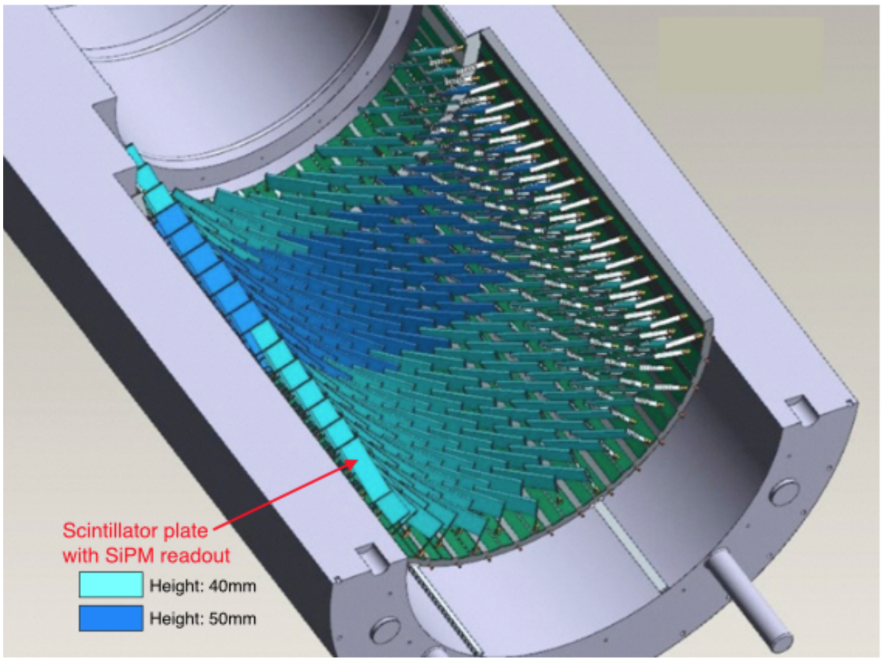

Figure 2.16: Schematic of pixelated timing counter

- have low mass to improve kinematic resolution (dominated by Multiple Scattering) and to minimise production of photons by positron annihilation in flight;
- provide excellent resolution in the measurement of the radial and longitudinal coordinates.

In order to meet these requirements the gas inside the chambers is a light gas mixture of helium and ethane (1:1) and the amount of material in the drift chamber corresponds to an average number of radiation lengths of $2 \times 10^{-3} X_0$ along the 52.83 MeV/c positron track. The MEG I detector apparatus consisted of 16 trapezoidal modules (see figure 2.17) aligned radially at 10.5° intervals in azimuthal angle made of two layers of cells.

The drift cell of each layer consists of a central anode wire and two potential wires on either side, enclosed by two cathode foils spaced 7 mm. The layers of anode planes contains nine drift cells, with a gap of 3 mm between the consecutive planes of the module. Each DC layer is staggered by a half cell (4.5 mm) in order to solve the left-right ambiguity. A schematic cross-sectional view of a part of single chamber module is shown in 2.18. In order to measure the hit position along the wire, namely the z-axis, two kind of informations are exploited:

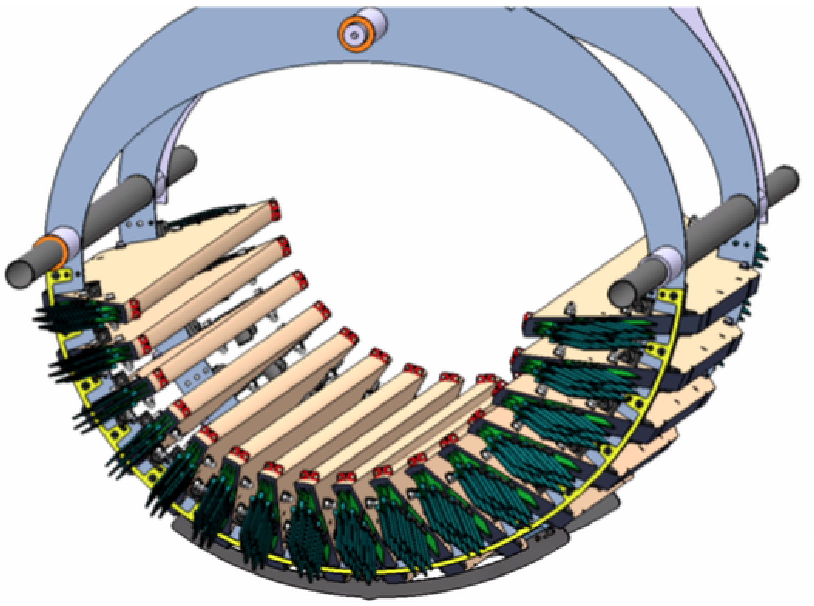

Figure 2.17: Schematic view of MEG I Drift Chamber

1. charge collected on both ends of the wire: since anodes consisted of resistive wires, the resistance seen by the signal is directly proportional to the distance covered on the wire;

2. the avalanche generated by the ionizing particle produces induction on the Vernier Pad cathodes (see figure 2.19)

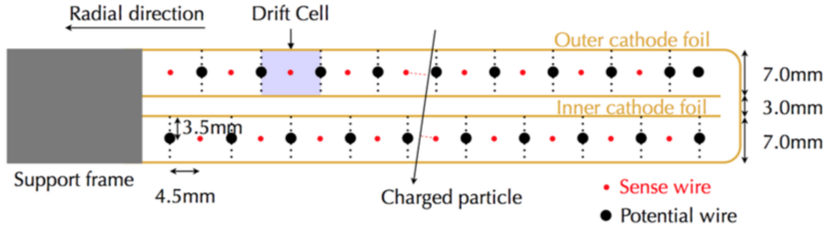

Figure 2.18: MEG I Crift Chamber cell configuration

The MEG I Drift chamber reaches a resolution of $\sigma_z = 550\ \mu m$ on data. The accuracy in the determination of the impact parameter on a wire, defined as single-hit resolution, is $\sigma_r = 210\ \mu m$ in the core and $\sigma_r = 780\ \mu m$ in the tail. The resolutions on

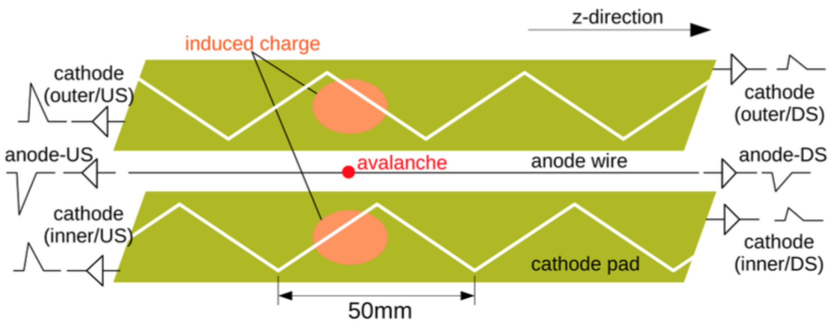

Figure 2.19: Concept of positron z-reconstruction

the positron angle are: $\sigma_{\theta_e} \sim 9.4\ mrad$ and $\sigma_{\varphi_e} \sim 8.7\ mrad$. The resolution obtained on data are worse than the design values ($\sigma_r \sim 200\ \mu m$, $\sigma_z \sim 300\ \mu m$, $\sigma_{\varphi_e,\vartheta_e} \sim 5$ $mrad$), because of the increased noise level in the signals and an unexpected chamber instability, owning to a reduced number of chamber for most of the run period, loosing hits and worsening the spectrometer performance. For this reason a new drift chamber is currently under construction and it will be one of the major improvements of the MEG apparatus for the second phase of the experiment. Specifically, the performance of the tracking system will contribute to improve MEG results by one order of magnitude of the sensitivity on the current branching ratio. The MEG Lecce group is involved both in the new drift chamber construction (37) (38) (39) and for the relative front-end electronics development (40) (41) (42) (43).

MEG upgrade Drift Chamber (see figure 2.20) (38) (37), consists of a unique volume, cylindrical multi-wire drift chamber, with the axis parallel to the muon beam, inspired to the one used in the KLOE experiment (44). The external radius of the chamber is constrained by the available room inside the magnet of the MEG experiment while the length is dictated by the necessity of:

- avoiding any material along the positrons path to the timing counter in order to increase the positron efficiency;
- tracking positron trajectories until they hit the timing counter to minimize the contribution of the track length measurement to the positron timing resolution.

The Cylindrical Drift CHamber (CDCH) is composed of 10 layers of drift cells at alternating stereo angles θ_s ranging from 6° (in the innermost layer) to 8° (in the

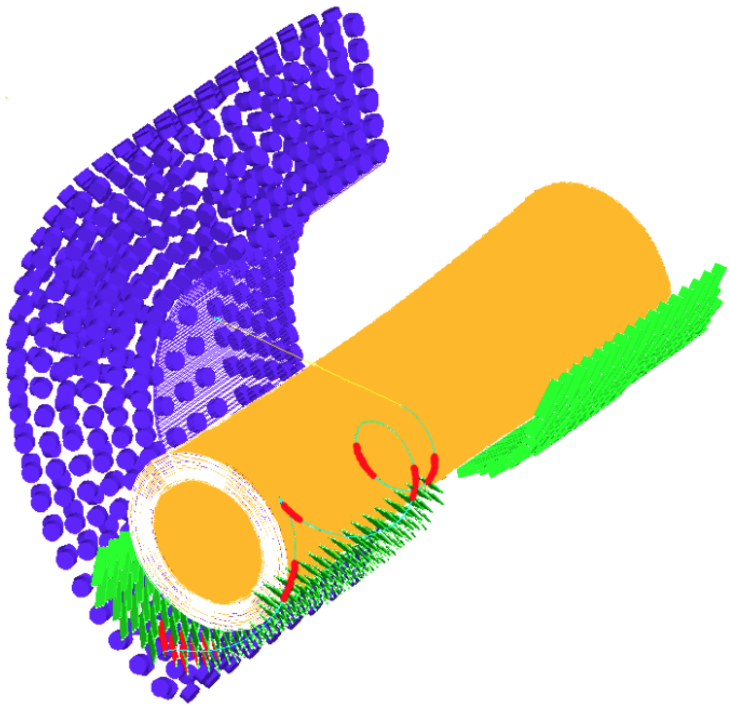

Figure 2.20: New Cylindrical MEG II Drift Chamber

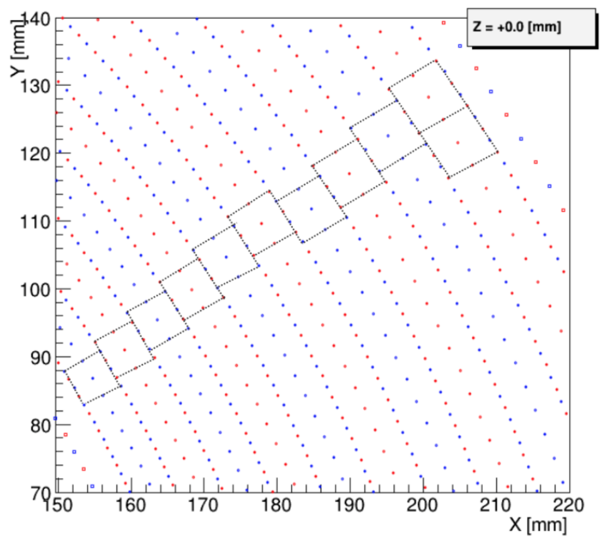

Figure 2.21: Drift cell layout in the middle of the chamber (z=0)

outermost one). The stereo angle will allow to determine the longitudinal coordinate of hits. Drift cells have an almost square shape (see figure 2.21): eight field wires surrounding the central anodic wire with 7 mm of side, in order to guarantee a tolerable occupancy of the innermost wires, which are placed at roughly 18 cm from the beam axis where the rate is $\sim$ 1 MHz for a stopping rate of $7 \times 10^7 \mu/s$. The number of anodic wires is 1920, while the cathode wires are $\sim$ 6400. Gold plated tungsten wires with 20 μm diameter are used as anodes, cathodes and guards are $40 - 50$ μm diameter respectively silver plated aluminium wires. The resulting radiation length per track turn is about $1.6 \times 10^3 X_0$. The most probable number of wires hits is $\sim$ 60, a factor of 3 larger than the present MEG DC system. Due to the large number of hits, a rough determination of the longitudinal coordinate of hits is a precious information for pattern recognition strategies. For this sake, the double readout of wires will permit to exploit charge division and time propagation difference. For an optimal matching to the timing counters, the length of the chamber is set to 193 cm. Despite the fact that in MEG II the acceptance of the apparatus, dictated by the C-shaped xenon detector, is azimuthally limited, the drift chamber has full coverage, to avoid non homogeneous and asymmetric electric fields.

The low momentum of positrons from muon decays and the need for keeping the Coulomb multiple scattering to a minimum requires high transparency: this is achieved using an ultra-low mass gas mixture (Helium and Isobutane 90:10). The usage of the this gas mixture, used also for KLOE experiment, produces a maximum drift time in a cell of $\sim$ 150 ns and an average number of ionization clusters, by the passage of a minimum ionizing particle, quite low (about 12.5 per cm of track), which in turn introduces a bias in the measurement the distance of closest approach (impact parameter) of a particle from the anode wire. Aiming to eliminate this bias has been proposed an alternative track reconstruction strategy: the Cluster Timing/Counting technique (29) (28) (45), coupled to fast front end electronics for signal acquisition (40) (42) (41) , which will be the aim of the studies presented in this thesis. A higher bandwidth (above 1 GHz) of the electronics Front End is needed to recognize individual clusters, originating from the primary ionization in the chamber and apply Cluster Timing algorithms. This will be an important upgraded element of the new trigger and DAQ system. In the next chapters foreseen improvements in spatial resolution and track reconstruction will be presented using Cluster Timing techniques.

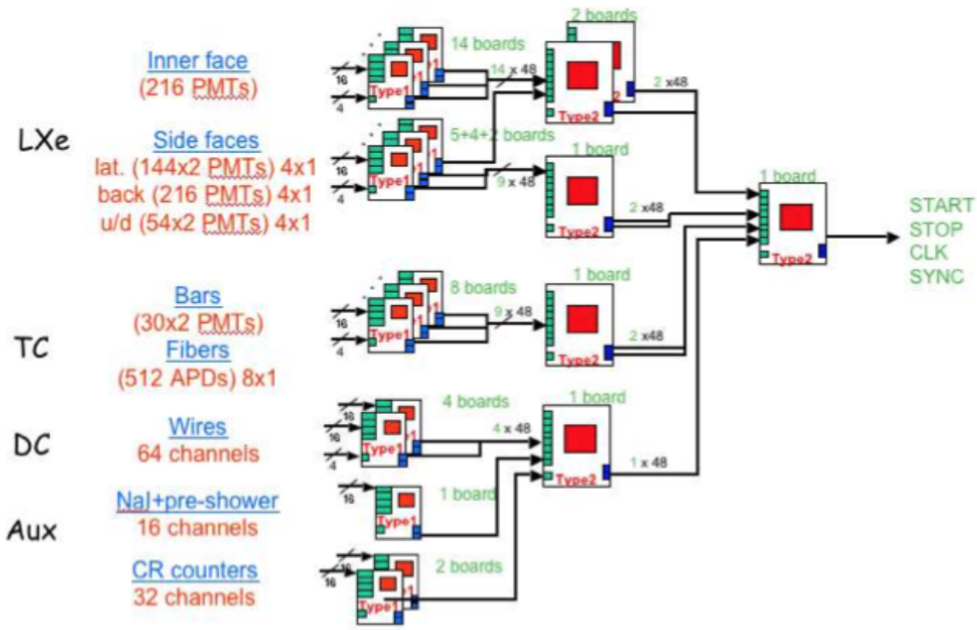

Figure 2.22: The structure of the trigger system; the boards are arranged in a tree-like structure

Definitively the drift chamber final goals are:

- a single hit resolution equal to $\sigma_r \sim 120\mu m$;
- a momentum resolution of $\sigma_p \sim 150\ keV$;
- an angular resolution of $\sigma_{\varphi_e,\theta_e} \sim 5\ mrad$;
- a drift chamber timing counter matching efficiency $\sim 90\%$, within the detector acceptance.

2.3.3 Trigger and DAQ System

The trigger system processes the signals coming from the fast detectors, to select $\mu^+ \longrightarrow e^+\gamma$ like events and reject the background, keeping an acceptable acquisition rate. The main informations used at trigger level are:

- the γ energy and time, reconstructed by the Xenon calorimeter;
- the positron time, given by Timing Counter;

- the direction match between the reconstructed directions of the two particles.

The information on the positron momentum by the drift chambers is not used, being too slow because of the delay of the electrons drift time in the gas. The γ energy is reconstructed by summing all PMTs charges, each one weighted by its gain and quantum efficiency. The selected energy threshold for the MEG trigger is $E_\gamma > 45MeV$. The γ timing is extracted from the rise time of the waveform associated with the PMT which shows the maximum signal, while the positron timing is evaluated using the mean of the times measured by the two PMTs of each bar. The γ-positron coincidence time window is set to 10 ns. The combined informations about γ positron direction is used to reject non collinear events.

The actual trigger hardware is mainly based on two types of boards: a first level trigger board, that receives the analog signals and performs a digitization at 100 MHz by means of Flash Analog-to-Digital Converter (FADC), and the second level trigger boards, based on Fast Programmable Gate Array (FPGA), which operates on the digitized signal applying different algorithms depending of the kind of implemented trigger. A third board (ancillary board) is added to the trigger system to provided the clock and the synchronization signals to all other boards. A schematic view of the trigger system is shown in figure 2.22. The experiment recorded the waveforms from all the detectors to obtain the precise information such as the charge, the time, the baseline, and the pileup with a fast digitizer called Domino Ring Sampler (DRS) (46). When an external trigger signal came, the domino wave stopped and the waveform stored was read out with a shift resister at lower frequency and digitized by an external 12 bit FADC . The data was acquired with a sampling speed of 1.6 GHz for the liquid xenon detector and timing counter and 0.8 GHz for the drift chambers.

The proposed upgrade of the MEG detector requires two main improvements of the existing DAQ system:

- more channels are needed both for the DAQ and the trigger systems,
- a higher bandwidth of the waveform digitizing system is required in order to use the algorithms based on cluster timing.

While the increase of DAQ channels is moderate and could be fulfilled with the existing system just by using a few more crates, the bandwidth of the old system is

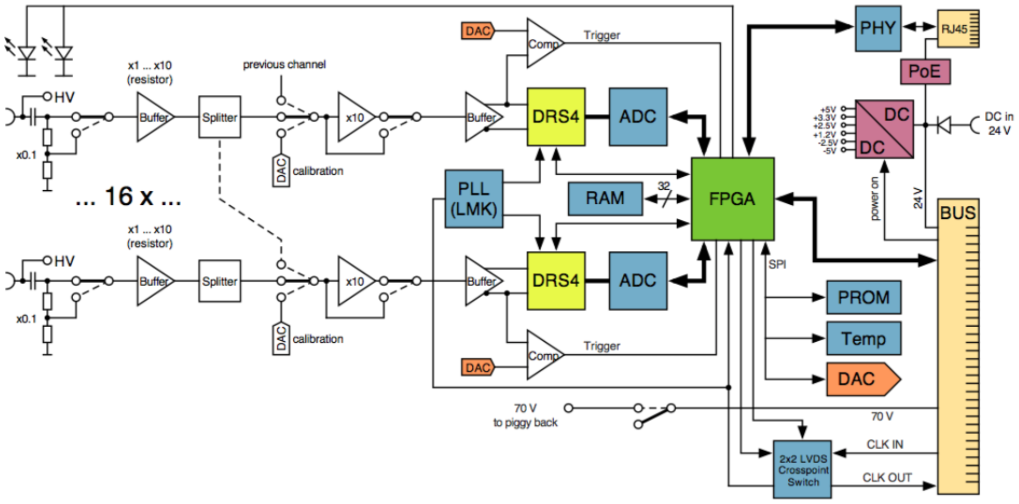

Figure 2.23: A simplified scheme of the new DAQ board

limited by the analog front-end of the DRS4 waveform digitizing boards. A cheap and simple scheme has originally been chosen, which uses only a passive transformer to convert the single-ended signal from the drift chambers into the required differential signal needed by the DRS4 chip. This scheme however limits the bandwidth to about 200 MHz. For this reason a DAQ board, which combines both the waveform digitizing technology using the DRS4 chip as well as the trigger and splitter functionality of our current system are under development. To overcome the DRS bandwidth limitation, a new active analog front-end has already been designed and tested. This front-end has two switchable gain stages, which can be combined to obtain a post-amplification by a factor one to about 70. The post-amplification can be used to increase the signal amplitude coming from the drift chamber pre-amplifiers which are typical in the order of a few ten millivolts. By increasing the amplitude to a few hundred millivolts, the signal-to-noise ratio inside the DRS4 chip is improved, which allows more accurate charge measurements. Figure 2.23 shows the simplified schematic of the new DAQ board (47). The proposed drift chamber requires the recognition of individual cluster originating from the primary ionization in the chamber gas. In a first phase, this cluster recognition will be done off-line on a PC, with a easy development and optimization of wavefrom analysis. In the second phase could be proposed to implement the algorithm directly inside FPGA and DAQ board (27).

3

The MEG II Drift Chamber

The design of the MEG II DC is optimised for meeting the fundamental requirements of high transparency for low multiple scattering contribution (50 MeV positrons), sustainable occupancy ($\sim 7 \times 10^7 \mu^+/s$ stopped on target) and fast electronics for cluster timing capabilities. This chapter focuses on the MEG II DC description and its innovative construction procedure performed by the INFN Lecce-Pisa groups.

3.1 Drift Chamber Overview

The MEG II Drift Chamber is a single volume cylindrical drift chamber with 2π coverage. Despite the fact that in MEG II the acceptance of the apparatus, dictated by the C shaped xenon detector, is azimuthally limited, the new drift chamber has full coverage, to avoid non homogeneous and asymmetric electric fields. The mechanical structure, shown in picture 3.1 is made by a 1.93 meter long cylinder divided in twelve sectors, in each sector there are ten multi-wire layers. The single multi-wire layer is realized with a custom wiring robot (26) by INFN Lecce group and finally it is mounted on the mechanical structure at INFN of Pisa (25). Gold-plated tungsten wires with 20 μm diameter are used as anodes, while cathode and guard wires are 40-50 μm silver plated aluminium wires.

The drift cells have an approximately squared shape 7×7 mm^2 and placed with different stereo angles θ_s ranging from 6° (in the innermost layer) to 8° (in the outermost one) in order to reconstruct the coordinate along the axis of the chamber by combining the information of adjacent layers. The entire detector has 1920 drift cells in total.

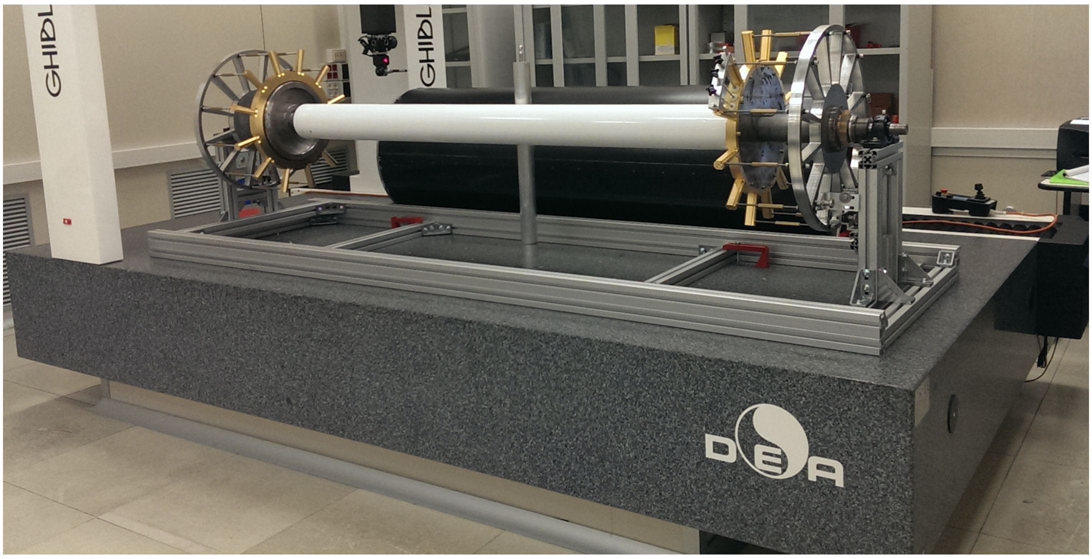

Figure 3.1: Cylindrical Drift Chamber structure

The anode wires are read out at both ends by a 1 GHz bandwidth DAQ chain. Due to the large number of hits, a rough determination of the longitudinal coordinate of hits is a useful information for pattern recognition strategies. For this sake, the double readout of wires will permit to exploit charge division and time propagation difference. Simulation studies (48) (49) show that, at a given single hit resolution of 110 μm, the momentum resolution is expected to be 110 keV and the angular resolution (in ϕ and θ) of 5 $mrad$ (14).

3.1.1 Mechanics

The detector geometry is realised by stacking FR4 printed circuit boards (figure 3.2) with PEEK spacers (figure 3.3) in each of the twelve sectors of the helm-shaped end-plate. A cylindrical carbon fibre frame guarantees the proper wire tension. At the inner radius an aluminated mylar foil encloses the gas volume and provides the proper boundary conditions for guard wires.

For stringing more than 10000 wires, a new construction tool was developed at INFN section of Lecce and it will be described in the next section with more details. The tension of the drift chamber wires is measured with two different methods: an acoustic method, in which mechanical oscillations are induced by acoustic bursts on wires at high voltage, and an electrical method, with oscillations induced by an applied

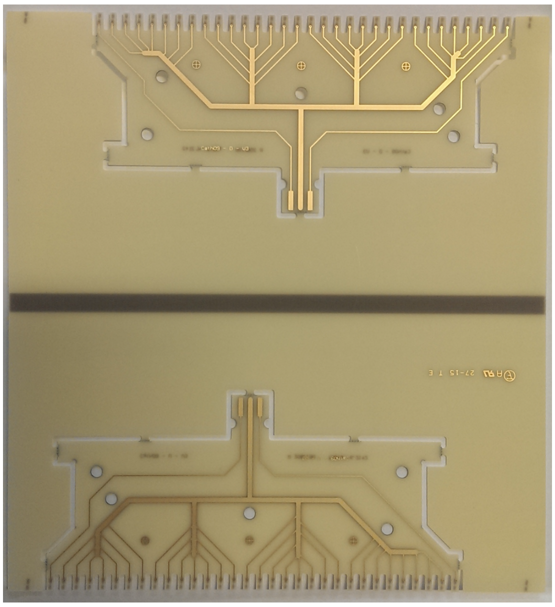

Figure 3.2: Wire pcb: FR4 printed circuit board on which the wires are soldered

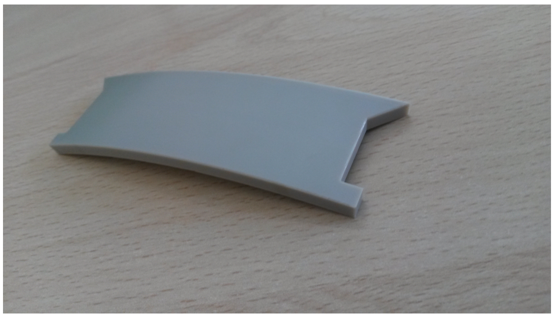

Figure 3.3: Peek spacer

sinusoidal high voltage. The change of the capacitance between adjacent wires induces an electric signal with a frequency depending on the wire tension.

3.1.2 The choice of Fill Gas

The choice of filling gas for a proportional chamber is governed by several factors: low working voltage, high gas gain, good proportionality and high rate capability. In general these conditions are met by using a gas mixture rather than a pure one. For a minimum working voltage, noble gases are usually chosen since they require the lowest electric field intensities for avalanche formation. MEG II Drift Chamber uses a Helium based gas mixture. The choice of Helium, is very advantageous, because of its large radiation length ($X_0 \simeq 5300\ m$ at STP), which ensures a small contribution in terms of multiple scattering, that is a very important feature in low momentum measurements.

A small amount (10%) of Isobutane used as quencher is required to avoid self-sustained discharge. In fact, excited Helium atoms formed in avalanche can give rise to high energy photons capable of ionizing the cathode and causing further avalanches. The molecules of the gas absorb the radiated photons and dissipate this energy through dissociation or elastic collision. A percentage of 10% is sufficient even though it raises the primary ionization number to $\sim 13/cm$ and lowers the mixture X_0 to ~ 1300 m. Unfortunately, the use of an organic quencher results in further problems after high fluxes of radiation have been absorbed. The recombination of dissociated organic molecules results in the formation of solid or liquid polymers which accumulate on the anode and cathode of detector, contributing to an ageing of the chamber. The fairly constant values of drift velocity in Helium based gas mixtures assures a linear time-distance relation, up to a very close distances to the sense wire. Given the spatial resolutions, which are obtained by timing only the first drifting electrons, one can aim at improving it by using the cluster counting technique by timing all arriving ionization clusters and, thus, reconstructing their distribution along the ionization track. The Helium high ionization potential, 24.6 eV, is such that a crossing particle produces a small number of primary ions ($\sim 4.8/cm$). This, together with the lower value of drift velocity ($\sim 2cm/\mu s$), considerably helps the time separation between clusters. In conclusion, in order to keep the Coulomb multiple scattering to a minimum the MEG II DC requires high transparency: this is achieved using an ultra-low mass gas mixture with Helium and Isobutane (90:10) and very thin wires used as anode and cathode. The resulting radiation length per track turn is about $1.6 \times 10^3 X_0$.

3.1.3 High Voltage and gas system

The chamber operates at 1600 V applied to the anode wires, corresponding to a gain of a few times 10^5. Gas flow rate and gas pressure are controlled by a dedicated system. The gas quality control is performed by means of sensors measuring oxygen, moisture and Isobutane concentrations.

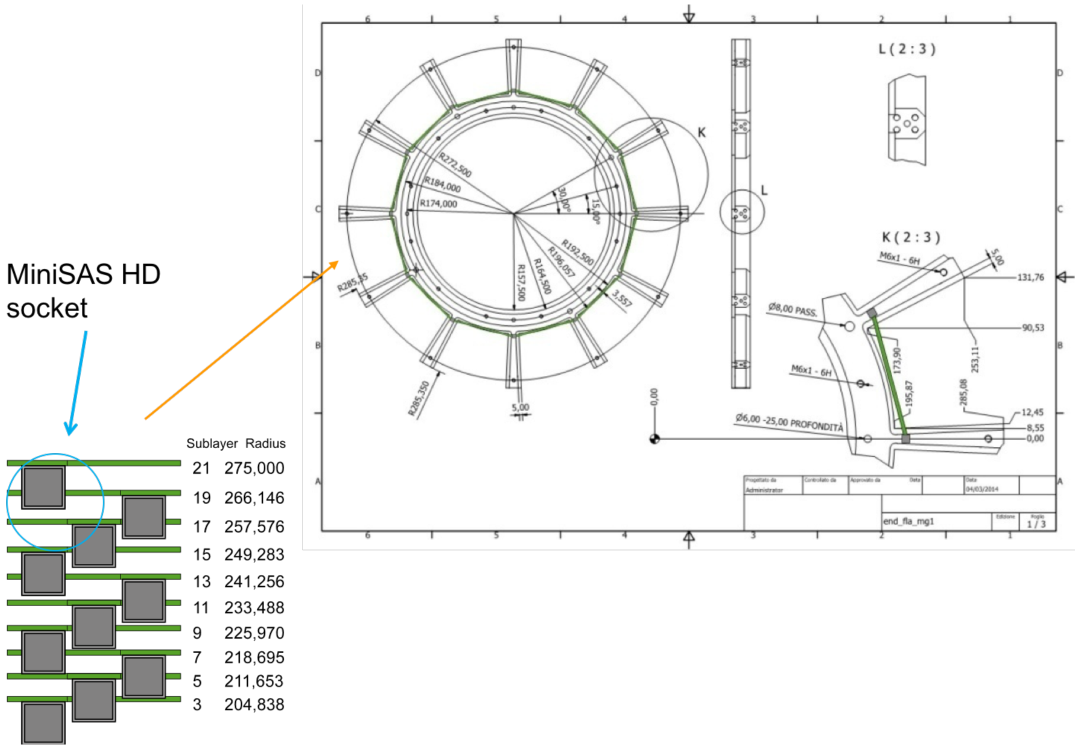

Figure 3.4: Drift Chamber end plate scheme

3.1.4 Electronics

In order to permit the detection of single ionisation clusters, the electronic readout interface has to process high speed signals. For this purpose, a high performance 8-channels Front End electronics has been designed and tested (42), (43) and it will be described in next chapter with more details.

The FE electronics boards are placed in each sector of the cylindrical drift chamber; in figure 3.4 the drift chamber end plate mechanical scheme, in which the boards will be inserted, is represented. Different connectors have been compared in relation to the amount of room on the DC end plates and on the digitizer frontal panel, as well different types of cables have been compared in order to reach the best bandwidth. The output connector has a MINI SAS socket (50). Due to the amount of area of Mini SAS socket and considering the available space between Drift Chambers Layers, we had to design three different board versions, one with the output connector on the right, one on the centre and the last on the left (see figure 3.5).

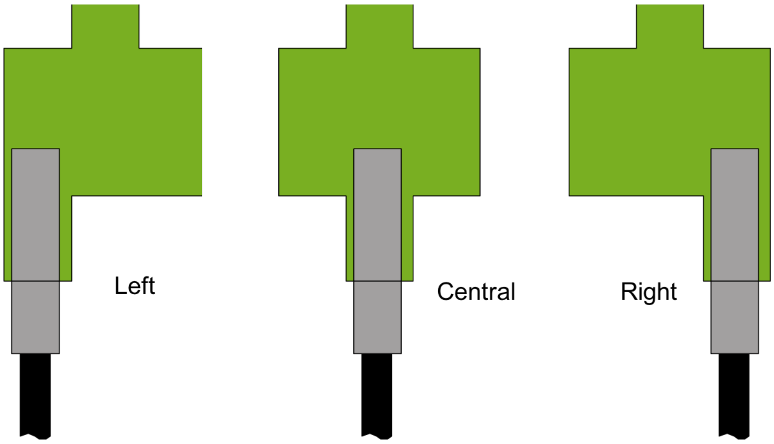

Figure 3.5: The three different FE card versions

Pre amplified differential signals are successively digitized by the DRS4 chip (46), at a (programmable) speed of 2 GSPS with an analog bandwidth of 1 GHz (47).

3.2 The wiring procedure at INFN of Lecce

A wiring system robot (26) has been fully designed and assembled in the cleaning room of Physics Department in the University of Salento and INFN of Lecce. It allows to stretch automatically the wires on PCB frames keeping under control the wire tension and pitch parameters, moreover the system fixes the wires on PCB by a contact less soldering. Since the MEG II Drift Chamber has a high wire density (12 wires/cm^2), therefore the classical feed-through technique, as wire anchoring system, is hard to be implemented, thus the development of a new wiring strategies is necessary. The large number of wires and the stringent requirements on the precision of the wire position, better than 20 μm, imposes the use of an automatic system to operate all the wiring phases.
The wiring robot has been designed in order to:

- managing a very large number of densely spaced wires;
- monitoring the solder quality of the wire to the supporting PCBs;
- applying the wires mechanical tension and maintaining it constant and uniform through the whole chamber;

- monitoring the wire positions and their alignments within a few tens μm.

These requirements are satisfied by three systems:

1. **A Wiring system** that uses a semi-automatic wiring machine to simultaneously wire the multi-wire layer with a high degree of control on the wire mechanical tension (better than 0.2 g) and on the wire position (of the order of 20 μm) . Each multi-wire layer is made up of 32 parallel wires placed on specially designed PCBs properly oriented at the desired stereo angle.

2. **A soldering system** composed of an Infra Red (IR) laser soldering system, designed to be contact-less.

3. **An automatic handling system** which extracts the multi-wire layers from the wiring system and places them in a storage and transport frame, to be sent to the assembly station at the INFN Pisa.

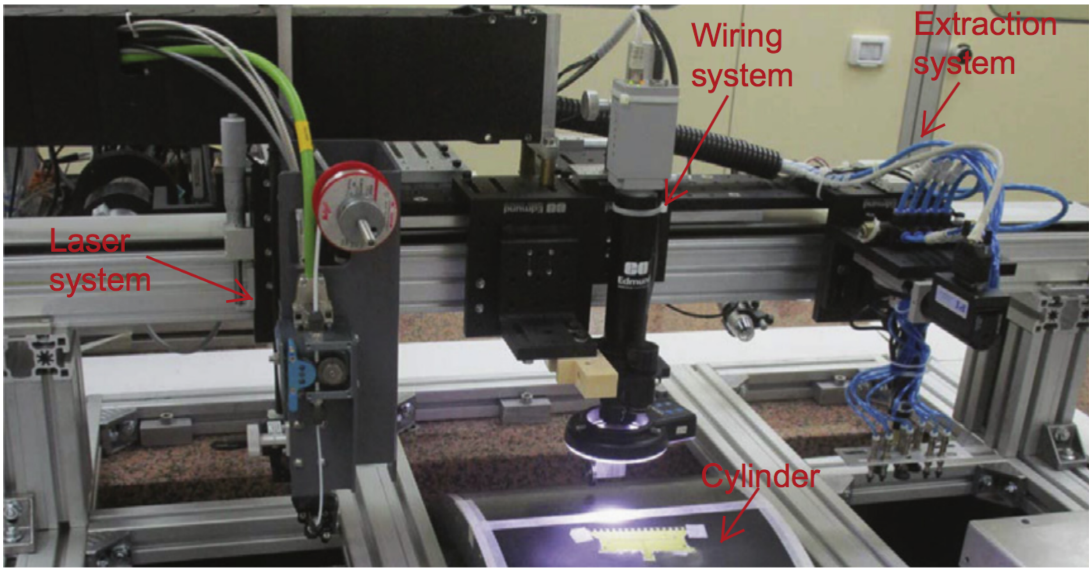

Figure 3.6: The wiring robot

A real-time system (26), based on a National Instrument Compact RIO platform (51), controls the three systems simultaneously, sequencing and synchronizing all the different operations. The Compact RIO platform includes a range of embedded controllers with two processing targets:

- a real-time processor for communication and signal processing
- a user-programmable FPGA to implement high-speed control and custom timing

The entire system is shown in figure 3.6.

3.2.1 Wiring system

The purpose of the wiring system is the winding of a multi-wire layer made up of 32 parallel wires. In order to achieve a multi-wire layer (see figure 3.7), two PCBs, aligned and oriented at the proper stereo angle, are placed back-to-back on the winding cylinder. The multi-wire layer is obtained in a single operation by winding along a helical path the same wire 32 times around the cylinder with a pitch corresponding to the wire PCBs spacing. The pitch is made by a system of synchronized stepper motors through the Compact RIO system and controlled by a digital camera with a software developed with LabView. The wire mechanical tension is monitored by a high precision strain gauge and corrected with a real-time feedback system acting on the wire spool electromagnetic brake.

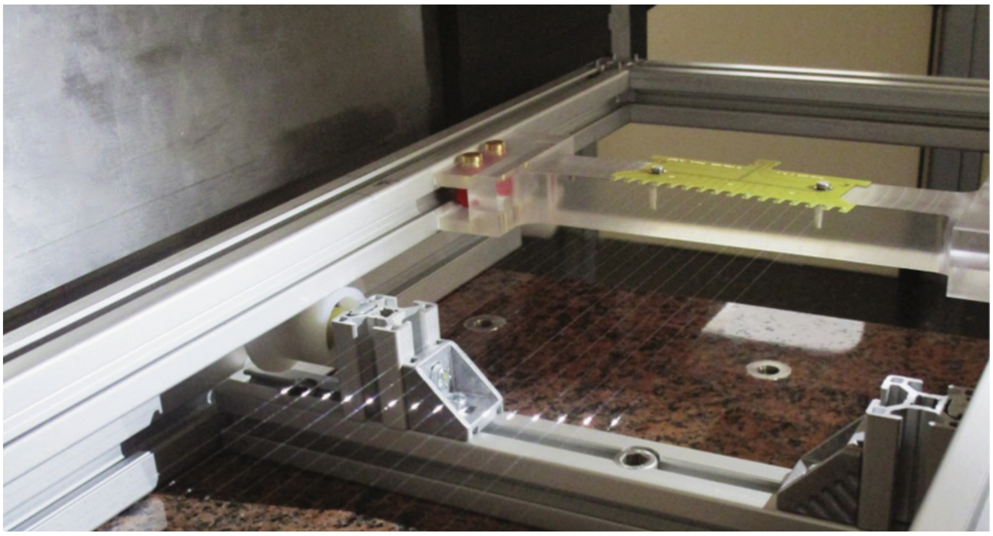

Figure 3.7: A multiwire frame

The wire tension variations are of order of ± 1.5 g, without the feedback system, because of the mechanical tolerances. The feedback system reduces these variations to less ± 0.5 g (see figure 3.8).

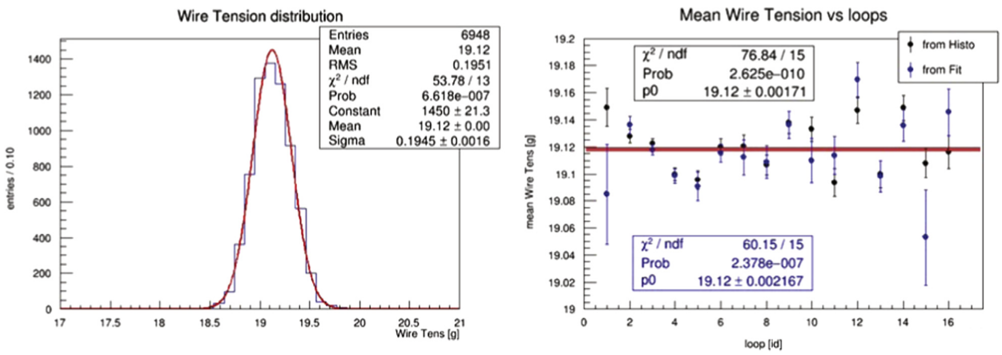

Figure 3.8: Left: the distribution of the wire tension during the winding. Right: average wire tension for each loops.

3.2.2 Soldering system

The soldering phase is executed by an IR laser soldering system (52) controlled by the Compact RIO. It allows also to synchronize the positioning system by using a pattern matching software developed with the LabVIEW program to localize the soldering pad.

3.2.3 Automatic handling system

The wound layer of soldered wires around the cylinder is unrolled and detensioned for storage and transport. This is accomplished with an automatic device. The first wire PCB is lifted off from the cylinder surface with a linear actuator connected to a set of vacuum operated suction cups and placed on the storage and transport frame. The unrolling is accomplished by synchronizing the cylinder rotation with the linear displacement of the frame. Once the layer of soldered wires is completely unrolled, the second wire PCB is lifted off from the cylinder, as the first one, and placed on the frame. The wires of the frame are examined stored and ready for the transportation (figure 3.9) towards DC assembly station in Pisa. The wiring informations relative to each frame are stored in a database (see figure 3.10) in order to share the informations with Pisa Group.

3.3 Expected performances

As preliminary tests, the spatial resolution and the ageing robustness of the chamber have been measured on prototypes. The high transparency of the chamber has the

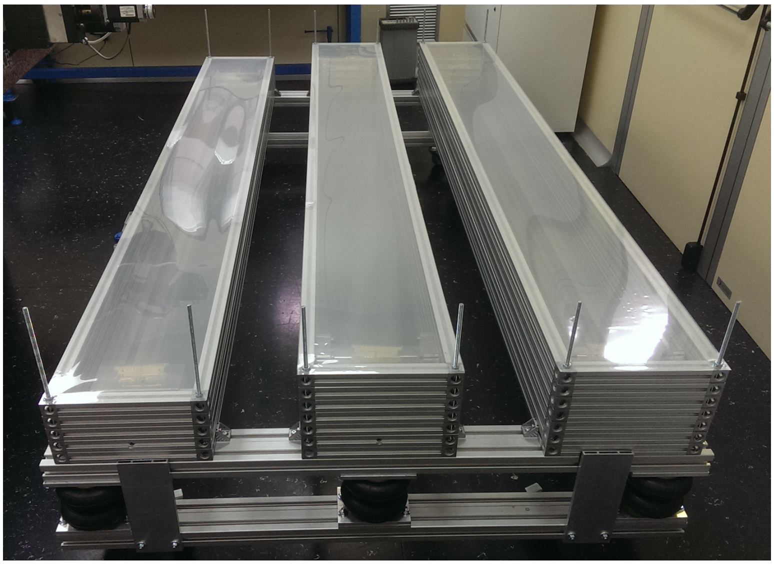

Figure 3.9: Some layers ready for transportation towards Pisa station

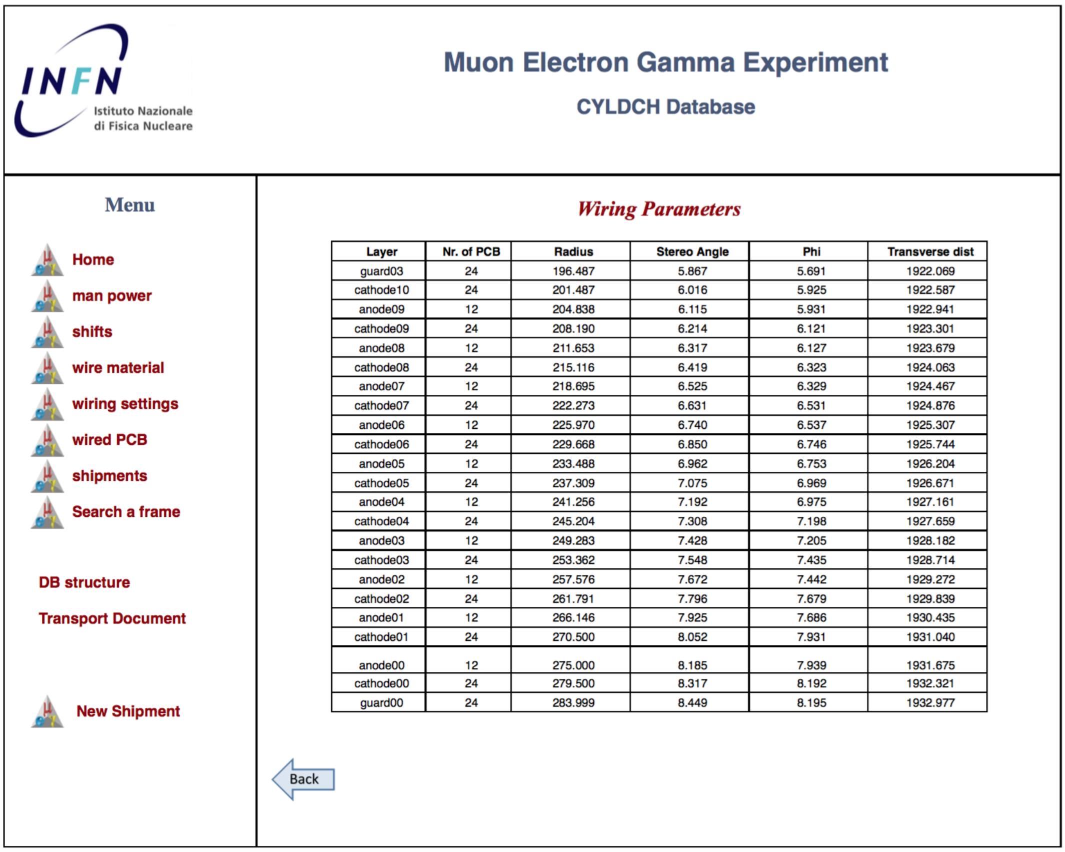

Layer	Nr. of PCB	Radius	Stereo Angle	Phi	Transverse dist
guard03	24	196.487	5.867	5.691	1922.069
cathode10	24	201.487	6.016	5.925	1922.587
anode09	12	204.838	6.115	5.931	1922.941
cathode09	24	208.190	6.214	6.121	1923.301
anode08	12	211.653	6.317	6.127	1923.679
cathode08	24	215.116	6.419	6.323	1924.063
anode07	12	218.695	6.525	6.329	1924.467
cathode07	24	222.273	6.631	6.531	1924.876
anode06	12	225.970	6.740	6.537	1925.307
cathode06	24	229.668	6.850	6.746	1925.744
anode05	12	233.488	6.962	6.753	1926.204
cathode05	24	237.309	7.075	6.969	1926.671
anode04	12	241.256	7.192	6.975	1927.161
cathode04	24	245.204	7.308	7.198	1927.659
anode03	12	249.283	7.428	7.205	1928.182
cathode03	24	253.362	7.548	7.435	1928.714
anode02	12	257.576	7.672	7.442	1929.272
cathode02	24	261.791	7.796	7.679	1929.839
anode01	12	266.146	7.925	7.686	1930.435
cathode01	24	270.500	8.052	7.931	1931.040
anode00	12	275.000	8.185	7.939	1931.675
cathode00	24	279.500	8.317	8.192	1932.321
guard00	24	283.999	8.449	8.195	1932.977

Figure 3.10: A database page in which wiring parameters are collected

Table 3.1: MEG II Expected Drift Chamber performances with respect to MEG

Resolution	MEG I	MEG II
p_e (keV)	306	130
ϑ_e (mrad)	9.4	5.3
φ_e (mrad)	8.7	4.8
e^+ efficiency (%)	40	88

drawback of a poor ionisation statistics, which results in a bias and a worsening of resolution in the estimate of the impact parameter in drift cells. For a clean measurement of the single-hit resolution, several drift chamber prototypes were tested in a cosmic ray facility set up at INFN section of Pisa (49) (48). The measured single-hit resolution is 110 μm, averaged over a large range of angles and of impact parameters. The high bandwidth electronics enables the possibility of improving the single-hit measurements by identifying individual ionization encounters. The longitudinal coordinate of hits will be determined by exploiting the stereo angle, with a resolution $\sigma_z = \sigma_r / sin\theta_s \simeq 1\ mm$. On the other hand, the extremely high positron rate in the MEG II drift chamber (up to $\sim 30\ kHz/cm^2$) will induce a huge amount of charge collected in the hottest portion of the innermost wire ($\sim 0.5\ C/cm$). Since at such values of collected charge wire chambers can present inefficiencies and loss of gain, laboratory tests on prototypes in a dedicate irradiation facility set up at INFN of Pisa were performed (49), (48). Tests returned sustainable gain losses of less than 20% per DAQ year in the hottest few centimetres of the innermost wires.

Using the results obtained with prototypes as input for the simulation of the detector, the expected Drift Chamber performance compared with the present chamber are summarized in table 3.1. The high efficiency of the drift chamber and its optimised matching to the timing counters result in an efficiency of the positron reconstruction improved by a factor two. The resolutions on the positron kinematic variables are improved as well, mainly because of the higher transparency of the detector, the better single hit resolution and the increase of larger hits number.

4

Front End Electronics for Drift Chamber signal acquisition

In this chapter the drift chamber signal characteristics is discussed in relation to the Front End electronics design. After some principles of DC operational, the chapter focus on the FE specification in order to acquire signal in the MEG II DC and above all, identify ionization clusters in the digitized waveforms with Cluster Timing algorithms. Some FE prototypes have been designed and tested, finally the prototype with the best performances has been chosen for developing the multichannel board. Additionally some measurements on the cell impedance are showed and discussed with the aim of minimizing signal reflections in the FE electronics.

4.1 Drift Chamber fundamentals

A Multi Wire Proportional Chamber (MWPC) is a device capable of localizing particle trajectories with a good resolution and it is widely used in high energy physic experiments. This device operates on the same basic principles as the simple proportional counter (53), (54). The basic MWPC consists of a plane of equally spaced anode wires centred between two cathode planes. Figure 4.1 illustrates this configuration schematically. If a negative voltage is applied to the cathode planes, an electric field arises. Near the anode wires the field takes on a 1/r dependence similar to the single wire cylindrical proportional chamber. When a charged particle passes through a gas, it will interact electromagnetically with nearby atomic electrons, resulting in the creation of

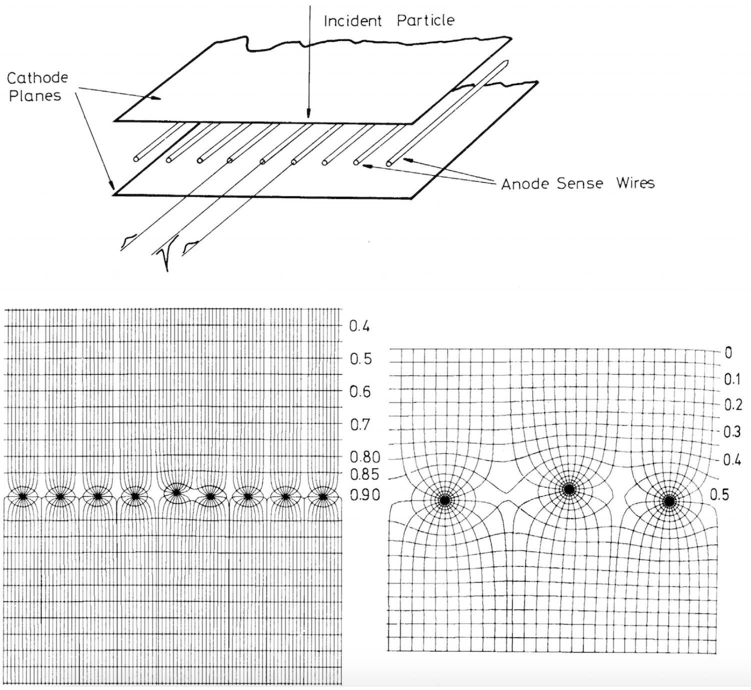

Figure 4.1: Multi Wire Proportional Chamber structure and electric field

electron/ion pairs along its path. They drift along the field lines (see figure 4.1) toward the nearest anode wire and opposing cathode. Upon reaching the high field region, the electrons are accelerated and produce a Townsend avalanche (this mechanism will be explained later in more details). The positive ions liberated in the multiplication process then induce a negative signal on the anode wire. The total charge is proportional to the ionization produced by the particle crossing the detector (proportional chamber (53)). The spatial information is obtained by measuring the drift time of the electrons coming from an ionizing event. Considering, a trigger and supposing the knowledge of the drift velocity u, the distance from the sensing wire to the point of generation of the electrons is:

$$x = \int_{t_0}^{t_1} u(t, E)dt \tag{4.1}$$

where t_0 is the arrival time of the particle and t_1 it the time at which the pulse appears at the anode. It is clear that it is highly desirable to have a constant drift velocity u, and hence a constant electric field, so as to have a linear relationship between time and distance.

By combining measures from cells crossed by computing pulses from all the wires, the particle trajectory can be reconstructed.

4.1.1 Primary and total ionization

The number of electron/ion pairs created during the gas ionization, depends on the energy of the particle and the type of gas, while the encounters with the gas atoms are purely random and are characterized by a mean free flight path λ between ionizing encounters given by the ionization cross-section per electron σ_I and the density N of electrons:

$$\lambda = 1/(N\sigma_I)$$

Therefore, the number of encounters along any length L has a mean of L/λ, and the frequency distribution is the Poisson distribution:

$$P(L/\lambda, k) = \frac{(L/\lambda)^k}{k!} e^{-\frac{L}{\lambda}} \tag{4.2}$$

From 4.2 we obtain the probability of having zero encounters along a track length L:

$$P(L/\lambda, 0) = e^{-\frac{L}{\lambda}} \tag{4.3}$$

If a gas counter with sensitive length L is set up so that the presence of even a single electron in L will always give a signal, then its inefficiency may be identified with expression 4.3; the equation 4.3 provides a method for measuring λ.

When an ionizing particle passes through a gas, free electrons and ions are produced in amounts that depend on the atomic number, density and ionization potential of the gas, and on the energy and charge of the incident particle. The number of primary electron pairs per cm is called N_p. The created electrons may have sufficient energy to ionize further and create secondary electron-ion pairs. The overall outcome of the two processes is called total ionization; the total number of electron-ion pairs per cm is denoted by n_T. The total number of produced ion pairs can be written as:

$$n_T = \frac{\Delta E}{W_i}$$

where ΔE is the total energy given by the particle to the medium and W_i the average energy for producing a couple, that is bigger than the gas ionization energy.

Table 4.1: Table of some properties of some noble and molecular gases commonly used for particle detectors

Gas	Density $mg\ cm^{-3}$	E_x (eV)	E_i (eV)	W_i (eV)	dE/dx M.I.P. $(keV cm^{-1})$	N_P (cm^{-1})	N_T (cm^{-1})
He	0.179	19.8	24.6	41.3	0.32	3.5	8
Ne	0.839	16.7	21.6	37	1.45	13	40
Ar	1.66	11.6	15.7	26	25	2.53	97
Xe	5.495	8.4	12.1	22	41	6.87	312
CH_4	0.667	8.8	12.6	30	28	1.61	54
C_2H_6	1.26	8.2	11.5	26	48	2.91	112
iC_4H_{10}	2.49	6.5	10.6	26	90	5.67	220
CO_2	1.84	7.0	13.8	34	35	3.35	100
CF_4	3.78	10.0	16.0	54	63	6.38	120

Table 4.1 (55) illustrates the properties of noble and molecular gases at normal temperature and pressure (NTP: 20°C, one atm). E_x, E_i are the first excitation and ionization energy, W_i average energy per electron-ion pair; dE/dx, N_P, N_T, primary and total number of electron-ion pairs per cm, for unit charge minimum ionization particle (M.I.P.).

In case of gas mixture, the contribution of each component is proportional to the percentage in the mixture:

$$N_{pMixture} = \sum_j N_{pj} \cdot w_j$$

4.2 Transport of Electrons and Ions in Gases

For ionization detectors the understanding of motion of electrons and ions in gases is very important as these factors influence the operating characteristics of the detector.

4.2.1 Drift and Mobility

In the presence of an electric field, the electrons and ions freed by radiation are accelerated along the field lines towards the anode and cathode respectively. This acceleration is interrupted by collisions with the gas molecules which limit the maximum average velocity. The average velocity attained is known as the *drift velocity* of the charge and is overlapped its normal random movement. The drift velocity can be expressed using the mobility of a charge and the electric field:

$$\mu = \frac{u}{E} \tag{4.4}$$

For ideal gases, in which the moving charges remain in thermal equilibrium, the mobility can be shown to be related to the diffusion constant:

$$\frac{D}{\mu} = \frac{kT}{e} \tag{4.5}$$

Unlike, positive ions, the mobility for electrons is much greater and is found to be a function of E. Velocities as high as few times 10^6 cm/s can be generally obtained, the electric field at this point are generally on the order of $1kV/cm$.

4.2.2 Avalanche effect

The increase of the electric field closed to a wire $\propto \frac{1}{r}$ is of some kVolt/cm and it let the electrons acquire enough energy between two collisions to produce excitation and ionization: if the electron reaches an energy equal to ionization potential of the gas, a ion pair is formed. The fractional increase in the number of electrons per unit path length is governed by the Townsend Equation. Initially a single electron is present, after a free mean path λ an ion-electron couple is produced with two electrons that can produce other ionizations, after $2/\alpha$ four electrons will be and so on. Thus, if n is the electrons number at a certain position, after a path dx the number will increase of:

$$dn = n\alpha dx$$

integrating this expession:

$$M = \frac{n}{n_0} = e^{\alpha x}$$

where n_0 is the initial electrons number and M is the multiplication factor or gain. In more general cases, where electric field is not constant α depends from x, so the multiplication factor is obtained:

$$M = \int_{-x_1}^{x_2} \alpha(x)\, dx$$

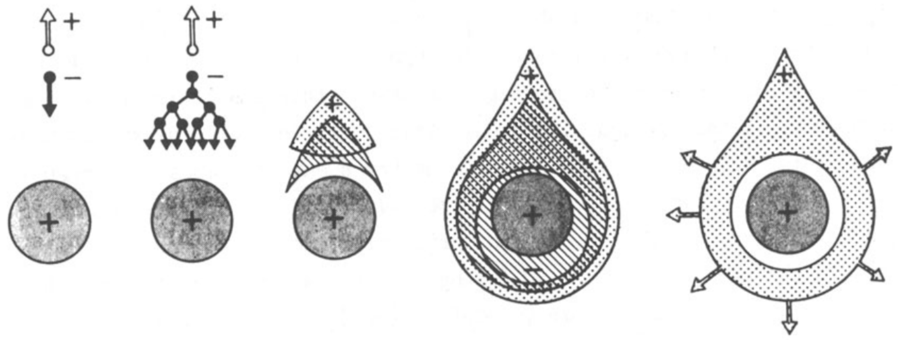

Figure 4.2: Ionization and avalanche process around a wire

The multiplication factor can not increase indefinitely, there is a phenomenological limit called Rather condition:

$$\alpha x \approx 20$$

an operational limit is $M \approx 10^6$.

If the total collected charge is proportional to the number of primary electrons, then the chamber is said to operate in the proportional mode. The proportionality constant is called multiplication factor and it depends exponentially on the applied high voltage. In general, the amplification is a statistical process which for a cylindrical geometry is well described by a Polya distribution (56). The electron avalanche is rapidly ($\sim$nsec) collected by the wires, the positive ions, leftover in the trail of multiplying electrons, move in opposite direction toward the cathode, resulting in a negative signal on the wire where the avalanche originated (figure 4.2). In principle, each wire could act as an individual detector and the way to read those electric signals is to connect each wire to a circuit which can include an amplifier, a discriminator and a digitizer (Analog to Digital Converter or Time to Digital Converter).

4.3 Time development of the signal

The pulse signal on the electrodes of ionization devices is formed by induction due to the movement of the ions and electrons as they drift towards the cathode and the anode, rather than by the actual collection of the charges itself. In order to analyze the time development of the detected signal we consider the simple case that consists in a drift

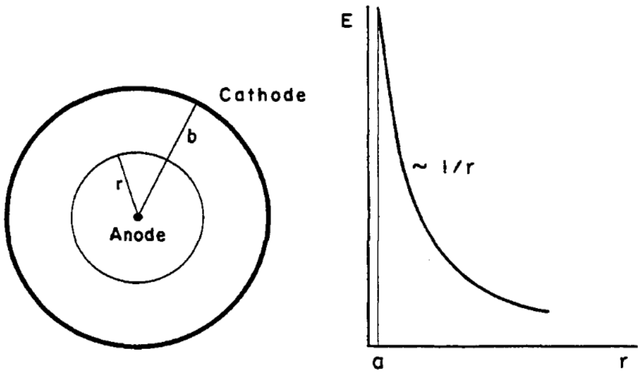

Figure 4.3: Simple drift tubes: a is the radius of wire (anode), b is the radius of the cathode (on the left) and the shape of the electric field around the thin anode (on the right)

tube with (cathode) radius b and wire radius a (Figure 4.3) that can be assimilated to a proportional counter. In this geometric and electrostatic conditions the electric field and the electric voltage versus the distance from the axis are:

$$E(r) = \frac{CV_0}{2\pi\varepsilon}\frac{1}{r}$$

$$\varphi(r) = -\frac{CV_0}{2\pi\varepsilon} ln\frac{r}{a}$$

where r is the radial distance fro the wire, V_0 the applied voltage, ε the dielectric constant of the gas and $C = \frac{2\pi\varepsilon_0}{ln\frac{b}{a}}$ the capacitance per unity length of this configuration. Suppose that a charge q located at a distance r from the wire moves a distance dr, the change in potential energy is:

$$dE = lCV_0 dV = q\frac{d\varphi(r)}{dr}dr \tag{4.6}$$

The detected pulsed signal, negative on the anode and positive on the cathode, is the consequence of the change in energy of the system due to movement of charges, so the induced signal is:

$$dv = \frac{q}{lCV_0}\frac{d\varphi(r)}{dr}dr \tag{4.7}$$

For the cylindrical proportional counter, we assume the multiplication takes place at a distance r' from the anode. The total induced voltage from the electrons and ions is respectively:

$$V^{-} = -\frac{q}{lCV_0}\int_{a+r'}^{a}\frac{d\varphi}{dr}dr = -\frac{q}{2\pi\varepsilon l}ln\frac{a+r'}{a} \quad (4.8)$$

$$V^{+} = \frac{q}{lCV_0}\int_{a+r'}^{b}\frac{d\varphi}{dr}dr = -\frac{q}{2\pi\varepsilon l}ln\frac{b}{a+r'} \quad (4.9)$$

Considering the two contributions, the ratio:

$$\frac{V^-}{V^+} = \frac{ln\frac{a+r'}{a}}{ln\frac{b}{a+r'}}$$

with the typical numerical values $a = 10\ \mu m$, $b = 10\ mm$, $\lambda = 1\ \mu m$, this ratio is nearly 0.013; this means that the electron contribution to the signal is $\sim 1\%$, so the signal almost entirely due to ions and the motion of the electrons can be ignored. With this simplification we can now calculate the time development of the pulse (53), (54)

$$v(t) = \int_{r(0)}^{r(t)}\frac{dV}{dr} = -\frac{q}{2\pi\varepsilon l}ln\frac{r(t)}{a} \quad (4.10)$$

Considering that for ions the drift velocity is proportional to the mobility μ and the electric field:

$$\frac{dr}{dt} = \mu E(r) = \frac{\mu^+ CV_0}{2\pi\varepsilon}\frac{1}{r}$$

and therefore:

$$rdr = \frac{\mu CV_0}{2\pi\varepsilon}dt$$

Since the positive ions come from the region close to the anode, we can set $r(0) = 0$, so the integration yields:

$$r(t) = \left(a^2 + \frac{\mu CV_0}{\pi\varepsilon}t\right)^{\frac{1}{2}}$$

Substituing in eq 4.10 the voltage time dependent signal is:

$$V(t) = -\frac{q}{4\pi\varepsilon l}ln\left(1 + \frac{\mu CV_0}{\pi\varepsilon a^2}t\right) = -\frac{q}{4\pi\varepsilon l}ln\left(1 + \frac{t}{t_0}\right) \quad (4.11)$$

where $t_0 = \frac{\pi\varepsilon}{\mu CV_0}$. For this distance, the total drift time T, obtained from the condition $r(T) = b$, is:

$$T = t_0(b^2 - a^2) \quad (4.12)$$

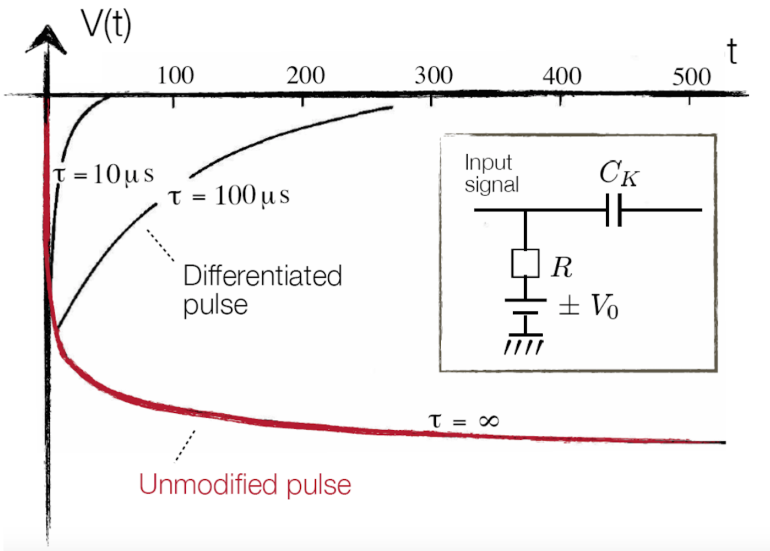

Figure 4.4: Time development of the pulse in a proportional chamber (in red). T is the total drift time of positive ions from anode to cathode. The pulse shape obtained with several differentiation time constants (RC_K circuit) is also shown.

This function is graphed in figure 4.4, for some typical values. Since it is not necessary to use the entire signal, the pulse is usually differentiated to shorten its duration. In this manner only the faster rising part of the pulse is exploited. Depending on the time constant $\tau = RC_K$ of the differentiator, the fall time of the resulting pulse will vary. The figure 4.4 shows some examples of pulse shape obtained by differentiation. At the limit for $R \to 0$, one speaks rather of a current signal than a voltage; this is given by:

$$i(t) = lC\frac{dv(t)}{dt} = -\frac{qC}{4\pi\varepsilon}\frac{1}{t+t_0} \tag{4.13}$$

The current is maximum for t = 0:

$$i_{max} = i(0) = -\frac{\mu^+ qC^2 V_0}{4\pi^2\varepsilon^2 a^2}$$

4.3.1 Avalanche signal simulation

The pulse expression has been reproduced using PSpice Simulator (57), a general purpose circuit simulation program for non linear transient and linear ac analysis, the

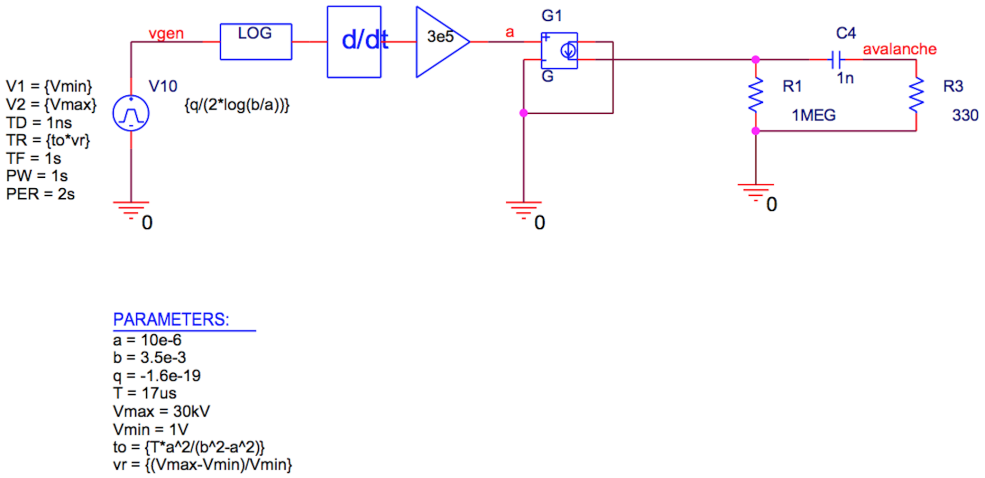

Figure 4.5: PSpice circuit schematic of a single pulse generated in a typical drift tube

circuit schematic is reported in figure 4.5. The signal is reproduced using mathematical blocks (logarithm and derivative) in order to obtain the analytic expression of the current 4.13; a gain block that simulates the gas gain (supposed 3×10^5) and a voltage controlled current source completes the circuit. The readout signal is taken on the termination resistance $R3$ which corresponds to the input of the electronics FE.

We suppose the simple case of a drift tube with cathode radius b and wire anode radius a (Figure 4.3). In our case, we assume the cathode wire radius $b = 3.5\ mm$ and the anode wire radius $a = 10\ \mu m$ in order to simulate the typical MEG II DC cell pulse signal. The circuit model is based on different behavioural blocks that reproduce the signal development as a function of the cell geometry and physic parameters such as the total drift time T. The resulting pulse avalanche signal, read out by a simple RC circuit representing the input of the FE, is depicted in figure 4.6 . This simulated pulse signal refers to a single electron and it will be used for the further studies on data analysis of the simulated waveforms.

4.4 High speed FE motivations

In drift chambers the Front-End electronics is a crucial parameter for device good time resolutions and, consequently, reasonable improvements on the spatial resolution, on the particle identification capabilities and on the trigger performances of the chamber

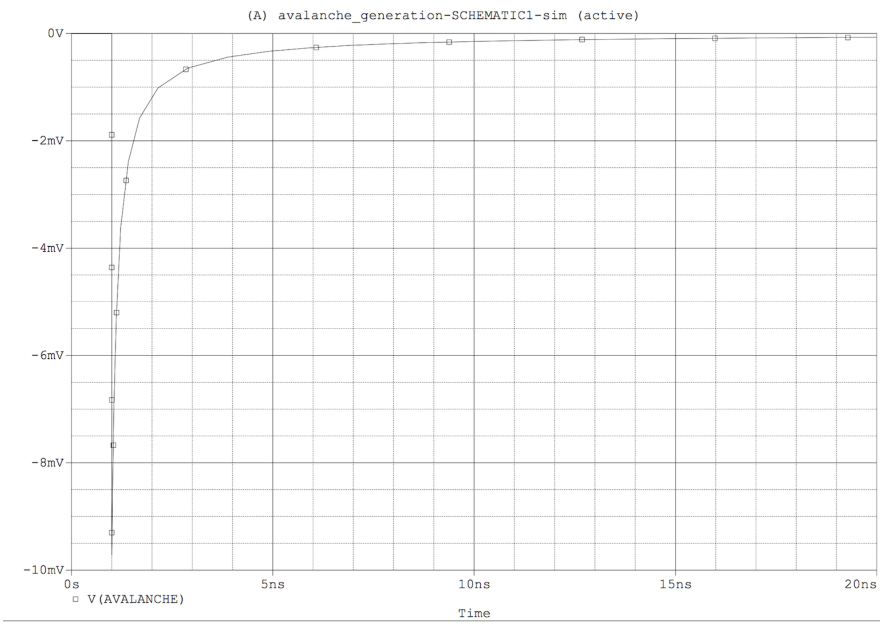

Figure 4.6: Single electron pulse simulated with PSpice Simulator

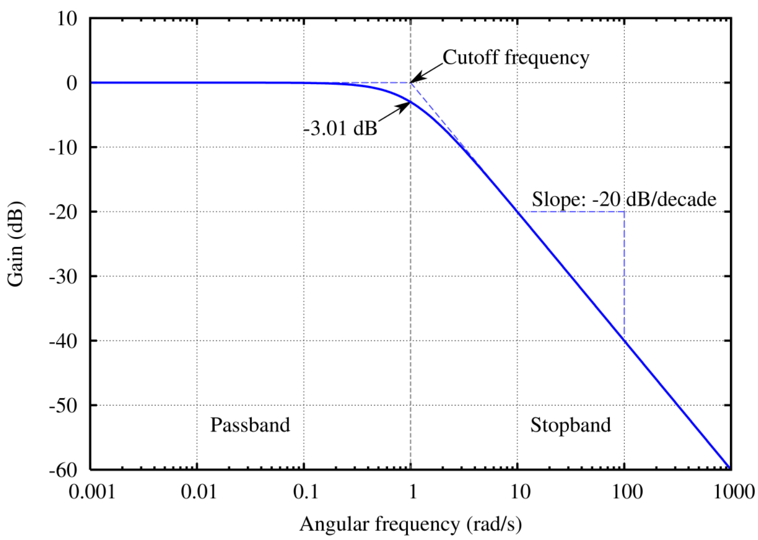

Figure 4.7: Tipycal frequency response curve. The frequency range between the points at which the curve falls by 3dB from its maximum value is defined as the bandwidth

itself. The electronic task is to process the signal coming from the detector. By theory, we know that a signal has different frequencies contributions and all frequencies play a role in the shaping of the signal. Thus, for an electronic device to faithfully treat the information contained in the signal, the device must be capable of responding uniformly to an infinite range of frequencies. In any circuit, of course, this is impossible. There will always be resistive and reactive components, which will filter out some frequencies more than others, so that the response it limited to a finite range of frequencies. This is also true for the interconnecting cables, as will be explained later. Figure 4.7 shows a typical flat response curve. The range of frequencies delimited by the points at which the response falls by 3 dB is defined ad the bandwidth; frequencies outside this range are attenuated or cutoff. A complete and faithful signal reproduction is desirable, but of course not absolutely necessary; what is important is that those part of the signal carrying information be reproduced with good fidelity. For the detector pulses, these parts are the amplitude and more particularly the fast rising edge, that is directly linked to the high frequency signal contributions.
In MEG II tracker it is very important to preserve fast rise time of the clusters in the waveforms throughout the electronic system because some clusters of the waveforms could not be recognized and Cluster Timing techniques could not be efficient. For these purposes it is necessary to have Front End electronics characterized by low distortion and large bandwidth, properly chosen in order to minimize also the noise contribution, in order to the acquired signal shows temporally separated pulses without overlapping and allow to apply Cluster Timing technique. A second problem, which will be treated in the next sections, is the distortion from reflections in the interconnecting cables. This arises because of the short duration of fast pulses relative to their time of transit in the interconnection.

Some studies on the typical DC signal characteristics have been carried out on both simulated and real signals. The pulse response of a simulated avalanche signal throughout a low pass filter at different cut frequencies (300 MHz, 600 MHz, 800 MHz) has been simulated in PSpice environment: figure 4.8 shows the electric schematic while figure 4.9 the pulse response thought an ideal low pass filter at different cut frequencies. As we can see by the graphs, the 800 MHz bandwidth system gets a faster time domain response, allowing to better recognize pulses due to different ionization clusters.

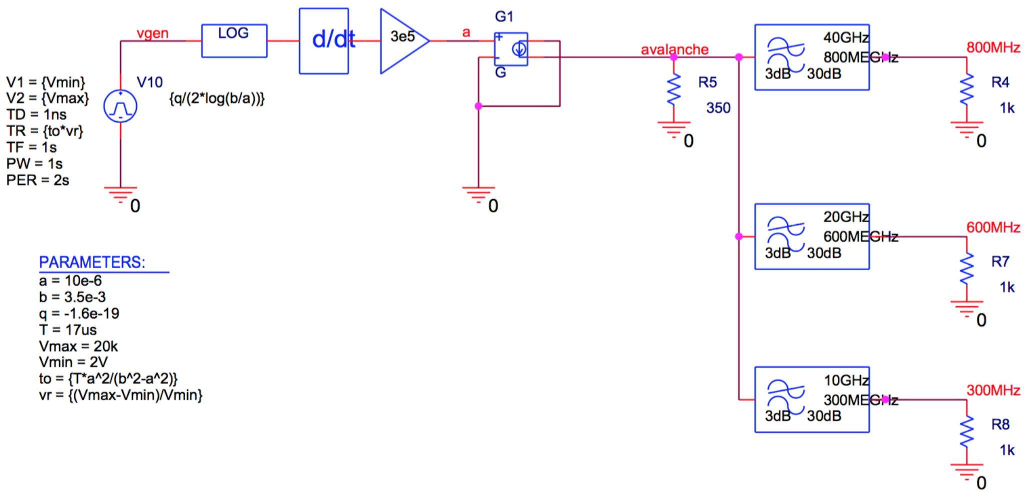

Figure 4.8: Pspice circuit Schematic of avalanche pulse processed by an ideal low pass filter at different bandwidths

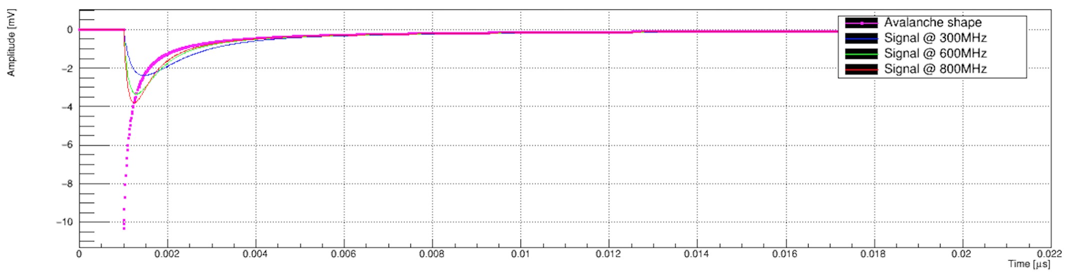

Figure 4.9: Avalanche pulse response after low pass circuit at different bandwidths (300-600-800 MHz)

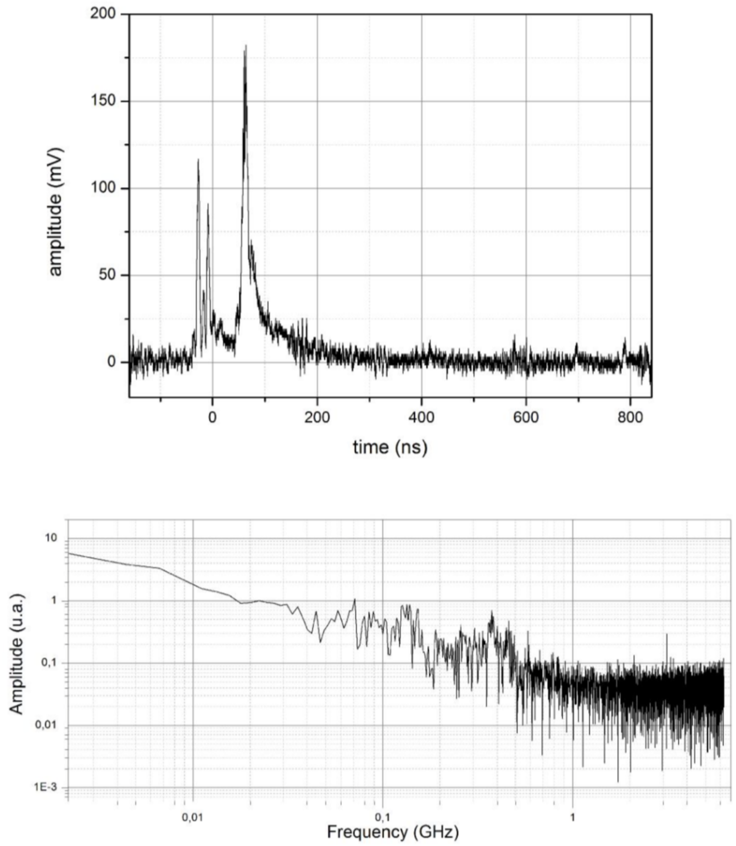

Figure 4.10: Typical Drift Chamber waveform (above) and Fourier transform (below) for an 8 mm diameter drift tube

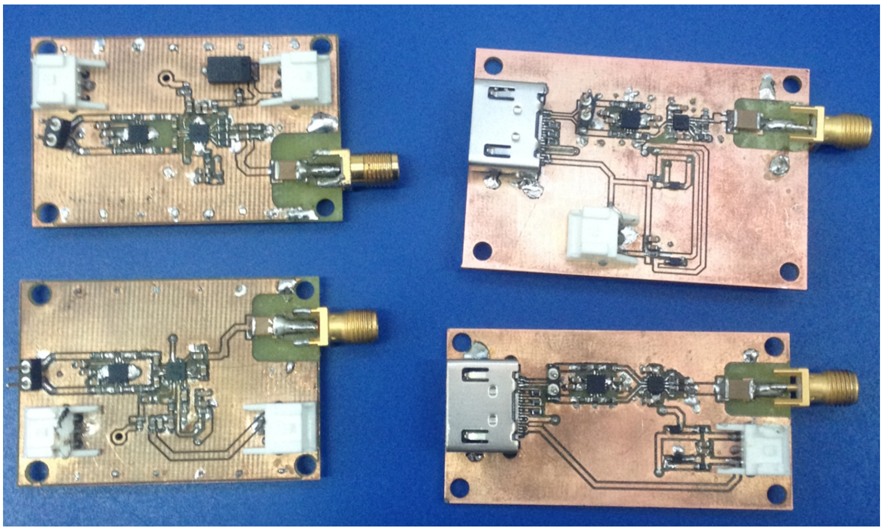

Figure 4.11: Front End single channel prototypes

Studies on real acquired signals show typical time separation between different ionization cluster going from few ns to few tens of ns, thus, if the electronics pulse response is larger than 1 ns some cluster could be lost. Figure 4.10 exhibits both a typical waveform acquired using a single 8 mm diameter drift tube with the 90% Helium: 10% Isobutane gas mixture and the related Fourier transform. The FFT in the bottom graph indicates that the main signal informations are included in a bandwidth of nearly 1 GHz. This result is used to set the overall bandwidth of the Front End electronics. In conclusion a high bandwidth and low noise electronics is necessary in order to meet the specifications discussed. In the next section, the multi-stage, low noise and low distortion Front End for MEG II Drift Chamber signal acquisition is described. The signals will be digitized by the MEG Wave Dream digitizer (47) and eventually Cluster Timing can be applied also in real time.

4.5 Front End board design and tests

The MEG II DC FE electronics has been designed in the INFN of Lecce electronics Laboratory in order to meet the specifications explained, by using commercial devices such as fast operational amplifiers that provide a gain-bandwidth of the order of 1 GHz. Different prototypes, depicted in figure 4.11, have been designed, realized and tested in order to perform frequency and time domain characterization. All the prototypes

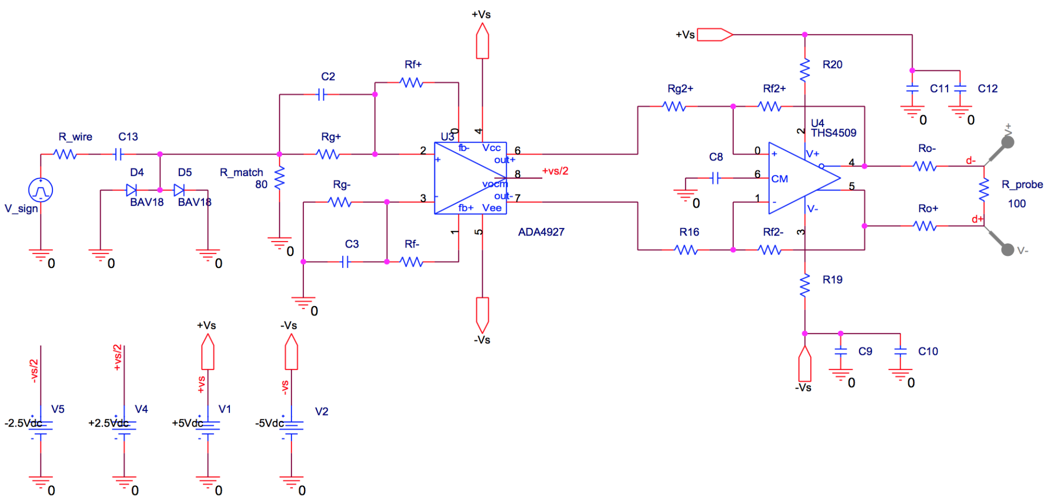

Figure 4.12: Front End single channel schematic

boards are realized using commercial amplifiers. Every board is based on a double gain stage: the output stage, used as output driver, is the same device for all the prototypes while they differ from the first gain stage device. The comparison was made about some relevant features:

- Gain, which must produce a suitable readout signal for further processing;

- Power consumption that must be limited;

- Bandwidth suited to the signal spectral density

- Fast pulse rise time response, in order to apply Cluster Timing techniques

The prototype with the best performance has been selected for the multi-channels amplification board and will be described following.

The single channel electronic schematic has been simulated by means of PSpice simulator (57) and it is represented in figure 4.12. The input network provides decoupling and protection while signal amplification is realized with a double gain stage made of ADA4927 and THS4509. Analog Device op-amp ADA4927 (58) works as first gain stage: it is a low noise, ultralow distortion, high speed, current feedback differential amplifier that is an ideal choice for driving ADCs. The current feedback architecture provides loop gain that is nearly independent of closed-loop gain, achieving wide

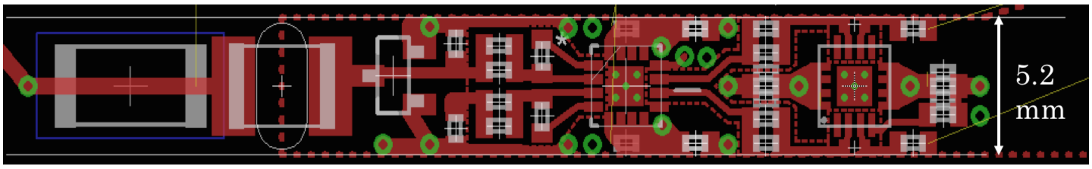

Figure 4.13: The design of DC FE single channel width

bandwidth, low distortion, and low noise (input voltage noise of only 1.3 nV/$\sqrt{Hz}$ at higher gains) and lower power consumption than comparable voltage feedback amplifiers. The THS4509 (59) by Texas Instruments is used as second gain stage and output driver. It is a wideband, fully differential operational amplifier with a very low noise (1.9 nV/$\sqrt{Hz}$), and extremely low harmonic distortion of -75 dBc HD_2 and -80 dBc HD_3 at 100 MHz. Slew rate is $6600V/\mu s$ with a settling time of 2 ns to 1% for a 2 V step; it is ideal for pulsed applications. The current consumption for each channel is 50 mA at voltage supply of $\pm$ $2.5V$.

Once selected the FE single channel we proceeded to design a multi-channels FE board by means of Eagle PCB Design Software (60). The multi channel electronics board is made of eight amplification channel, each channel is dedicated to amplify a single wire signal. Due to the amount of available area we have to shrink the channel width as much as possible. We reach 5.25 mm channel width and 30 mm channel length as represented in figure 4.13 where the single channel layout is depicted. An image of a card version realized is depicted in figure 4.14.

4.5.1 Output cable and pre-emphasis

The output of the FE is differential, in order to improve the noise immunity and it is connected to the Wave Dream Board (47) through a custom cabled designed ad hoc to meet the specifications. Different output cables have been compared and tested: the selected cable is by Amphenol Spectra Strip (61) (see figure 4.15(a)), made of shielded parallel pairs, each pair is individually shielded, overall a ground jacket is also present. For this kind of cable the maximum attenuation is 0.75 dB/m at 625 MHz. The cable is terminated with the connector MINI SAS (50) depicted in figure 4.15(b).

In order to balance the attenuation of the output cable, we implemented also a pre-emphasis on both gain stages. Test performed with spectrum Analyzer (Agilent 4396B) with a source -30 dBm show that FE the configuration with the pre-emphasis

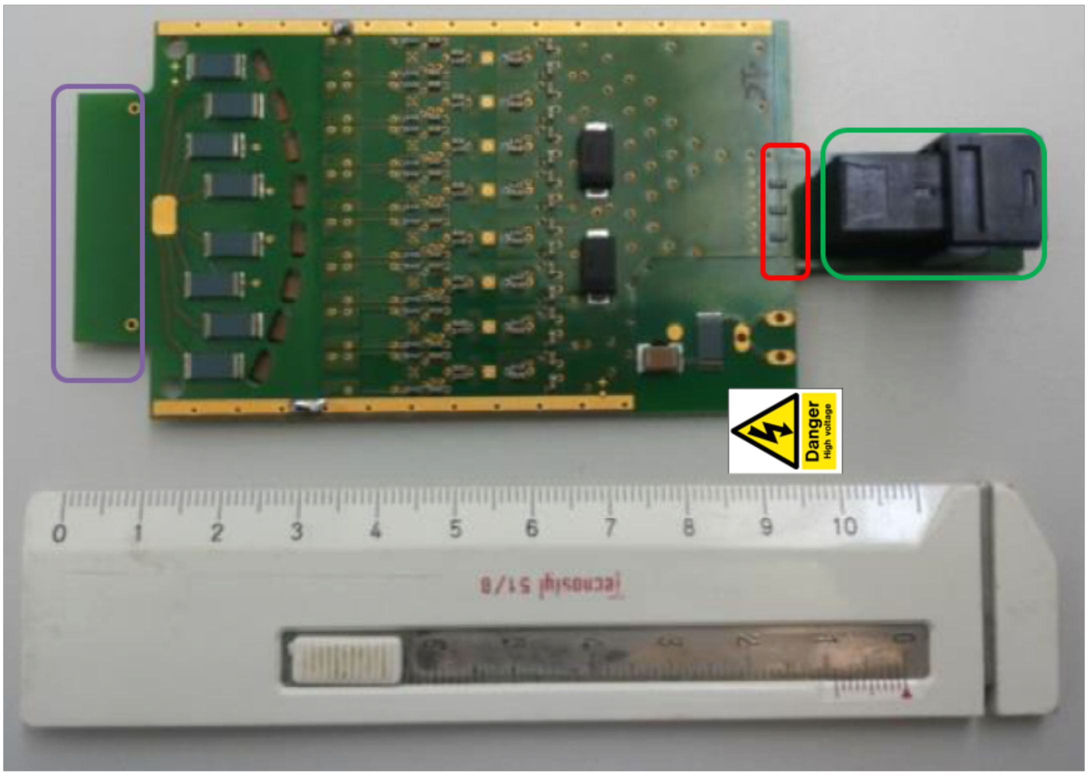

Figure 4.14: A multichannel prototype board realization

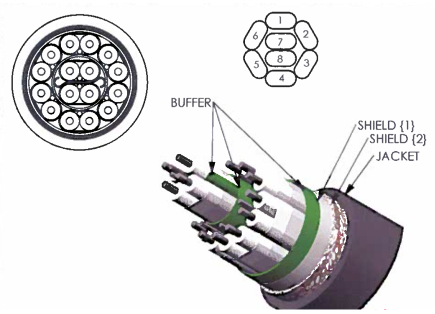

(a)

(b)

Figure 4.15: a)Amphenol Spectra Strip Output Cable; b)MINI SAS HD internal output connector

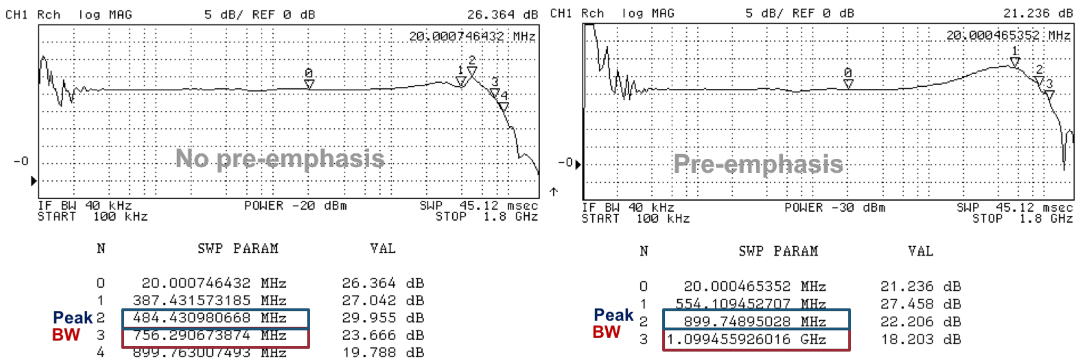

Figure 4.16: Single channel frequency response comparison between FE with pre-emphasis and without pre-emphasis performed by Spectrum Analyzer

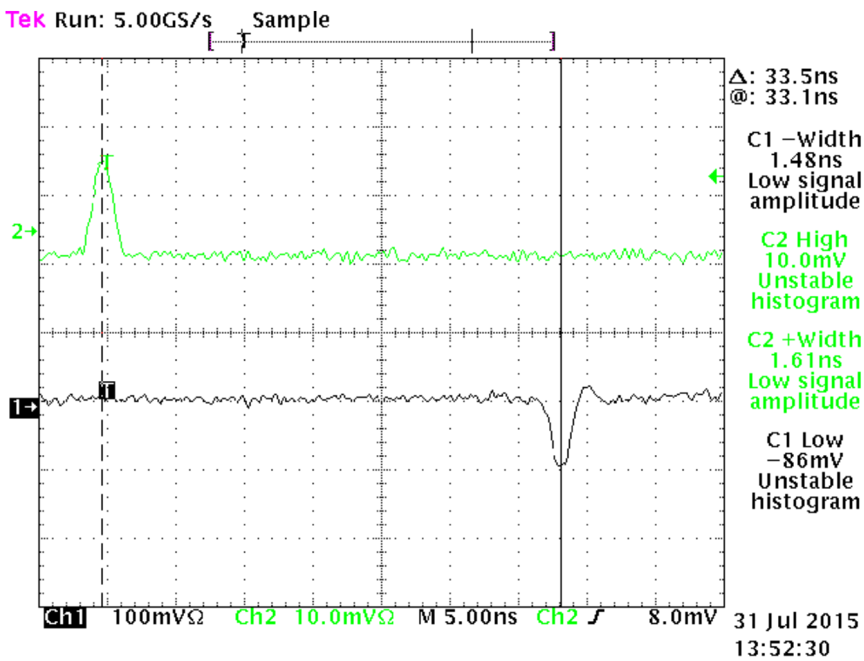

Figure 4.17: FE pulse response performed with a pulse generator and measured by an oscilloscope

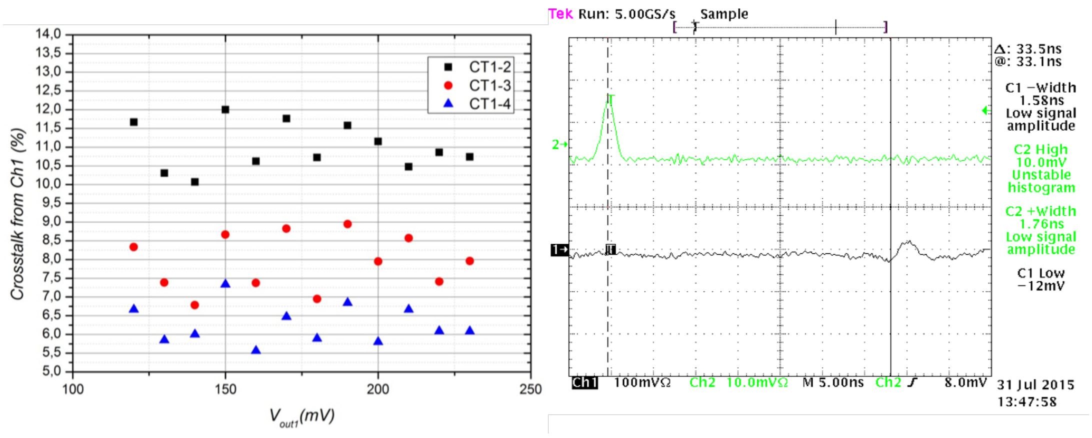

Figure 4.18: Crosstalk due to the first channel pulsed on the adjacent channels at different pulse amplitudes

implemented introduces a high frequency peak that compensates the output cable losses resulting in a overall a -3dB bandwidth of nearly 1 GHz as represented in figure 4.16, while FE time domain response using a pulse generator LeCroy 250 MHz Variable Edge Output Module 9211 is shown in figure 4.17

4.5.2 Crosstalk and signal integrity

The board designed processes high-speed signals: as speed increases, high frequency effects take over, and even the shortest lines can suffer from problems such as ringing, crosstalk and ground bounce, seriously hampering the response of the signal thus damaging signal integrity. In particular, due to the narrow channels distance, crosstalk effect is the most relevant cause of a spurious signal in adjacent channels of the board.

During a preliminary design of the multichannel board we measured a crosstalk of 10% as reported in figure 4.18 where a measurement in time domain and some measurements at different pulse amplitudes are reported. A reconfiguration of ground distribution improved the channel signal integrity reducing crosstalk up to 1%.

4.6 Drift Cell Impedence

The DC signal is assimilable as a current source connected to the sense wire at a certain distance from the pre-amplifier. Drift cells length ($\sim 2m$) impose to consider them as a transmission line: indeed indicating with f the signal frequency and c the

speed of light, for sufficiently high frequencies the wavelength $\lambda = f/c$ is comparable with the length of conductors in a transmission line. Therefore, we cannot neglect the impedance properties of the wires (distributed impedance circuits). A first issue is the signal reflection: if there is no impedance matching, due to the fast signal development, reflected signal can be confused as real ones. Another effect to take into account is that the small anode wire diameter (20 μm) has a non negligible resistance with a consequent signal attenuation.
Definitively, the Drift Chamber cell forms a lossy transmission line which is terminated with the real part of the characteristic impedance at the FE. Our study is focus on the drift cell characteristic impedance measurement in order to compute the FE input matching network. The drift cell transmission line can be treated as a cylindrical drift tube, because of its favourable geometrical constraints.

From transmission line theory we know that the ratio of the amplitude of a single voltage wave to its current wave is called characteristic impedance Z_0 of a transmission line:

$$Z_0 = \sqrt{\frac{R + j\omega L}{G + j\omega C}} \tag{4.14}$$

Note that the characteristic impedance is a frequency function and it depends only on the metal of the conductors, the dielectric material surrounding the conductors and the geometry of the line cross-section, which determine L, R, C and G; that are respectively inductance, resistance, capacitance, conductance per unity of length.

4.6.1 Input Matching Network

The drift tube can not be considered as non dispersive line and this sets considerable problems on the precise characteristic impedance determination: it is not a simple resistor, but it is in general a complex impedance, frequency dependent. Because drift tube frequency signal has different frequency components, we can not have a perfect matching, but we can consider a frequency range in which the line is matched in a average value and design the input matching network in these conditions. In our case of study the drift tube can be considered as a coaxial cable with the inner radius having diameter $a = 20\ \mu m$ and outer tube having diameter $b = 8\ mm$, the capacitance and the inductance per unity of length are respectively:

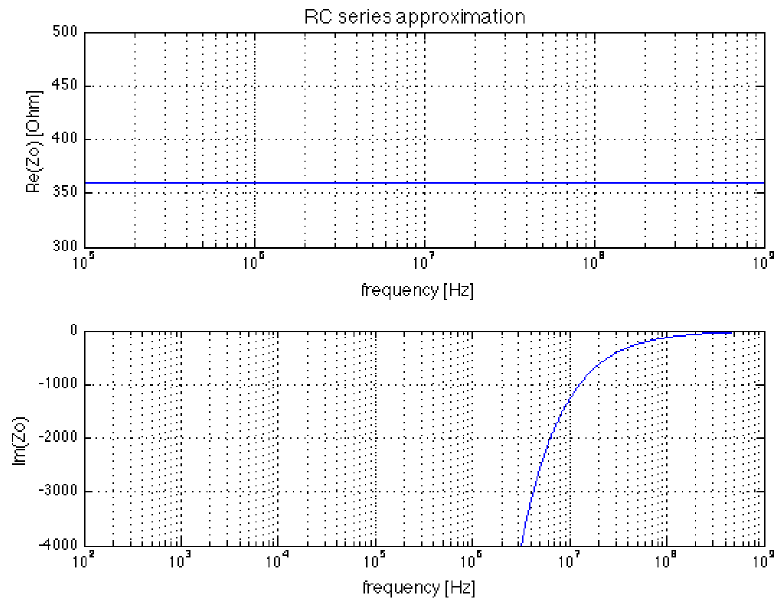

Figure 4.19: Characteristic impedance in function of frequency: real part (above) and immaginary part (below)

$$C = \frac{2\pi\epsilon_0}{ln\frac{b}{a}} = 9.28 \cdot 10^{-12} F/m \tag{4.15}$$

$$L = \frac{\mu_0}{2\pi} ln\frac{b}{a} = 1.19 \cdot 10^{-6} H/m \tag{4.16}$$

The resistance per unity of length of the anode wire can be computed by measuring the wire resistance and dividing for its length,

$$R = \frac{330}{1.92}\frac{\Omega}{m} \simeq 170\frac{\Omega}{m} \tag{4.17}$$

The conductance G is influential for our study so we can assume G=0, the characteristic impedance becomes:

$$Z_0 = \sqrt{\frac{R + j\omega L}{j\omega C}} \tag{4.18}$$

that is a complex function depending on frequency, the real part and the imaginary part correspond to the resistance and the reactance; they have been plotted in the graph 4.19. By the graph we can note that for $f > 100\ MHz$ the characteristic impedance

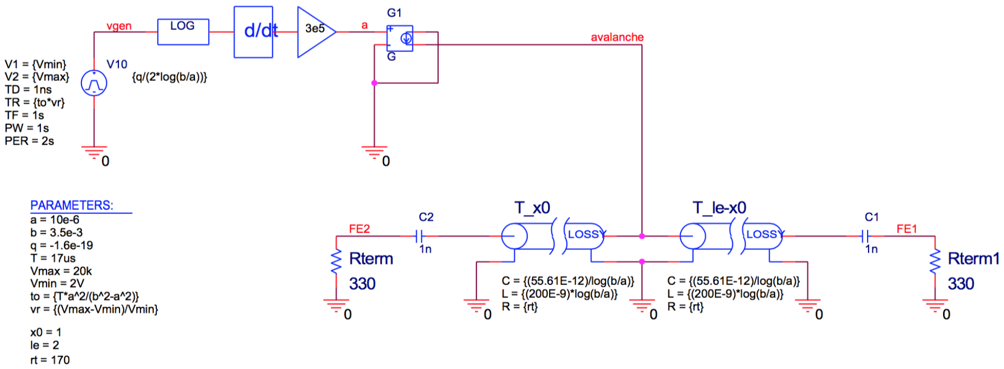

Figure 4.20: Drift cell modelling by means of trasmission line in PSpice enviroment

imaginary part tend to zero, so it can be approximated with a simple resistor of 330 Ω that will be the termination resistance at the FE input.

The signal reflection has been evaluated by PSpice Simulator (see figure 4.20). The avalanche signal generated at the wire input and the signal at the FE input are plotted in the graph 4.21. A reflection of less that 10% is obtained with this kind of input matching network.

Finally the reflections have been minimized empirically with different values of termination resistors in relation to the reflected signal visualized on the oscilloscope and the best resistor value is 330 Ω as reported in figure 4.22.

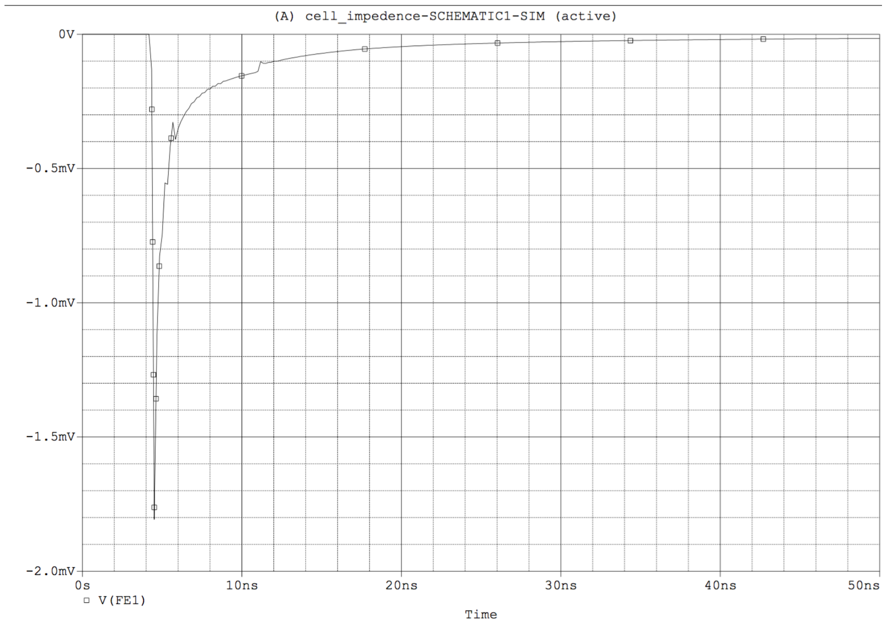

Figure 4.21: Signal reflection at FE input with a 330 Ω resistor value

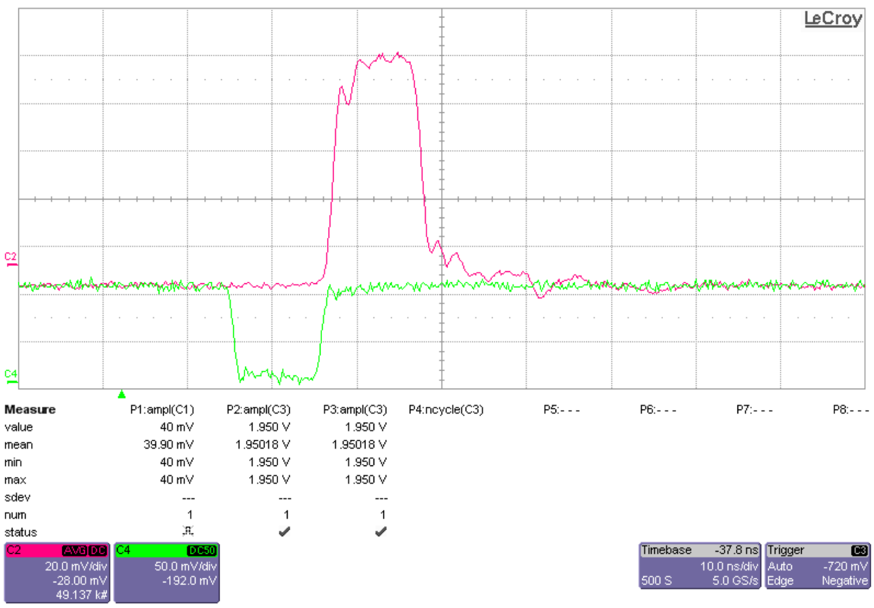

Figure 4.22: Signal pulse reflection on a drift cell with a 330 Ω terminated resistor

5

Impact parameter estimate using Cluster Timing techniques

In this chapter the momentum resolution and spatial resolution in MEG II DC are discussed, in order to introduce Cluster Counting/Timing motivations and methods. Two algorithms will be presented with the aim to improve the impact parameter estimate in the single hit resolution. The algorithms have been tested on Monte Carlo (MC) data drift distances showing a good improvement in the bias correction. The clusters identification is also discussed, in order to apply these algorithms on simulated waveforms processed by the electronics. In this perspective, we show how the electronics features, explained in the previous chapter, are crucial requirements to apply this techniques allowing to improve the spatial resolution in the chamber.

5.1 Momentum resolution and spatial resolution

By the theory we know that the trajectory of a charge particle in a magnetic field is obtained by measuring a set of points along the particle path. In presence of a constant magnetic field $\bar{B}$, a particle with a charge ze moves along a helix, with radius of curvature ρ in the transverse plane. The momentum of the particle can be obtained in cylindrical coordinates (ρ, ϕ, ϑ) from:

$$p = \frac{p_T}{sin\theta} = \frac{0.3zB\rho}{sin\theta} \tag{5.1}$$

where θ is the polar angle between the particle direction and the magnetic field axis and p_T is the component of the particle momentum in a plane transverse to the magnetic field. Notice that using B expressed in Tesla and ρ in meter, the value of p is in GeV/c. The momentum resolution can be decomposed in the transverse momentum resolution and longitudinal resolution on θ angle :

$$\left(\frac{\sigma_p}{p}\right)^2 = \left(\frac{\sigma_{p_T}}{p_T}\right)^2 + \left(\frac{\sigma_\theta}{tg\theta}\right)^2 \tag{5.2}$$

The resolution on transverse plane gets contribution from the error on track measurement and the error due to Multiple Scattering (62):

$$\left(\frac{\sigma_{p_T}}{p_T}\right)^2 = \left(\frac{p_T\sigma_{\rho\phi}}{0.3zBl}\sqrt{\frac{720}{N+4}}\right)^2 + \left(\frac{0.037}{\beta pBl}\sqrt{\frac{L}{X_0}}\right)^2 \tag{5.3}$$

where $\sigma_{\rho\phi}$ is the spatial resolution of the detector in the transverse plane, N is the number of points, uniformly spaced along the track, L is the track length and l is the radial size of the tracker. Also the resolution on θ angle has the contribution from the error on track measurement and Multiple Scattering:

$$(\sigma_\theta)^2 = \left(\frac{\sigma_z}{l\sqrt{N}}\frac{tg^2\theta}{1+tg^2\theta}\right)^2 + \left(\frac{13.6MeV/c}{\beta cp}z\sqrt{\frac{L}{X_0}}\left(1+0.038ln\frac{L}{X_0}\right)\right)^2 \tag{5.4}$$

where σ_z is the longitudinal resolution and X_0 the radiation length.

Equations 5.3 5.4 show that the choice of Helium based gas mixture thanks to its radiation length allows to minimize the Multiple Scattering contribution in momentum resolution.

It is clear that in order to obtain a good momentum resolution it is necessary to have good precision on the spatial measurement in the transverse plane and the resolution in z direction. The spatial resolution in the transverse plane depends on :

- the intrinsic fluctuations of the ionization process;
- the diffusion;
- electronics system.

The spatial resolution in transverse plane is given by the squaring sum of these three terms:

$$\sigma_{\rho\phi}^2 = \sigma_{ion}^2 + \sigma_{diff}^2 + \sigma_{electronics}^2 \tag{5.5}$$

The fluctuations in the spatial distribution of the primary ionization along the track and in the number of secondary electrons produced implicates an uncertainty on the

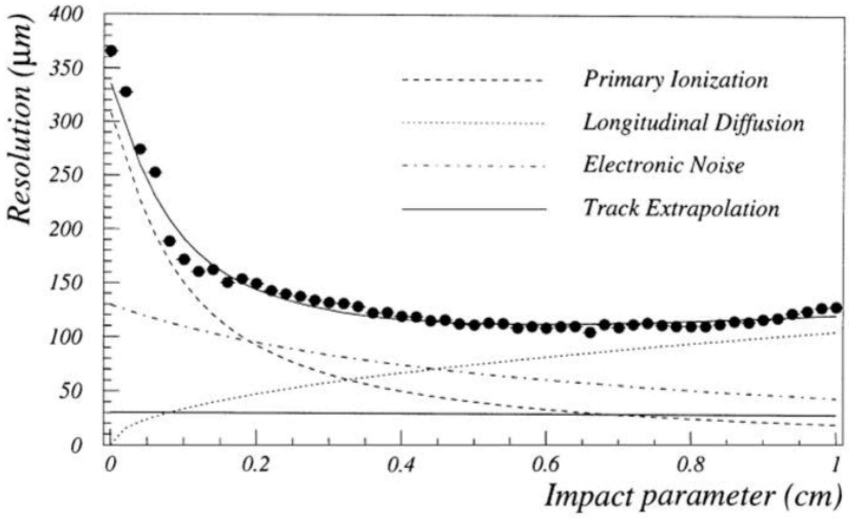

Figure 5.1: Single hit spatial resolution in KLOE drift chamber

position measurement. The contribution of the diffusion on the transverse plane is given by the longitudinal diffusion σ_L of the single electron. The third term is due to a systematic error depending on the resolution of the trigger system and electronics.

5.2 Cluster Timing motivations

The uncertainty on single hit resolution is the starting point to evaluate the DC spatial resolution. Figure 5.1 shows the spatial resolution of the KLOE experiment (44) on the single hit as a function of the impact parameter. As explained, spatial resolution gets contribution from many different sources: electronic noise, extrapolation uncertainty, electrons longitudinal diffusion, primary electrons ionization. Both the electronic noise and the ionization statistics, that are the more important contributions, can be reduced by using a fast electronic chain and the Cluster Timing techniques. A preliminary single hit reconstruction finds the Distance of Closest Approach (DCA) to the wire, from the arrival time of the first avalanche cluster, with a resolution of about 110 μm (49), (48).

In the track reconstruction phase, the coordinates of the first cluster not necessarily correspond to the point of closest approach to the anode wire (see figure 5.2). This phenomenon leads to an overestimate of the impact parameter particularly for short impact parameters and small cell drift chambers. The effect is more relevant, in high

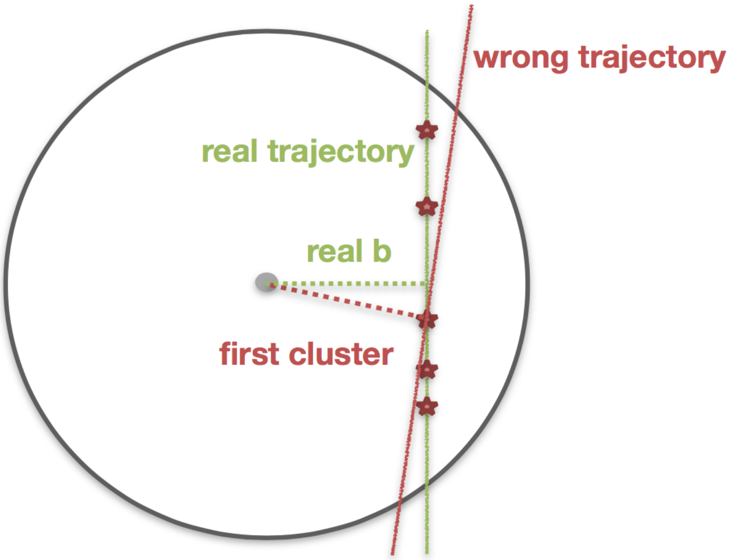

Figure 5.2: Impact parameter overestimate

transparent tracker, like the MEG II DC, in which the light helium based gas mixtures produces a low ionization clusters density (12.5 clusters/cm in a 90:10 Helium:Isobutane mixture). As regards the longitudinal resolution, the stereo angle structure allows to determine the position along the z axis simply by combining the informations of the adjacent layers. The resolution in z direction is obtained as the ratio of the resolution in transverse plane and the sin of the stereo angle δ:

$$\sigma_z = \frac{\sigma_{\rho\phi}}{sin\delta} \tag{5.6}$$

Therefore the precision in the position along z axis is improved by a better resolution in transverse plane and a large stereo angle. A large stereo angle makes the geometry more complicated in the pattern recognition strategy, besides it is hard to be realized.

The basic idea of Cluster Timing is to exploit the informations from the different clusters on the sense wire from the fast Front End electronics and use this information to provide an estimate of impact parameter. More specifically, Cluster Counting/Timing technique (28) consists in measuring the arrival times on the wires of each individual ionization cluster and combining these times to minimize the bias contribution to the impact parameter estimate. Apply Cluster Timing algorithms could be an important upgraded element of the MEG II tracker; in particular recognizing the clusters time distribution is very useful and can be used for:

- particle identification, by simply calculating the linear cluster density along an ionizing track;

- improvement of spatial resolution within a drift cell, by including the additional information coming from the arrival time of all the clusters after the first one;

- definition of the time of the event (trigger time), by looking at the synchronous arrival time of the latest cluster in all the cells hit

Since the high ionization potential of Helium (24.5 eV compared to the 15.7 eV of argon) causes small primary ionization density, the time separation between consecutive clusters goes from a few to a few tens of nanoseconds making Cluster Counting possible. Obviously a fast electronics and DAQ system are required to record and identify more clusters information and apply Cluster Timing techniques in order to reduce the bias on the impact parameter. A better determination of the impact parameter results in a better determination of the track parameters and thus momentum.

5.3 Impact parameter estimate

The first cluster information used as the conventional method of estimating the DCA is intuitive and computational safe, but it presents a bias that results in a systematic overestimation. The problem of finding an estimator of the impact parameter can be solved with two different approaches that will be illustrated following.
The first approach (29), (63), called $\frac{\lambda}{2}$, adopts an iterative algorithm based on simple geometrical considerations, that presume knowing λ.
Another way to estimate impact parameter is represented by the algorithm Maximum Product of Spacings (MPS), which provides the optimal estimator (30). The two algorithms will be compared in order to evaluate their performance and applicability.

5.3.1 $\frac{\lambda}{2}$ algorithm

$\lambda/2$ algorithm approach is to use the information provided by all the clusters to form a weighted average of the impact parameter estimates provided by the different clusters. The following hypothesis are done:

- ionized electrons and ions move on equidrift lines;

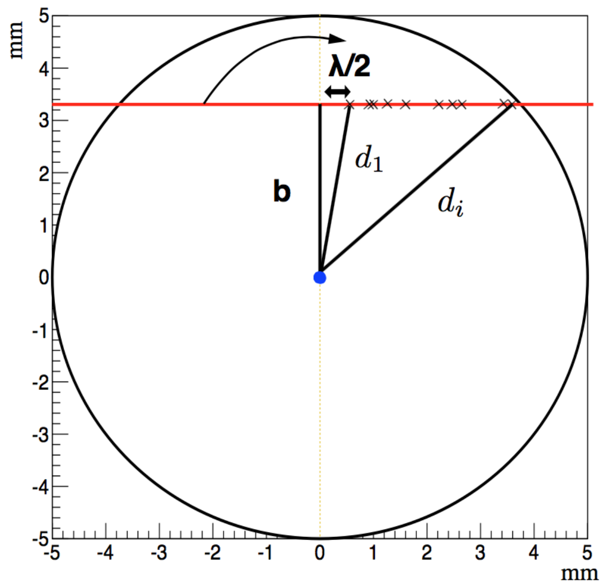

Figure 5.3: Drift tube single hit $\lambda/2$ approach: clusters are moved to one side resulting in a average distance between clusters equal to $\lambda/2$

- the mean free path λ is known by the statics;
- hits positions are ideally reported in one cell side;
- since the clusters have been moved in one side of the cell, the distance between two consecutive clusters equal to $\lambda/2$.
- clusters positions λ_i along the ionizing particle trajectory are obtained iteratively according to the assumption that the clusters are separated by $\lambda/2$.

Different values of impact parameter are calculate by using the Pythagoras theorem, and finally a weighted average gives an estimate of b. Figure 5.3 represents a single hit study with $\lambda/2$ algorithm approach. The algorithm is iterative and starts by the second cluster; following it is described step by step. By knowledge of first cluster we know that:

$$\lambda_1^2 = d_1^2 - b^2 \tag{5.7}$$

The second cluster is separated by the first one of $\lambda/2$ according with the algorithm hypothesis and similarly the position of the second cluster is given by:

$$\lambda_2^2 = \left(\lambda_1 + \frac{\lambda}{2}\right)^2 \tag{5.8}$$

Solving the equation 5.8 we can set the position of the first cluster at the second iteration:

$$\lambda_1^{(2)} = \frac{d_2^2 - d_1^2}{\lambda} - \frac{\lambda}{4} \tag{5.9}$$

$$b_{(2)}^2 = d_2^2 - \lambda_2^2 = \frac{d_2^2 + d_1^2}{2} - \frac{(d_2^2 - d_1^2)^2}{\lambda^2} - \frac{\lambda^2}{16} \tag{5.10}$$

Extending the algorithm steps at every iteration:

$$\lambda_1^{(i)} = \frac{d_i^2 - d_1^2}{(i-1)\lambda} - (i-1)\frac{\lambda}{4} \tag{5.11}$$

$$\lambda_i = \lambda_1^{(i)} + (i-1)\frac{\lambda}{2} \tag{5.12}$$

$$b_i^2 = d_i^2 - \lambda_i^2 = \frac{d_i^2 + d_1^2}{2} - \frac{(d_i^2 - d_1^2)^2}{(i-1)^2\lambda^2} - (i-1)^2\frac{\lambda^2}{16} \tag{5.13}$$

Each b derived by each cluster has its uncertainty that is used as weight for the average. The uncertainty associated to the b_i is

$$\sigma_i(b_i) = \sqrt{\left(\frac{\partial}{\partial \lambda_i} b_i\right)^2 \cdot \sigma_i^2(\lambda_i) + \left(\frac{\partial}{\partial d_i} b_i\right)^2 \cdot \sigma_i^2(d_i)} \tag{5.14}$$

where

$\sigma_i(\lambda_i) = -\frac{2\lambda_1^{(i)}}{\lambda} \cdot \sigma\left(\frac{\lambda}{2}\right)$

$\sigma_i(d_i) = 160\mu m \cdot \sqrt{d_i(cm)}$

$\sigma\left(\frac{\lambda}{2}\right) = \sqrt{\left(\frac{\lambda}{2}\right)^3}$

The impact parameter estimate is calculated by means of an weighted average:

$$b = \frac{\sum_{j=2}^{i} \frac{b_j}{\sigma_j^2(b_j)}}{\sum_{j=2}^{i} \frac{1}{\sigma_j^2(b_j)}} \tag{5.15}$$

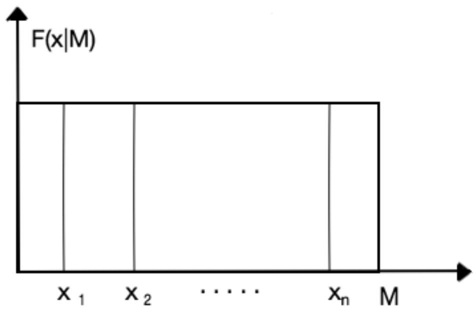

Figure 5.4: Flat distribution made of n observables x_1 ... x_N, where $x_0 = 0$, $x_1 < x_2 <$ ... $< x_N$, $x_{N+1} = M$

5.3.2 Maximum Product of Spacings algorithm

MPS algorithm (30) idea is to attribute the problem of using clusters information to the problem of estimating the upper limit of a flat distribution (between 0 and M) by making N measures $\{x_1 ... x_N\}$ (see figure 5.4). It is demonstrated (63), (30), (64), (65) that the maximum likelihood (ML) estimator in this case $x_{ML} = x_{max} = max_N(x_i)$ is pathological since the limits of the distribution depend on a parameter. Thus, a different approach based on (64), (65) has been proposed.
We know that the clusters are distributed uniformly (randomly) along the track and the separation between two consecutive clusters follows an exponential distribution with mean value λ. Thus we can assume that the relative spacing $D_i = x_i - x_{i-1}$ should be as similar as possible. Suppose $x_1 ... x_N$ observations representing cluster positions along the track, coming from a uniform distribution with an unknown end points. Assume $x_0 = 0$ and $x_{N+1} = M$. The MPS estimator for the parameter M is the one that maximizes the geometrical mean of the spacings:

$$G = \left\{ \prod_{i=1}^{n+1} \frac{D_i}{M} \right\}^{\frac{1}{n+1}} \tag{5.16}$$

or alternatively its logarithm:

$$H = logG = \frac{1}{n+1} \left\{ logx_1 + \sum_{i=2}^{n} log(x_i - x_{i-1}) + log(M - x_n) - (n+1)logM \right\} \tag{5.17}$$

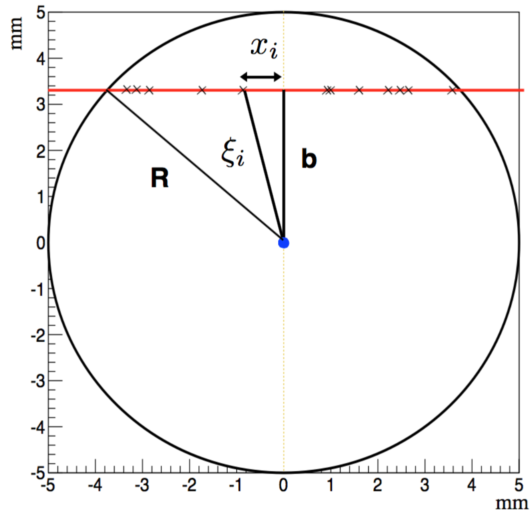

Figure 5.5: Drift Tube single hit MPS approach: clusters are generated along the track at x_i position

The maximum of the equation 5.17 is the MPS estimator of M:

$$M_{MPS} = x_{max} \frac{n+1}{n} \tag{5.18}$$

it is larger than x_{max} and their relative distance is just the average spacing between two consecutive x_i's. The MPS estimator has the same properties of ML estimator (30), or even better. It is asymptotically sufficient, consistent and asymptotically efficient. The result achieved for the flat distribution can be generalized to any distribution $f(x \mid M)$ using the cumulative *pdf*:

$$D_i = y_i - y_{i-1} = \int_{x_i-1}^{x_i} f(x \mid M) dx \tag{5.19}$$

In the next subsection we show that this method can be used to estimate the track-anode impact parameter.

5.3.2.1 Application to tracking

The statistical features developed above are used to estimate the track-anode point of closest approach b in a single drift cell in a 2-dimensional perspective. Suppose a particle is passing at distance b from an anode wire in a drift cell of radius R; the particle generates ionizations clusters randomly along its track 5.5. Let denote with x_i each generated cluster position along the track, the normalized probability density function (pdf) for each x_i, is given by:

$$F(x \mid b)dx = \frac{dx}{2\sqrt{R^2 - b^2}}\vartheta(-\sqrt{R^2 - b^2} < x < \sqrt{R^2 - b^2}) \tag{5.20}$$

where $\vartheta(a < x < b) = 1$ if $a < x < b$, 0 elsewhere. Let's indicate with $\{\xi_i\}$ the cluster distances from anode obtained by the time-drift relation. The normalized *pdf* for the ξ_i's is obtained by a change in variable:

$$G(\xi \mid b)d\xi = \frac{\xi d\xi}{\sqrt{R^2 - b^2}\sqrt{\xi^2 - b^2}}\vartheta(b < \xi < R) \tag{5.21}$$

The maximum likelihood estimator is ξ_{min}, value for which the likelihood diverges. Thus to obtain the MPS estimator we need to compute the D_i's from the cumulative distribution of:

$$y_i = \int_b^{\xi_i} \frac{\xi}{\sqrt{R^2 - b^2}\sqrt{\xi^2 - b^2}}\, d\xi = \frac{\sqrt{\xi_i^2 - b^2}}{\sqrt{R^2 - b^2}} \tag{5.22}$$

Using $\xi_0 = b$ and $\xi_{n+1} = R$. Hence:

$$D_i = y_i - y_{i-1} = \frac{\sqrt{\xi_i^2 - b^2} - \sqrt{\xi_{i-1}^2 - b^2}}{\sqrt{R^2 - b^2}} \tag{5.23}$$

We define the MPS estimator of the impact parameter, the b which maximizes the expression:

$$H(b) = \frac{1}{n+1}\sum_{i=1}^{n+1} log D_i \tag{5.24}$$

5.4 Algorithms tests on Monte Carlo distance

In order to test the algorithms described on the single hit measurement a Monte Carlo simulation has been performed. The detector considered in the simulation is made of eight drift tubes: the single drift tube radius is 0.5 cm, with an anode wire of 20 μm diameter. The data are generated according to the geometry, the gas mixture, the electric field configuration and the physic phenomenons that regulate the loss of energy

Table 5.1: MC data simulation setting parameters

Parameter	Setting
Number of simulate events	50000
Gas Gain	3×10^5
HV voltage	1500 V
Gas Mixture	90% He:10% iC_4H_{10}
anode radius	10 μm
tube radius	5 mm
ADC time resolution	0.5 ns

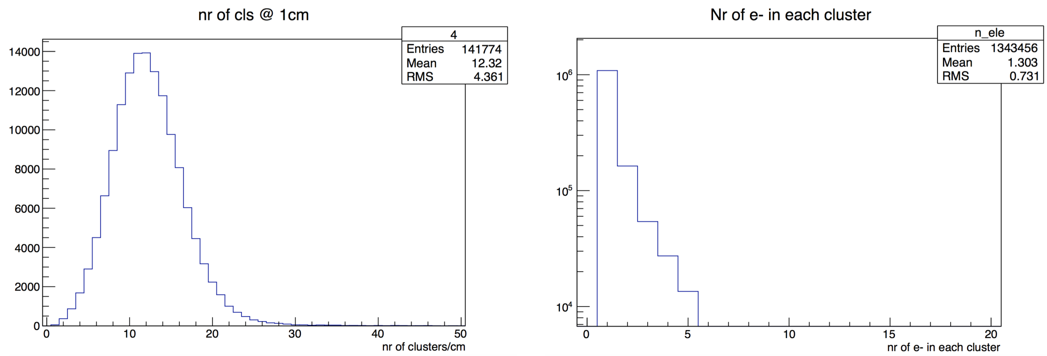

(a) (b)

Figure 5.6: a) Frequency of the number of cluster/cm generated by the ionizing particle; b) Number of electrons in one cluster

in the ionization process. Table 5.1 summarizes the main parameters of the MC data simulation.

We simulate the particle track in the drift tube, the cluster produced along its path, the number of electrons in each cluster, the distance of closest approach and drift distance from the anode (impact parameter).

Figure 5.6(a), shows the frequency of the number of clusters generated in MC data for track length of 1 cm and figure 5.6(b) exhibits the number of electrons in each cluster, that we call "multiplicity".

The different track lengths coming out by the ionizing particle are reported in figure 5.7(a) and the distribution of the impact parameter in each event is shown in figure 5.7(b).

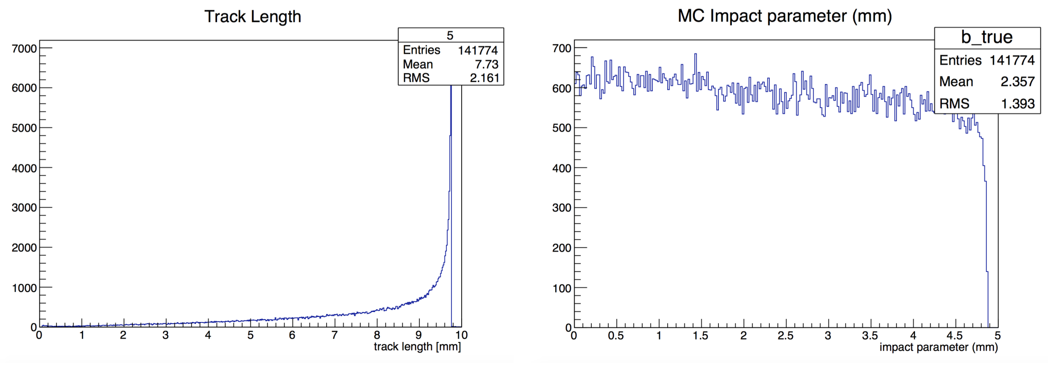

(a) (b)

Figure 5.7: a) Frequency of the track length generated by the ionizing particle; b) Impact parameter distribution

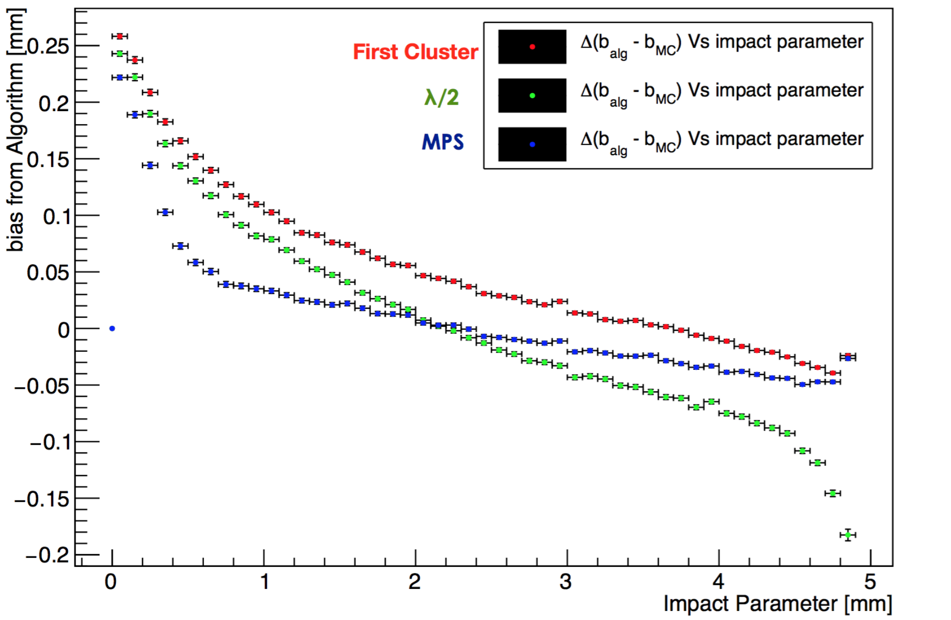

Figure 5.8: Difference between impact parameter estimation obtained from algorithms and impact parameter of MC data

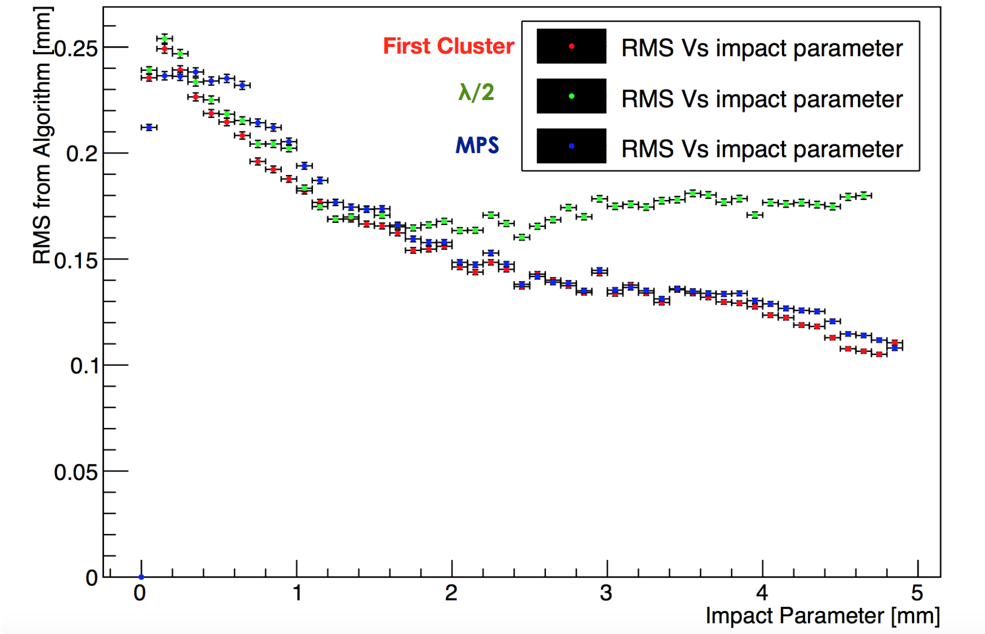

Figure 5.9: RMS for the three impact parameter estimation approaches as funcion of the impact parameter

The impact parameter of MC data, that we call b_{MC}, has been compared to the impact parameter estimate obtained from results of the algorithms presented above b_{alg}. The residuals $\Delta b = b_{alg} - b_{MC}$, for the three different methods, First Cluster, $\lambda/2$, MPS, have been plotted for the different impact parameter ranges. As we can see by the figure 5.8, the first cluster information provide an overestimate of the distance of closest approach, and this effect is more intense for short impact parameter as we foreseen. Applying the $\lambda/2$ algorithm this bias is reduced, but MPS estimator corrects well the bias up to 2.5 mm, maintaining quite stable for long distance.

By computing the RMS in the three algorithm, we obtained the uncertainties on the impact parameter (see figure 5.9) similar with those showed in the single hit resolution measurements. Each point in the graph is obtained projecting the $b_{alg} - b_{MC}$ distribution bin per bin. Although, the bins corresponding to large impact parameter present a Gaussian shape distribution as it is visible by the figure 5.10, in the first bin the distribution can non be considered Gaussian (see figure 5.11) due to the presence of the tails; thus we can not extract the resolution of the algorithm but we can only evaluate the Root Mean Square.

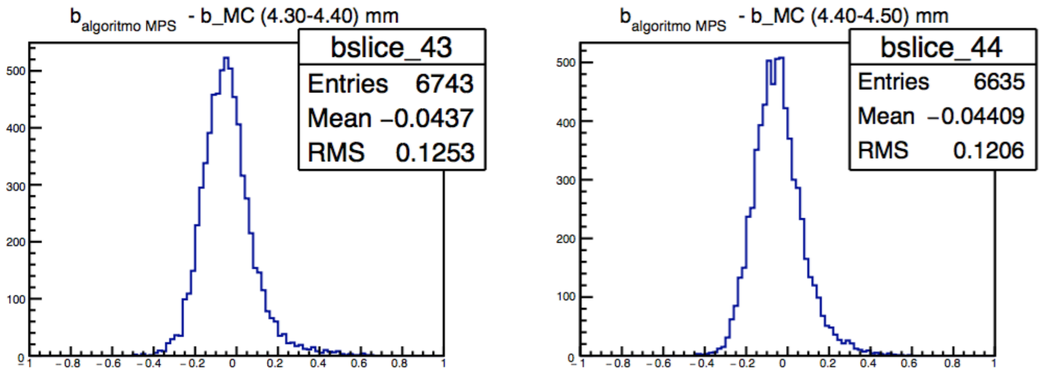

Figure 5.10: RMS distribution of $b_{alg} - b_{MC}$ in the last two bin

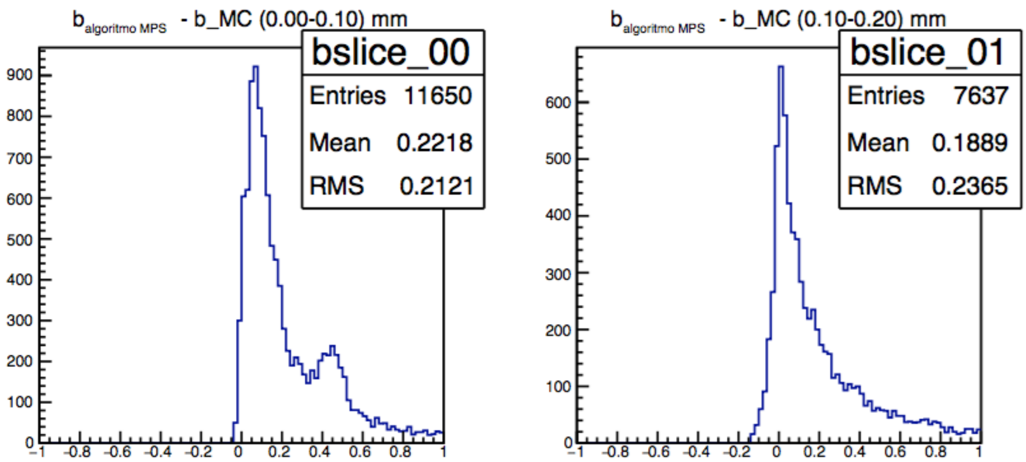

Figure 5.11: RMS distribution of $b_{alg} - b_{MC}$ in the first two bin

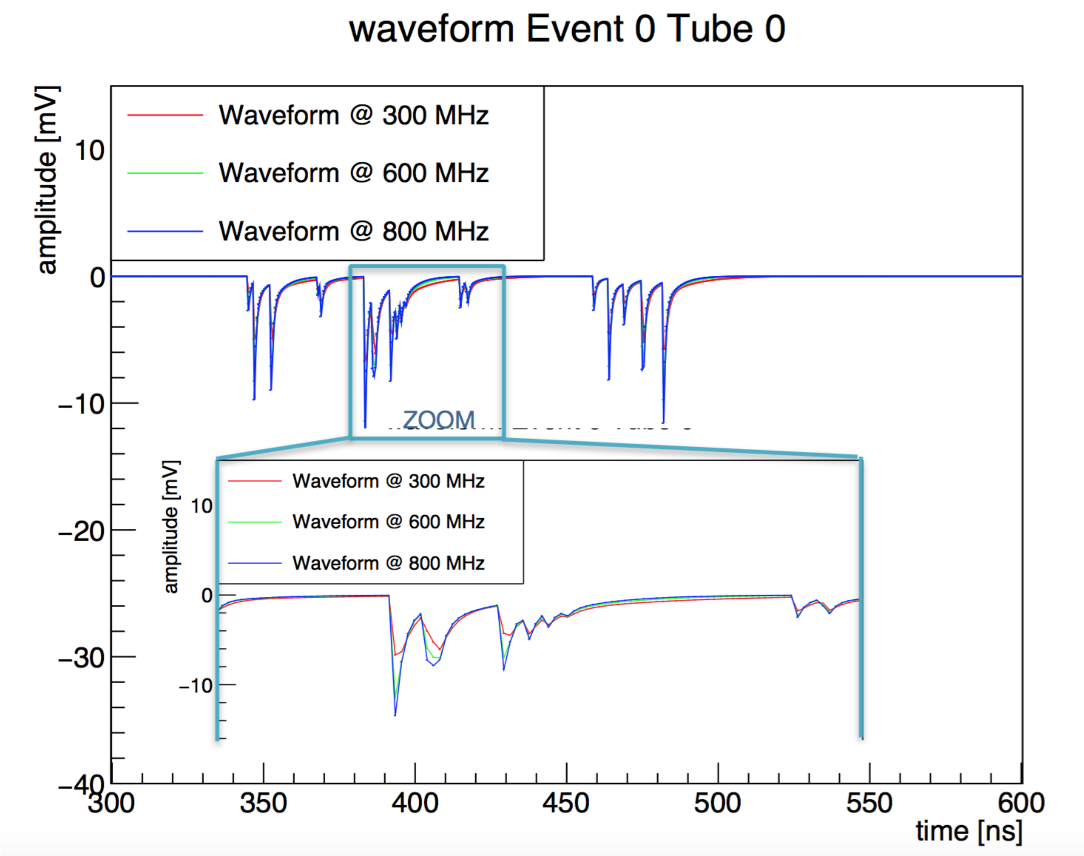

Figure 5.12: Monte Carlo waveform generation at different bandwidth system

5.5 Waveform Generation

In order to evaluate the algorithms described above on DC signals, we have to analyse the waveforms recorded by the detector system: in particular a peak recognition strategy is necessary in order to identify structures related to the ionization acts.

The readout signal induced by the detector and processed by the electronics has been simulated by means of PSpice Simulator according with the procedure described in 4.3.1. The single electron pulse shape, obtained by the PSpice simulation, has been fitted with an empirical function depending on the following parameters V_0, t_0, τ_{D1}, τ_{UP}, τ_{D2}:

$$a(t) = \frac{V_0}{k}\frac{\tau_{D1}+\tau_{UP}}{\tau_{UP}+\tau_{D2}}(1-e^{-(t-t_0)/\tau_{UP}})\left[\frac{R}{\tau_{D1}}e^{-(t-t_0)/\tau_{D1}} + \frac{1-R}{\tau_{D2}}e^{-(t-t_0)/\tau_{D2}}\right] \quad (5.25)$$

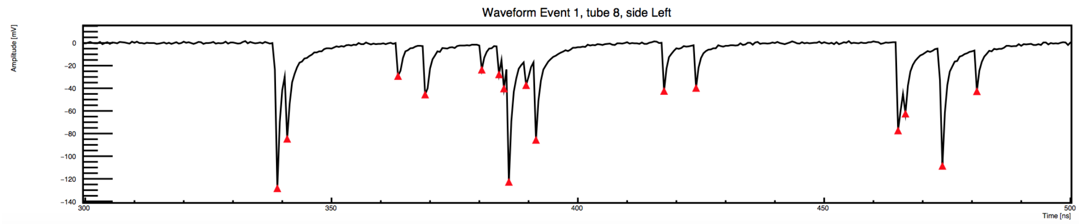

Figure 5.13: Peaks found by the algorithm in a typical waveform generate by the MC simulation

where $k = \tau_{D1}R + \tau_{UP}R + \tau_{D1}\tau_{UP}R + \tau_{UP}R\tau_{D2}$ is a normalizing constant.
The waveforms at different bandwidths have been generated on varying the parameters R, τ_{UP}, τ_{D1}, τ_{D2}. Based on the sequence of the time arrival of the electrons, the waveforms have been produced as overlapping of the N electrons generated in the MC event, each located in correspondence of the arrival time of the electrons. A picture of a typical event waveform as result of electronics system at different bandwidths, without noise addition, is shown in figure 5.12. By the graph is obvious to see that pulses processed with a lower bandwidth system have a slow rise time and this fact can be penalizing in the peak find strategy; moreover they have major chance to be hidden by the noise due to their small height.

5.6 Peak Find Algorithm

In this section we describe the procedure to find and localize the peaks on the simulated waveforms at different electronics bandwidths in order to make a comparison of the algorithm efficiency as a function of the bandwidth system and noise level. The Peak Find algorithm identifies, in the digitized signal, the peaks corresponding to the different ionization electrons and stores each peak amplitude and timing in a memory. The algorithm approach is derivative, first and second derivative are calculated and their value is compared to a threshold related to the signal noise level. Simultaneously a smoothing of the signal is done. The determination of a peak is done by relating the $n-th$ sample to a number n of preceding samples, where n is directly proportional to the rise times of the signal peak.

Figure 5.13 shows a typical waveform with the addition on Gaussian noise, the Peak Find algorithm applied to this waveform recognizes the peaks highlighted with the red

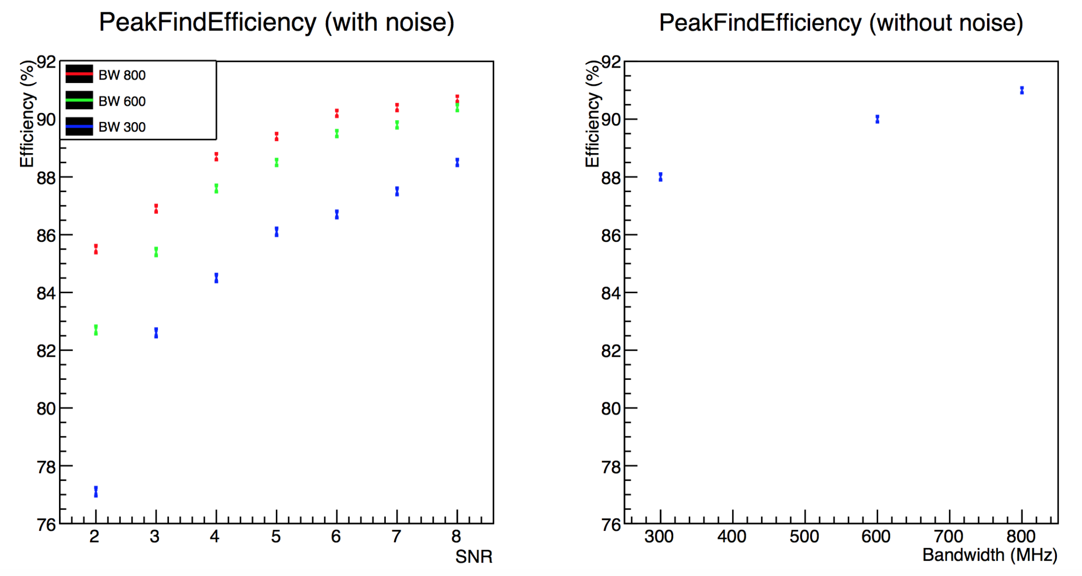

Figure 5.14: PeakFind algorithm efficiency as function of SNR (on the left) for the different bandwidth; PeakFind algorithm efficiency as function of bandwidth (on the right) in absence of noise

marker.

This algorithm processes the data off-line but can be also implemented in real time on programmable device such as Field Programmable Gate Array (27), (41).

The algorithm has been run on the MC waveform and its efficiency has been evaluated. The efficiency is defined as the ratio between the recognizing peaks and the MC peaks corresponding to the drifting electrons:

$$eff = \frac{n^{\circ}recognpeaks}{n^{\circ}MCpeaks} \tag{5.26}$$

At first the Peak Find Algorithm was run on the waveform without noise, monitoring the efficiency as function of the bandwidth (graph on the right in figure 5.14). The algorithm recognizes peaks quite with the same efficiency in the ideal condition, stabling in a range between 88% and 92%.

Progressively a Gaussian white noise has been added and the efficiency as function of the Signal to Noise Ratio (SNR) has been evaluated for the different bandwidth. It is interesting to note that efficiency is considerably reduced for small SNR value at 300 MHz bandwidth and it is close to the intrinsic efficiency for high SNR also for lower bandwidth. This underline how it is important to keep under control the noise and how, when it can not be further reduced, a wide bandwidth allow to maintain the peak find efficiency to acceptable values.

The next step consisted in get together electrons belonging to same cluster in order to recognize every ionization cluster and apply algorithms above described for impact parameter estimation.

5.7 Cluster Recognition strategy

The measurement of the number of the clusters and consequently the clusters identification, consists of recognizing in the signal the structures that are generated during the coming of the electrons of a cluster on the anode. First of all, we have to ensure that pulse due to different clusters have a low probability to overlap, allowing to be identified. Secondly, the time distance between pulses generated by electrons coming from the same cluster must be small with respect to the time between two consecutive cluster in order to prevent over counting. In this perspective two factors related to the issues explained are relevant: time resolution and diffusion.

5.7.1 Time Resolution

Essentially, the time resolution is the results of the resolution of the detector combined to entire electronic system and the signal processing. The effects are manly due to the dead time of the detector and the electronics. The basic features of the electronics are:

- the rise time of the pre-amplifier;

- the sampling rate.

Obviously a short rise time is indispensable to follow the fast signal variations and allow to distinguish the finest structures; moreover it permits a more precise temporal location of the pulses related to a single cluster. This is the reason of the fast electronic FE designed for MEG II tracker. The sampling rate, imposed by the Analog to Digital Converter, defines the system resolution because it fixes the minimum time distance between two observable peaks. Also this aspect has been improved with the new WAVEDREAM board (47). The effect of a resolution $\Delta t \neq 0$ is that we can not solve and thus count, those peaks related to the same cluster with a time separation

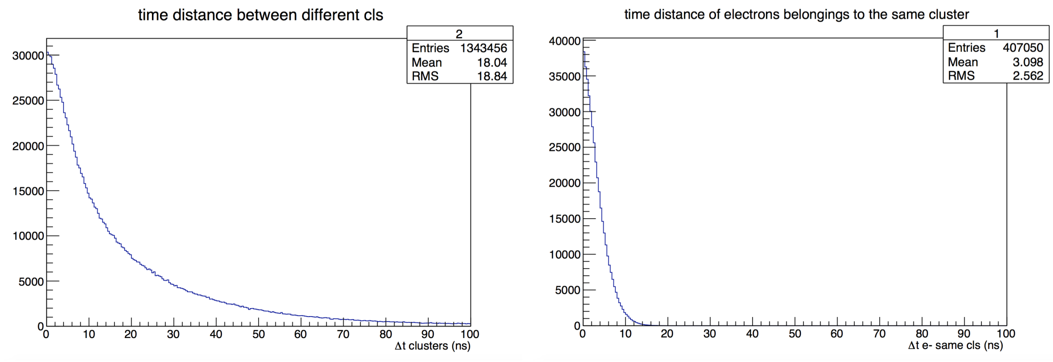

(a) (b)

Figure 5.15: a) Temporal distance of different clusters; b) Time spacing of electrons belonging to the same cluster

less than Δt. Thus, the time resolution brings a counting underestimate because it is not possible distinguish two structures that fall in the same temporal bin.

5.7.2 Diffusion

The multiple collisions generated in the gas in the passage of the ionizing particle make the electrons spread in the time. The electrons spatial distribution follows a Gaussian distribution with a standard deviation variable in the time (55):

$$\frac{dN}{dx} = \frac{N}{\sqrt{4\pi Dt}} e^{-\frac{x^2}{4Dt}} \tag{5.27}$$

The standard deviation at a time t is: $\sigma = \sqrt{2Dt}$ where D is the diffusion coefficient that describes the diffusion properties of the particle in the gas mixture. The effect of the diffusion is a smearing of the arrival times of the electrons originated in the same position as it is possible to see in figure 5.15(b), where the time spacing of electrons in the same cluster is depicted, while in the figure 5.15(a), we find the temporal distance of all the clusters. It is clear that the diffusion phenomena can yield a over counting in cluster recognition strategy.

5.8 Cluster Counting

In the ideal condition, with a time resolution $\Delta t = 0$ and in absence of diffusion, the electrons of the same cluster reach the anode in the same time, generating a single pulse

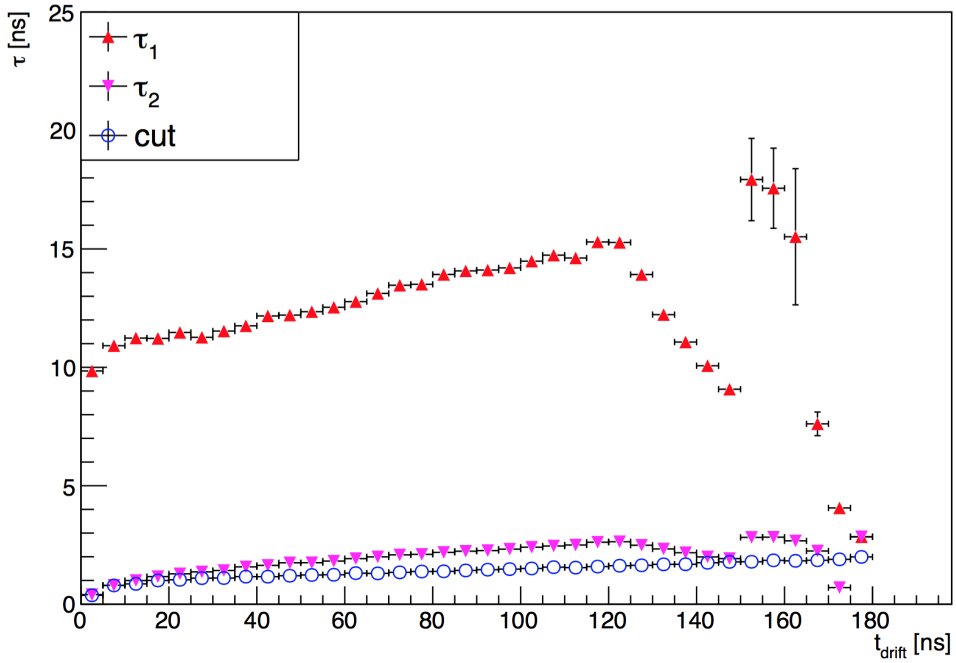

Figure 5.16: Time separation of electrons in different clusters (τ_1) and time separation of electrons belonging to the same cluster (τ_2) as function of drift time. The blue points represent the temporal threshold set in order to obtain the mean number of counted clusters equal to the mean number of MC clusters

(without structures) at different amplitudes depending on the number of electrons. In practice, the effect of time resolution contributes to an inefficiency in counting while the effect of the diffusion leads to an overcounting. Obviously the effect of the separation of the electrons belonging to the same cluster due to the diffusion, results more evident the for long drift times and thus for large impact parameters.

In general we can assume that electrons with a time distance below a certain value, that we call "time cut", comparable to the diffusion effect, are originated in the same cluster. However, as we have seen, because the spread in time depends on the drift time, we have to take into account this fact when we get together electrons to define a cluster. The basic idea is to build different time cuts as function of drift time and apply these cuts on the different drift distances in order to compensate the effects of time resolution and diffusion.

Starting from figure 5.15(b) we considered the distribution of time distance between consecutive electrons as function of drift time, in slice of 5 ns each. The distributions for each drift time slice have been fitted with a double exponential function. The two time constants, obtained by the fit function, are used to extrapolate the points on the graph in figure 5.16. Points indicated as τ_1 represent the difference in time between electrons of different clusters, while τ_2 correspond to the time spread of electrons belonging to the same cluster. The blue points are defined as the time value for which the mean number of counted clusters is equal to the mean number of MC cluster in each slice. This values are used to set the temporal threshold in order to count clusters in the different temporal slices.

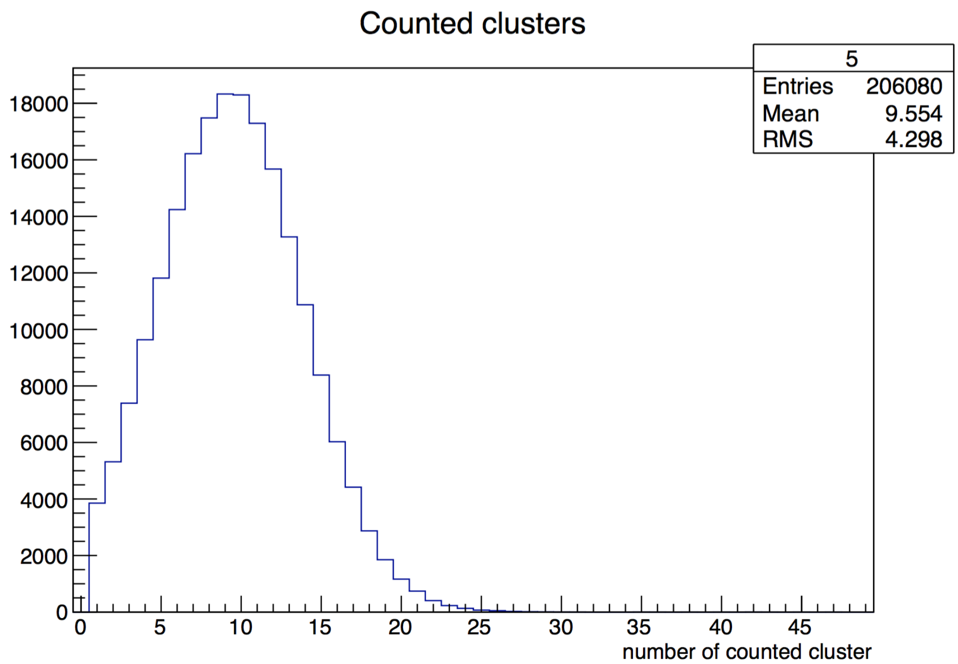

Figure 5.17: Number of counted cluster

The distribution of the counted cluster is reported in figure 5.17, while in figure 5.18, we can observe the residuals between the number of the clusters generated in MC simulation and the counted cluster. The distribution follows a Gaussian shape, by the fit parameters we can say that it is possible to count the right number of cluster on average with an uncertainty of 1.6 cluster. Obviously, this value can be further improved, but it can be considered a good starting point for cluster identification strategy. At the later time, a timing assignment in each cluster recognized is necessary in order to apply algorithm on the waveforms. The time of the cluster can be assigned

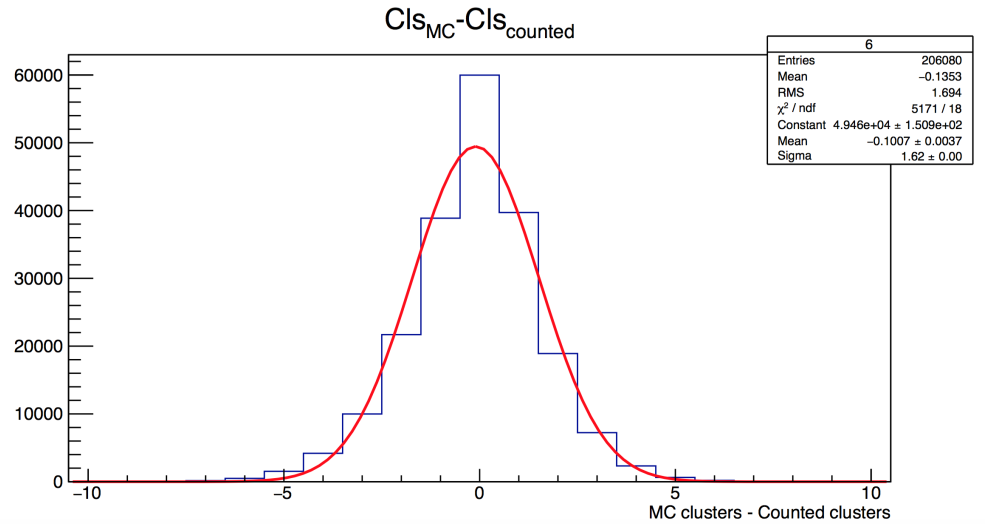

Figure 5.18: Difference between number of MC clusters and counted clusters

by making a weighted average of the time of the electrons in each cluster. As it has been done for Cluster Counting in cluster recognition strategy, MC simulations can be used to optimize the results.

Conclusions

The Lepton Flavour Violation is considered a powerful probe for testing physics beyond the standard Model. Different experiments designed to measure forbidden processes are operative producing data to be analyzed. With the last data analysis, the MEG experiment established a new upper limit equal to 4.2×10^{-13} at 90% C.L. in 2016. An upgrade of the experiment in order to improve the sensitivity of one order of magnitude was approved and it is actually under development. New detectors with better performances are under construction. A new high transparency and high granularity tracker, based on a unique volume multi-wire drift chamber is under construction at INFN section of Pisa and Lecce. In this thesis we described the MEG II tracker and we studied the drift chamber signal generation that provides the features required to the Front End electronics for the first signal acquisition and elaboration. We have seen that a wide bandwidth, low noise electronics is necessary in order to follow the fast variations of the signal and preserve its shape. For this purpose a multi-channel analog board, based on commercial devices has been designed and realized at INFN of Lecce laboratory. Test on the last prototypes shows that it is possible to keep a high bandwidth near 1 GHz, also after 5 meters long cable. This electronics is the prerequisite for the applicability of Cluster Counting/Timing techniques that can improve further the spatial resolution of the detector in the upgrade phase. The Clu Cou/Tim algorithms tested on Monte Carlo data showed a good improvement on the impact parameter estimation in the single hit measurement, that can bring important improvements on spatial resolution and thus momentum resolution in the chamber.

Bibliography

[1] Francis Halzen and Alan D Martin. *Quark & Leptons: An Introductory Course In Modern Particle Physics*. John Wiley & Sons, 2008. 3

[2] Michael Peskin and Dan Schroeder. An introduction to quantum field theory. 1995. 3

[3] IJR Aitchison and AJG Hey. Gauge theories in particle physics. *Adam Hilger*, 1984. 3

[4] Chris Quigg. *Gauge theories of the strong, weak, and electromagnetic interactions.* Princeton University Press, 2013. 3

[5] Francisco J Ynduráin. *The theory of quark and gluon interactions*. Springer Science & Business Media, 2007. 3

[6] Richard D Field. *Applications of perturbative QCD*. Addison-Wesley, 1989. 3

[7] Riccardo Barbieri, Lawrence Hall, and Alessandro Strumia. Violations of lepton flavour and cp in supersymmetric unified theories. *Nuclear Physics B*, 445(2):219–251, 1995. 4

[8] André de Gouvêa and Petr Vogel. Lepton flavor and number conservation, and physics beyond the standard model. *Progress in Particle and Nuclear Physics*, 71:75–92, 2013. 4

[9] Kalpana Bora and Gayatri Ghosh. Charged lepton flavor violation $\mu \to e\gamma$ in μ-τ symmetric susy so (10) msugra, nuhm, nugm, and nusm theories and lhc. *The European Physical Journal C*, 75(9):1–14, 2015. 4

[10] Sheldon Lee Glashow. Particle physics in the united states, a personal view. *arXiv preprint arXiv:1305.5482*, 2013. 4

[11] EP Hincks and B Pontecorvo. Search for gamma-radiation in the 2.2-microsecond meson decay process. *Physical Review*, 73(3):257, 1948. 5, 7, 9

[12] R. H. Bernstein and P. S. Cooper. Charged lepton flavor violation: An experimenter's guide. 532:27–64, November 2013. 7, 10

[13] William J Marciano, Toshinori Mori, and J Michael Roney. Charged lepton flavor violation experiments. *Annual Review of Nuclear and Particle Science*, 58(1):315, 2008. 7

[14] AM Baldini, F Cei, C Cerri, S Dussoni, L Galli, M Grassi, D Nicolo, F Raffaelli, F Sergiampietri, G Signorelli, et al. Meg upgrade proposal. *arXiv preprint arXiv:1301.7225*, 2013. 7, 18, 21, 23, 32, 36, 48

[15] Marcello Conversi, Ettore Pancini, and Oreste Piccioni. On the disintegration of negative mesons. *Physical Review*, 71(3):209, 1947. 7

[16] Enrico Fermi, Edward Teller, and Victor Weisskopf. The decay of negative mesotrons in matter. *Physical Review*, 71(5):314, 1947. 7

[17] MEG Collaboration et al. Search for the lepton flavour violating decay $\mu^+ \longrightarrow e^+\gamma$ with the full dataset of the meg experiment. *arXiv preprint arXiv:1605.05081*, 2016. 9, 16

[18] W Bertl, R Engfer, EA Hermes, G Kurz, T Kozlowski, J Kuth, G Otter, F Rosenbaum, NM Ryskulov, A Van Der Schaaf, et al. A search for mu2e conversion in muonic gold. *The European Physical Journal C-Particles and Fields*, 47(2):337–346, 2006. 9

[19] Robert K Kutschke. The mu2e experiment at fermilab. *arXiv preprint arXiv:1112.0242*, 2011. 9

[20] S Mihara. Prospects for clfv experiments. In *Journal of Physics: Conference Series*, volume 408, page 012017. IOP Publishing, 2013. 10

[21] U Bellgardt, G Otter, R Eichler, L Felawka, C Niebuhr, HK Walter, W Bertl, N Lordong, J Martino, S Egli, et al. Search for the decay μ+ e+ e+ e-. *Nuclear Physics B*, 299(1):1–6, 1988. 10

[22] J Adam, X Bai, A Baldini, E Baracchini, A Barchiesi, C Bemporad, G Boca, PW Cattaneo, G Cavoto, G Cecchet, et al. A limit for the $\mu \longrightarrow e\gamma$ decay from the meg experiment. *Nuclear Physics B*, 834(1):1–12, 2010. 16, 19

[23] J Adam, X Bai, AM Baldini, E Baracchini, C Bemporad, G Boca, PW Cattaneo, G Cavoto, F Cei, C Cerri, et al. New constraint on the existence of the $\mu^+ \longrightarrow e^+ \gamma$ decay. *Physical review letters*, 110(20):201801, 2013. 16

[24] J Adam, X Bai, AM Baldini, E Baracchini, C Bemporad, G Boca, PW Cattaneo, G Cavoto, F Cei, C Cerri, et al. New limit on the lepton-flavor-violating decay $\mu^+ \longrightarrow e^+ \gamma$. *Physical review letters*, 107(17):171801, 2011. 16

[25] AM Baldini, E Baracchini, L Berretta, S Bianucci, G Cavoto, G Chiarello, C Chiri, F Cei, A Corvaglia, S Dussoni, et al. A new cylindrical drift chamber for the meg ii experiment. *Nuclear Instruments and Methods in Physics Research Section A: Accelerators, Spectrometers, Detectors and Associated Equipment*, 2015. 19, 47

[26] G Chiarello, C Chiri, A Corvaglia, F Grancagnolo, A Miccoli, M Panareo, A Pepino, C Pinto, P Primiceri, M Spedicato, et al. A new construction technique of high granularity and high transparency drift chambers for modern high energy physics experiments. *Nuclear Instruments and Methods in Physics Research Section A: Accelerators, Spectrometers, Detectors and Associated Equipment*, 2015. 19, 47, 52, 53

[27] L Cappelli, P Creti, F Grancagnolo, A Pepino, and G Tassielli. A fast readout algorithm for cluster counting/timing drift chambers on a fpga board. *Nuclear Instruments and Methods in Physics Research Section A: Accelerators, Spectrometers, Detectors and Associated Equipment*, 718:226–228, 2013. 19, 46, 99

[28] GF Tassielli, F Grancagnolo, and S Spagnolo. Improving spatial resolution and particle identification. *Nuclear Instruments and Methods in Physics Research Section A: Accelerators, Spectrometers, Detectors and Associated Equipment*, 572(1):198–200, 2007. 19, 42, 86

[29] Michele Cascella, Francesco Grancagnolo, and Giovanni Tassielli. Cluster counting/timing techniques for drift chambers. In *Nuclear Science Symposium and Medical Imaging Conference (NSS/MIC), 2013 IEEE*, pages 1–4. IEEE, 2013. 19, 42, 87

[30] G Signorelli, M Venturini, et al. A novel method to estimate the impact parameter on a drift cell by using the information of single ionization clusters. *Nuclear Instruments and Methods in Physics Research Section A: Accelerators, Spectrometers, Detectors and Associated Equipment*, 824:581–583, 2016. 19, 87, 90, 91

[31] J Adam, X Bai, AM Baldini, E Baracchini, C Bemporad, G Boca, PW Cattaneo, G Cavoto, F Cei, C Cerri, et al. The meg detector for $\mu^+ \longrightarrow e^+\gamma$ decay search. *The European Physical Journal C*, 73(4):1–59, 2013. 30

[32] Ryu Sawada. Performance of liquid xenon gamma ray detector for meg. *Nuclear Instruments and Methods in Physics Research Section A: Accelerators, Spectrometers, Detectors and Associated Equipment*, 623(1):258–260, 2010. 31

[33] A Baldini, C Bemporad, F Cei, T Doke, M Grassi, AA Grebenuk, DN Grigoriev, T Haruyama, K Kasami, J Kikuchi, et al. Absorption of scintillation light in a 100l liquid xenon γ-ray detector and expected detector performance. *Nuclear Instruments and Methods in Physics Research Section A: Accelerators, Spectrometers, Detectors and Associated Equipment*, 545(3):753–764, 2005. 31

[34] T Iwamoto. The lxe calorimeter and the pixelated timing counter in the meg ii experiment. *Journal of Instrumentation*, 9(09):C09037, 2014. 32, 36

[35] M De Gerone, S Dussoni, K Fratini, F Gatti, R Valle, G Boca, PW Cattaneo, R Nardo, M Rossella, L Galli, et al. Development and commissioning of the timing counter for the meg experiment. *Nuclear Science, IEEE Transactions on*, 59(2):379–388, 2012. 35

[36] Malte Hildebrandt. The drift chamber system of the meg experiment. *Nuclear Instruments and Methods in Physics Research Section A: Accelerators, Spectrometers, Detectors and Associated Equipment*, 623(1):111–113, 2010. 37

[37] G Chiarello, C Chiri, A Corvaglia, A Innocente, F Grancagnolo, A Maffezzoli, P Mazzotta2 A Miccoli, M Panareo, A Pepino, P Primiceri, et al. The meg experiment at lecce. 40

[38] AM Baldini, E Baracchini, L Berretta, S Bianucci, G Cavoto, G Chiarello, C Chiri, F Cei, A Corvaglia, S Dussoni, et al. A new cylindrical drift chamber for the meg ii experiment. *Nuclear Instruments and Methods in Physics Research Section A: Accelerators, Spectrometers, Detectors and Associated Equipment*, 2015. 40

[39] G Chiarello, C Chiri, A Corvaglia, F Grancagnolo, A Miccoli, M Panareo, A Pepino, C Pinto, P Primiceri, M Spedicato, et al. A new assembly technique of full stereo drift chamber for high energy physics experiments. In *Advances in Sensors and Interfaces (IWASI), 2015 6th IEEE International Workshop on*, pages 68–71. IEEE, 2015. 40

[40] Michele Cascella, A Corvaglia, Francesco Grancagnolo, M Panareo, A Pepino, and Giovanni Tassielli. A full acquisition and elaboration system for drift chambers. In *Nuclear Science Symposium and Medical Imaging Conference (NSS/MIC), 2013 IEEE*, pages 1–4. IEEE, 2013. 40, 42

[41] Alessandro Corvaglia, Francesco Grancagnolo, Aurora Pepino, Patrizio Primiceri, Giovanni Tassielli, Marco Panareo, Michele Cascella, and Yuri Yudin. A readout electronics for drift chambers signals processing. In *Advances in Sensors and Interfaces (IWASI), 2013 5th IEEE International Workshop on*, pages 71–74. IEEE, 2013. 40, 42, 99

[42] G Chiarello, C Chiri, A Corvaglia, F Grancagnolo, M Panareo, A Pepino, C Pinto, and G Tassielli. A high performance front end electronics for drift chamber readout in meg experiment upgrade. *Nuclear Instruments and Methods in Physics Research Section A: Accelerators, Spectrometers, Detectors and Associated Equipment*, 2015. 40, 42, 51

[43] G Chiarello, C Chiri, A Corvaglia, F Grancagnolo, M Panareo, A Pepino, C Pinto, and G Tassielli. A high performance front end for meg ii tracker. In *Advances in Sensors and Interfaces (IWASI), 2015 6th IEEE International Workshop on*, pages 55–57. IEEE, 2015. 40, 51

[44] M Adinolfi, F Ambrosino, A Andryakov, A Antonelli, M Antonelli, C Bacci, R Baldini-Ferroli, A Bankamp, F Bellini, G Bencivenni, et al. The tracking detector of the kloe experiment. *Nuclear Instruments and Methods in Physics Research Section A: Accelerators, Spectrometers, Detectors and Associated Equipment*, 488(1):51–73, 2002. 40, 85

[45] G Cataldi, F Grancagnolo, and S Spagnolo. Cluster counting in helium based gas mixtures. *Nuclear Instruments and Methods in Physics Research Section A: Accelerators, Spectrometers, Detectors and Associated Equipment*, 386(2):458–469, 1997. 42

[46] Stefan Ritt, Roberto Dinapoli, and Ueli Hartmann. Application of the drs chip for fast waveform digitizing. *Nuclear Instruments and Methods in Physics Research Section A: Accelerators, Spectrometers, Detectors and Associated Equipment*, 623(1):486–488, 2010. 44, 52

[47] L Galli, U Hartmann, F Morsani, D Nicol, and S Ritt. A new generation of integrated trigger and read out system for the meg ii experiment. In *2014 IEEE Nuclear Science Symposium and Medical Imaging Conference (NSS/MIC)*, pages 1–3. IEEE, 2014. 45, 52, 73, 75, 100

[48] AM Baldini, E Baracchini, G Cavoto, M Cascella, F Cei, M Chiappini, G Chiarello, C Chiri, S Dussoni, L Galli, et al. Single-hit resolution measurement with meg ii drift chamber prototypes. *arXiv preprint arXiv:1605.07970*, 2016. 48, 57, 85

[49] M Venturini, A Baldini, E Baracchini, F Cei, S Dussoni, L Galli, M Grassi, D Nicolò, G Signorelli, et al. Meg ii drift chamber characterization with the silicon based cosmic ray tracker at infn pisa. *Nuclear Instruments and Methods in Physics Research Section A: Accelerators, Spectrometers, Detectors and Associated Equipment*, 2015. 48, 57, 85

[50] FCI. *Mini-SAS HD Next generation SAS storage interface.* 51, 75

[51] National Instruments. *www.ni.com/compactrio.* 53

[52] Dr. Mergenthaler GmbH & Co. KG. www.ma-info.de. 55

[53] Fabio Sauli. Principles of operation of multiwire proportional and drift chambers. Technical report, European Organization for Nuclear Research, 1977. 59, 60, 66

[54] William R Leo. Techniques for nuclear and particle physics experiments. *Dr155*, 1990. 59, 66

[55] Particle Data Group et al. *Particle physics booklet*. in the Americas, Australasia, or the Far East, write to: Particle Data Group, Lawrence Berkeley National Laboratory, 2004. 62, 101

[56] GD Alkhazov. Statistics of electron avalanches and ultimate resolution of proportional counters. *Nuclear Instruments and Methods*, 89:155–165, 1970. 64

[57] PSpiceSoftware. http://www.orcad.com/resources/orcad-downloads. 67, 74

[58] Analog Devices. Ada4927 datasheet ultralow distortion current feedback differential adc drive. 74

[59] Texas Instruments. Ths4509 datasheet wideband, low-noise, low-distortion, fully-differential amplifier. 75

[60] Eagle Software. http://www.cadsoftusa.com. 75

[61] www.spectra-strip.com. 75

[62] HA Bethe. Moliere's theory of multiple scattering. *Physical Review*, 89(6):1256, 1953. 84

[63] A. D'onofrio. Improving single hit reconstruction of the meg ii drift chamber by using the cluster timing information. *Master Degree Thesis*, 2015. 87, 90

[64] RCH Cheng and NAK Amin. Estimating parameters in continuous univariate distributions with a shifted origin. *Journal of the Royal Statistical Society. Series B (Methodological)*, pages 394–403, 1983. 90

[65] Bo Ranneby. The maximum spacing method. an estimation method related to the maximum likelihood method. *Scandinavian Journal of Statistics*, pages 93–112, 1984. 90